Modelling Hydrodynamic Interactions between Deformable Droplets

Rogério Manica

Submitted in total fulfilment of the requirements
of the degree of Doctor of Philosophy

June 2007

Department of Mathematics and Statistics
The University of Melbourne

Abstract

Understanding deformations during interaction of colloidal or nano droplets has important implications in a wide range of applications such as flotation collection and emulsion stability. The present work is important and necessary because current models are unable to properly describe recent experimental results obtained using the Atomic Force Microscope (AFM) and Surface Force Apparatus (SFA). We revisit and improve on theories involving interacting deformable droplets. A detailed theoretical model of the experiments, which accounts for surface forces, hydrodynamic interactions, droplet deformation and AFM cantilever deflection has been developed. The new feature of the model is the use of matched asymptotic expansions to derive a new boundary condition at constant volume to obtain results that are independent of the size of the computational domain.

The AFM experiments provide measurements of dynamical forces between two interacting droplets as well as between a drop and a colloidal particle of micrometre radii in solution when they are driven together and then are retracted from each other. The SFA experiments measure (time dependent) surface profiles of a millimetre size mercury drop interacting with a mica surface. Different configurations have been studied including mechanical and electrical perturbations to a thin film stabilized by double layer repulsion. Interesting experimental features were observed when approaching or retracting the mica from the mercury drop.

All these experiments are compared to our theoretical model and excellent agreement is observed using only measured parameters within an experimental error band. An important observation is the need of the no-slip hydrodynamic boundary condition on the liquid-liquid interfaces. The good

agreement together with fast solution of the numerical scheme allows us to run extensive sensitivity analysis to understand the separate contributions of hydrodynamic interaction, surface forces and drop deformation. It also gives confidence to use the model to predict situations that have not been reached experimentally and suggest interesting experiments to be performed using the available technology. Simple forms for small and large interaction forces have been derived and are useful in the range of experimental data available.

Declaration

This is to certify that:

(i) the thesis comprises only my original work towards the PhD except where indicated in the Preface,

(ii) due acknowledgement has been made in the text to all other material used,

(iii) the thesis is less than 100,000 words in length, exclusive of tables, and bibliographies.

Rogério Manica

Preface

The study of deformable interfaces and interactions with colloidal particles encompasses many diverse areas of science and consequently a number of different approaches are possible, ranging from engineering, chemistry, physics, and applied mathematics. This thesis is part of a wide project involving researchers from different departments in The University of Melbourne, University of South Australia, National University of Singapore and Institute of High Performing Computing in Singapore. In writing this thesis I have attempted to bridge these disciplines to show their complementary importance in understanding droplet interactions.

Even though I am one of the authors of a few articles involving experiments and theory, none of the experiments published or in this thesis were performed by me. My contribution to the project was in understanding and improving the theory for interacting droplets, writing numerical codes to solve the non-linear system of equations, comparing the theoretical results with the experiments provided by the collaborators, understanding theoretical and experimental results and providing new theoretical information that is not available from the experiments.

The assumptions of the derived model proved necessary to predict experimental results performed by collaborators using the AFM and the SFA. Each subproblem was organized in a different chapter, being all modelled by the same basic theory with appropriate modifications to take into account particular of each system. Separate literature reviews are for each experiment.

Acknowledgments

First and foremost I would like to thank my supervisors, Derek Chan and Steven Carnie. Their guidance and our discussions were essential to the development of this thesis.

I thank collaborators Raymond Dagastine and Grant Webber from the Department of Chemical and Biomolecular Engineering at The University of Melbourne for providing the AFM experimental data and collaborators Lucy Clasohm, Jason Connor, and Roger Horn from the Ian Wark Research Institute at University of South Australia for access to the SFA experimental data modelled in this thesis.

I also express my thanks to the staff of the Department of Mathematics and Statistics for their help and to my office mates, in particular Anna, Frederick, Jason, Jennifer, Kim, Amy and Ofer.

I gratefully acknowledge the financial support of the Melbourne International Research Scholarship and the Melbourne International Fee Remission Scholarship of the University of Melbourne. Particulate Fluids Processing Centre (PFPC), the Department of Mathematics and Statistics of the University of Melbourne and the Institute of Mathematical Sciences of the National University of Singapore (NUS) for conference support. My exchange program with NUS and the Institute of High Performance Computing was funded by a Postgraduate Overseas Research Experience Scholarship. The PFPC is an Australian Research Council Special Research Centre.

To my family and friends, in particular, the love and support of my parents, Eleodoro and Tereza Manica, and my siblings Denise, Vanderlei and Samuel for all the support during my education process. Last but not least I thank my fiancee Citra for all love and support during my PhD candidature.

Publications

R.R. Dagastine, R. Manica, S.L. Carnie, D.Y.C. Chan, G.W. Stevens, F. Grieser, 'Dynamic forces between two deformable oil droplets in water', *Science*, **113** (2006), 210–213.

R. Manica, J.N. Connor, S.L. Carnie, R.G. Horn, D.Y.C. Chan, 'Dynamics of interactions involving deformable drops: Hydrodynamic dimpling under attractive and repulsive electrical double layer interactions', *Langmuir*, **23** (2007), 626–637.

S.L. Carnie, D.Y.C. Chan and R. Manica, 'Modelling drop-drop interactions in an Atomic Force Microscope', *ANZIAM Journal*, **46(E)**, (2005), C805-C819.

S.L. Carnie, D.Y.C. Chan, C. Lewis, R. Manica and R.R. Dagastine, 'Measurement of dynamical forces between deformable drops using the Atomic Force Microscope I. Theory', *Langmuir*, **21**, (2005), 2912-2922.

R. Manica, J.N. Connor, L.Y. Clasohm, S.L. Carnie, R.G. Horn, D.Y.C. Chan, 'Transient responses of a wetting film to mechanical and electrical perturbations', *Langmuir*, Accepted (2007).

R. Manica, J.N. Connor, R.R. Dagastine, S.L. Carnie, R.G. Horn, D.Y.C. Chan 'Equilibrium and dynamic forces involving deformable interfaces at nanometer separations', *Physics of Fluids*, Submitted (2007).

G.B. Webber, R. Manica, S.A. Edwards, G.W. Stevens, S.L. Carnie, R.R. Dagastine, F. Grieser, D.Y.C. Chan, 'Hydrodynamic interactions between a silica particle and a deformable droplet: Effects of particle/droplet size ratio', *Journal of Physical Chemistry C*, Submitted (2007).

Contents

List of Tables

List of Figures

List of Symbols

Latin Symbols

b	Navier slip length
Bo	Bond number
Ca	Capillary number
Re	Reynolds number
f^*	Correction to Reynolds equation due to Navier slip
E	Interaction energy per unit area
F	Force
g	Gravity
G	Scaled force
h	Film thickness
h_0	Initial separation
h_c	Scale for thickness
h_s	Characteristic separation
H	Constant of integration in inner solution
K	Spring constant of cantilever
n	Electrolyte concentration

N	Size of the system of equations
p	Hydrodynamic pressure
p_c	Pressure scale
r	Radial coordinate
r_1, r_2	Radial extent of the drop
r_c	Radial scale
r_{max}	Scaled radial distance where boundary condition is applied
R	Radius related to Lagrange multiplier
R_0	Unperturbed radius of the drop or harmonic mean radius
R_1, R_2	Radius of drops in AFM experiment
s	Scaled radial coordinate
s_-, s_+	Constants
t	Time
T	Temperature
$\mathbf{u}$	Velocity vector
u_r	Radial or tangential velocity
u_z	Normal velocity
V	Approach velocity
V_d	Volume of the drop
X	Position
z	Axial coordinate
z_0	Initial height of the drop
z_1, z_2	Shape of the drops

Greek Symbols

δR	Perturbation to the radius
Δr	Grid spacing
ΔX	Displacement
ΔX_{max}	Maximum travel
Δs	Deflection of cantilever
$\Delta \rho$	Density difference between continuous and disperse phase
α	Constant associated with the new boundary condition
Γ	Integral of pressure
θ	Contact angle
θ_1, θ_2	Contact angles of the drops
θ_p	Constant contact angle
κ^{-1}	Debye length
μ	Viscosity
ν	Kinematic viscosity
λ	Capillary length
Λ	Lagrange multiplier
Π	Disjoining pressure
ρ	Density
σ	Interfacial tension
τ_d	Drop deformation time
χ	Scaled axial coordinate
ψ_0	Surface potential
ϕ	Azimuthal angle

Chapter 1

Introduction

In many multiphase processes ranging from ore flotation in the mineral industry to controlling emulsion stability in the manufacture of pharmaceutical and health care products, an important objective is to quantify and control the interaction involving deformable interfaces. Central to understanding the dynamics of interactions in soft matter, for example, suspensions of emulsion drops or cellular components of biological systems, is the interplay between colloidal forces such as van der Waals, electrical double-layer and steric forces, hydrodynamic interactions arising from relative motion within the suspension medium, surface tension forces, and internal Laplace pressure effects. These interactions give rise to surface deformations, which in turn determine the relative importance and contributions of various forces. Recent technological developments allowed precise measurements of the interaction between deformable interfaces. Devices used for this purpose include the Atomic Force Microscope (AFM) and the Surface Force Apparatus (SFA).

The AFM has been used successfully to measure both static forces involving deformable bubbles [34, 12, 61] and oil drops [55, 2, 56] in solution and the dynamic forces between a particle and a drop [3, 27] and between two oil drops (stabilized by surfactants) that have been driven together or pulled apart under well-controlled conditions [29, 28]. For drops of around 50 μm radius, the range of velocities studied in the latter experiments covers the range of thermal velocities for drops of this size. The strong dependence of the total interaction force on the relative velocity of approach and retract

demonstrated the importance of hydrodynamic effects. However, current experiments based on the AFM are as yet unable to provide direct information about the deformations of the interfaces during the course of interaction.

On the other hand, a complementary experimental technique based on using the SFA – originally developed to measure drainage of very thin films between solids [44, 40, 16, 43] – as an imaging device is well-suited to yield accurate details of the evolution of the surface profiles of drop deformation during interaction. Through analysis by video recording of fringes of equal chromatic order (FECO), Connor and Horn [25] were able to measure the space-time evolution of the deformations of a mercury/aqueous electrolyte interface due to hydrodynamic and electrical double-layer interactions with an approaching mica plate. The position of the deformable interface was determined with sub-nanometre precision for a mercury drop of radius $\sim$2 mm and mica velocity in the range 20–70 μm/s. As the surface potential of the mercury drop could be controlled independently, it was possible to study surface deformations under a range of repulsive and attractive interactions due to electrical double-layer forces between the mercury and the mica surface.

A characteristic of most experimental problems involving liquid-liquid, liquid-solid or solid-solid interactions in the colloidal range is the presence of a thin film that develops between the interacting surfaces. Starting with the work of Reynolds [62] more than 100 years ago, thin film theory has been developed and improved to take into account different problems that appeared over the years. Using the thin film assumptions, governing equations for the evolution of the film between drops have been derived [35, 37, 33] and treated numerically [36, 51, 50]. Surface forces have also been incorporated [18]. Two cases have been studied in detail: drops interacting under constant force [76, 77] and under constant velocity [1, 8, 47]. Unfortunately, these models were not appropriate to analyse the AFM and SFA experimental data available. For the drop sizes and velocities studied here, hydrodynamics, surface forces and deformation are all significant and must be included in the model.

In this thesis we derive evolution equations to model recent AFM and SFA experiments, in particular comparisons are performed for the experiments of

Dagastine et al. [29, 28], Connor and Horn [25] and Clasohm et al. [23]. The time evolution of the profiles uses the thin film assumptions with no-slip boundary condition for the liquid-liquid interface. Pressure is obtained through a normal stress balance and we apply the surface forces relevant to the particular experiment. The main theoretical contribution to the model is the use of asymptotic expansions to derive a new boundary condition at large separations that takes into account far field deformations at constant volume due to the interaction, effects of contact angle and cantilever deflection for the AFM case [13]. This general approach turns out to be necessary if one wishes to properly explain the experimental data available since the constant velocity model [47] gives results that depend on the size of the computational domain, being only useful in restricted situations.

Comparisons between the developed theory and experiments show an impressive agreement in most of the cases analysed using only experimental parameters within an error band of uncertainties of the experimental data. Such agreement suggests that the assumptions of the model are correct in representing the important physical characteristics of these systems in particular the controversial assumption of no-slip boundary condition in the liquid-liquid interfaces. This can be explained by the presence of surfactant in the system that immobilises the interface. Such boundary conditions are likely to be present in most real systems. Given the good agreement between our theory and experiments we are confident to use the model to explain all features of the experiment since just few characteristics are measured, for example interaction forces in the AFM and surface profiles in the SFA. We can also predict what would happen in situations where experiments are not yet available and suggest interesting experiments that can be performed using the available technology.

Most of the effort of this thesis was put on applications of the derived model to explain and understand hydrodynamic properties of deformable interfaces. After the derivation of equations in Chapter 2 each chapter consists on modelling a different experiment or set of experiments performed by collaborators. In the following we summarize each chapter to give an overview of the content of the thesis.

1. Chapter 2: We present the assumptions for modelling the AFM and SFA experiments, which lead to the thin film equations. Different features of the experiment are incorporated into the model through a new asymptotic boundary condition which derivation is shown in detail by matching inner and outer regions of the problem. Some features of the problem such as effect of gravity and Navier slip are also treated.

2. Chapter 3: We introduce the AFM experimental setup for two interacting drops under repulsive double layer forces. The experimental force-displacement data are then compared with the theoretical model for four different SDS concentrations and three different approach velocities. Given the good agreement we extract from the model features that cannot yet be measured experimentally, for example pressures, film thickness and velocity of the interface. An extensive parameter sensitivity analysis is also presented.

3. Chapter 4: We discuss a new experiment in which a solid sphere is interacted with an oil drop using the AFM. Good agreement for the interaction forces allows us to understand how the system behaves during approach and retract because the sphere is not deforming and we can recover the shape of the drop during interaction. This allows the observation of a wrapping regime which is smaller than originally thought and much of the response of the drop during interaction with the solid sphere is accommodated by far field deformation.

4. Chapter 5: We introduce the SFA experimental setup which is able to track deformations of the interface from a near-parabolic shape at large separations to the formation and development of the characteristic dimple when a mica plate is driven against a mercury/electrolyte interface. Impressive agreement is observed when comparing results for repulsive as well as attractive double layer. The model is further used to provide information that is not measured experimentally.

5. Chapter 6: We present three new experiments performed using the SFA and compare with our theory. The experiments consist of mechanical

and electrical perturbations of a stable film which is already close to a mica surface stabilised by double layer repulsion. Once again, the good agreement allows us to understand the modes of collapse of films when the repulsion is suddenly taken away.

6. Chapter 7: We discuss a theoretical work on interaction forces for both SFA and AFM cases. Comparisons between experiments, full numerical solution and simplified theories are presented and discussed in non-dimensional form. We also derive a nonlinear force-displacement formula showing that a drop cannot be treated as a Hookean spring.

7. Chapter 8: The thesis finishes with conclusions and ideas for future work.

Chapter 2

Governing Equations

2.1 Introduction

The theoretical contribution of this thesis is the development of a new boundary condition necessary for interacting droplets. The derivation of the model will be shown in detail for completeness using theoretical results of three previous papers: Chan et al. [15], Bardos [5] and Klaseboer et al. [47], resulting in the work of Carnie et al. [13]. Even though the derivation involves a different problem from the results of two of those papers in which a drop-solid sphere interaction was studied and takes into account different scales, parts of the derivation are simply reproduced from those works. The objective is to include every step of the derivation.

In earlier studies of the interaction of a small rigid colloid probe and a large decane drop [56], the interaction was observed to be independent of velocity within the range of the AFM. This allowed the result to be interpreted in terms of an equilibrium model. The force-stage position relationship $F(X)$ can be calculated from minimization of the total free energy of interaction, subject to a constant drop volume constraint [15]. The case where the three-phase contact line is kept fixed while the contact angle could vary was studied. Later, Bardos [5] generalized this theory considering also the case where three-phase contact line could slip while the contact angle remained fixed, and corrected some typographical mistakes in [15].

In the present case, in order to account for the relative speed of approach of the drops, the hydrodynamics of the thin liquid film must be incorporated into the model. The governing equations used here follow the work of Klaseboer et al. [47], but with improvements in the far field boundary conditions for pressure and thickness.

2.2 Film drainage

A considerable literature exists on modelling the drainage of a thin film between drops. In early works, the governing equations were derived using thin film assumptions [35, 37, 33]. Numerical treatment of the equations dates from the work of Hartland [36] and refined by Slattery [51], who described the drainage once a dimple had been formed. Surface forces were incorporated via a disjoining pressure in [18]. Two special cases have been studied in detail: drops interacting at constant force, appropriate for collisions driven by buoyancy forces [77] or at constant relative velocity in modelling inertial collisions [20, 1, 8]. The former case has been studied in great depth as a singular perturbation problem that requires matching across inner and outer regions [76]. This has been generalised to drops of different sizes [63] and to include the effect of attractive surface forces that cause drop coalescence [64].

The relative importance of hydrodynamics, surface forces and deformation depends on the drop size. The thin film equations have been tested experimentally on drops of millimetre size [46, 47] where dimpling of the thin film region typically occurs, with formation of a barrier ring that in turn restricts film drainage. In this regime, hydrodynamics is dominant, while repulsive surface forces determine the final film thickness at the barrier ring as well as the equilibrium film thickness.

For drops of micron size or smaller, surface tension is so strong, that is, the capillary number is so small that under typical conditions the drops remain spherical and deformation can be neglected. However, in the intermediate size range of 10–100 μm described here, hydrodynamics, surface forces and deformation are all significant and must be included in the model.

One important modelling step is to decide whether tangential stresses are

transmitted across the surfaces of the drops. If they are, which is generally the case for clean liquid-liquid interfaces, such surfaces are called *partially mobile*. The film velocity then has a slip velocity at the drop surface and the velocity field inside the drops must be accounted for in the governing equations. This model was carefully studied for non-deforming drops in [31] and with deformation in [1, 8, 76, 77]. In general, the film drainage then depends on the viscosity ratio of drop and film [8].

If the interface contains significant amounts of adsorbed surfactant, there is much evidence to suggest that the interface is *immobile* and no tangential stress is transmitted into the drop [47, 56]. This means that the film velocity at the drop surface is the same as that of the drop interface and a no-slip boundary condition applies. In this case, the thin film dynamics can be determined without the need to know the velocity inside the drops. Since the AFM experiment has adsorbed surfactant, we consider the drop surface to be immobile. Consequently a no-slip boundary condition is applied at the drop surfaces and there is no need to consider velocity fields inside the drops.

More recent work has focused on the inclusion of surfactant transport both from the bulk to the interface and within the interface due to Marangoni effects [10, 74, 75]. At surfactant concentrations at or above the critical micelle concentration, the liquid/liquid interfaces will be populated by a close-packed surfactant layer. In this situation we can ignore surfactant transport effects and we assume that the liquid/liquid interfacial tension remains constant and uniform during interaction.

2.3 The lubrication theory

For completeness and justification of using lubrication theory the next few pages summarize the theoretical background needed when modelling the experimental data we have available. To derive governing equations for interacting droplets, it is recommended taking into account the widely differing length scales that appear. This process leads to the thin film equations, which contains the essential physics of this problem. The starting point is the Navier-Stokes and continuity equations for a Newtonian incompressible

fluid, written as [7]

$$\frac{\partial(\rho\mathbf{u})}{\partial t} + \nabla\cdot(\rho\mathbf{uu}) = -\nabla p + \mu\triangle\mathbf{u} \tag{2.1}$$

$$\nabla\cdot\mathbf{u} = 0 \tag{2.2}$$

where ρ is the constant density, μ is the viscosity of the continuous phase which is assumed constant even at very small separations [43], p is the excess pressure in the film, and $\mathbf{u}$ is the velocity vector, being a function of time t and three spatial coordinates.

Cylindrical coordinates have been adopted because the drops are assumed spherical initially and the motion is along the symmetry axis. The components of the velocity vector $\mathbf{u}$ in this case are defined as: u_r, u_z and u_ϕ. The nature of the problem suggests axisymmetric flow. So, $u_\phi = 0$, where ϕ is the azimuthal angle and all partial derivatives with respect to ϕ are also zero. The Navier-Stokes (only r and z components left) and continuity equations become

$$\frac{\partial u_r}{\partial t} + u_r\frac{\partial u_r}{\partial r} + u_z\frac{\partial u_r}{\partial z} = -\frac{1}{\rho}\frac{\partial p}{\partial r} + \nu\left(\frac{1}{r}\frac{\partial}{\partial r}\left(r\frac{\partial u_r}{\partial r}\right) + \frac{\partial^2 u_r}{\partial z^2} - \frac{u_r}{r^2}\right) \tag{2.3}$$

$$\frac{\partial u_z}{\partial t} + u_r\frac{\partial u_z}{\partial r} + u_z\frac{\partial u_r}{\partial z} = -\frac{1}{\rho}\frac{\partial p}{\partial z} + \nu\left(\frac{1}{r}\frac{\partial}{\partial r}\left(r\frac{\partial u_z}{\partial r}\right) + \frac{\partial^2 u_z}{\partial z^2}\right) \tag{2.4}$$

$$\frac{1}{r}\frac{\partial(ru_r)}{\partial r} + \frac{\partial u_z}{\partial z} = 0 \tag{2.5}$$

For the problem of interacting drops, most terms in Eqs. (2.3-2.5) are much smaller compared to others and can be neglected. We adopt the scales suggested by Klaseboer et al. [47]

$$h_c = R_0 Ca^{1/2} \qquad p_c = \sigma/R_0 \qquad u_{rc} = V/Ca^{1/4}$$

$$r_c = R_0 Ca^{1/4} \qquad t_c = \mu Ca^{-1/2}/p_c \qquad u_{zc} = V$$

where R_0 is the undeformed radius of the drop. For the experiments studied here $r_c \gg h_c$. The large difference in length scales implies the weak variation of the film thickness with a typical radial scale and implies

$$\frac{\partial h}{\partial r} \ll 1 \tag{2.6}$$

which is needed in lubrication theory [62] and in the study of thin films generally [49]. The validity of this condition has been extensively discussed in the works of Chesters [1, 64, 8].

Inserting these scales into the cylindrical form of the Navier-Stokes equations and continuity equations yields the following non-dimensional form:

$$ReCa^{1/2}\left[\frac{\partial u_r}{\partial t}+u_r\frac{\partial u_r}{\partial r}+u_z\frac{\partial u_r}{\partial z}\right] = -\frac{\partial p}{\partial r}+\frac{\partial^2 u_r}{\partial z^2}+ Ca^{1/2}\left(\frac{1}{r}\frac{\partial}{\partial r}\left(r\frac{\partial u_r}{\partial r}\right)-\frac{u_r}{r^2}\right) \quad (2.7)$$

$$ReCa\left[\frac{\partial u_z}{\partial t}+u_r\frac{\partial u_z}{\partial r}+u_z\frac{\partial u_r}{\partial z}\right]=-\frac{1}{\rho}\frac{\partial p}{\partial z}+Ca\frac{1}{r}\frac{\partial}{\partial r}\left(r\frac{\partial u_z}{\partial r}\right)+Ca^{1/2}\frac{\partial^2 u_z}{\partial z^2} \quad (2.8)$$

$$\frac{1}{r}\frac{\partial(ru_r)}{\partial r}+\frac{\partial u_z}{\partial z}=0 \quad (2.9)$$

where $Re=\rho V h_s/\mu$ is the Reynolds number, with h_s some characteristic separation between the drops (around 50 to 100 nm in the experiments).

In all the experiments considered in this thesis, $Ca \ll 1$ and $Re \ll 1$ (Stokes flow), due to low velocities and small length scales. Typically, $Ca \sim 10^{-6}-10^{-8}$ for the AFM and SFA experiments and similar values for Re numbers. Retaining only leading order terms in the previous system provides the thin film equations which, when recast in dimensional variables, take the form:

$$\frac{\partial p}{\partial r} = \mu\frac{\partial^2 u_r}{\partial z^2} \quad (2.10)$$

$$\frac{\partial p}{\partial z} = 0 \quad (2.11)$$

$$\frac{\partial u_z}{\partial z} = -\frac{1}{r}\frac{\partial(ru_r)}{\partial r} \quad (2.12)$$

where the hydrodynamic problem was reduced to a radial pressure driven flow. Starting from this system we get an evolution equation for the film thickness $h(r,t)$ directly. We show this step for each experiment separately.

2.4 Equations for drop-wall interaction

We present first the derivation of the evolution equations for the drop-wall interaction because it is theoretically simpler when compared to the drop-drop interaction in AFM, since there is no deflection of the cantilever and there is a solid wall in which the no-slip boundary conditions can be applied and just one deformable interface. This derived equations have been used to model the experiments performed by Connor and Horn [25] and Clasohm et al. [23]. Figure 2.1 shows a schematic of the problem, V being the approach velocity, which can be a function of time. Here, X is the distance between the base of the drop (top of the syringe) and the wall (mica surface).

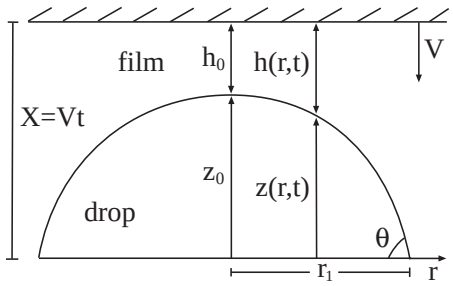

Figure 2.1: Schematic of a deformable drop interacting with a solid wall. X is the separation between the base and the wall, V is the approach velocity, h_0 is the initial separation, θ is the contact angle between the drop and the base, and r_1 is the length of the capillary tube, which is fixed.

We assume the simplest possible model in which the no-slip boundary condition applies at the solid/liquid interface (which is expected to hold at a solid interface) as well as at the liquid/liquid interface. In making this assumption, we are guided by the observation that experimental results for film drainage tend to be consistent with the no-slip boundary conditions rather than the full slip condition associated with the continuity of tangential stress across a liquid/liquid interface [47]. The application of the no-slip boundary condition at the liquid/liquid interface also means that one does not have to consider the possibility of flow in the interior of the drop. The assumption of a no-slip boundary condition at the liquid/liquid interface may afford simpli-

fication but can be contentious. Indeed there is a body of results, though not without controversy which suggests that the no-slip boundary may not apply at a solid boundary for film thickness in the nanometre range [57]. Nonetheless, we first examine a model with few parameters and consider the effects of a slip boundary condition later. Therefore, the tangential component of velocity at the drop/liquid interface must be zero.

$$u_r = 0 \quad \text{at} \quad z = h(r,t) \tag{2.13}$$

At the wall, the no-slip boundary condition implies

$$u_z = u_r = 0 \quad \text{at} \quad z = 0 \tag{2.14}$$

The drop is approaching the surface with velocity $V(t)$, where $V(t) = \partial h/\partial t$. Therefore,

$$u_z = V(t) = \frac{\partial h}{\partial t} \quad \text{at} \quad z = h(r,t) \tag{2.15}$$

As p does not depend on z according to Eq. (2.11), Eq. (2.10) can be integrated twice with respect to z, and applying boundary conditions for u_r gives

$$u_r = \frac{1}{2\mu}\frac{\partial p}{\partial r}(z^2 - hz) \tag{2.16}$$

Substituting u_r into the continuity equation (Eq. 2.12) and using Eq. (2.15) we obtain the Reynolds equation [62] for the evolution of the thickness of the thin film between a deformable drop and a rigid wall

$$\frac{\partial h}{\partial t} = \frac{1}{12\mu r}\frac{\partial}{\partial r}\left(rh^3\frac{\partial p}{\partial r}\right) \tag{2.17}$$

The characteristic drop deformation time of the drop/water interface in the SFA experiment is small compared to the typical experimental time. Therefore it is justified to assume that the deformation of the interface takes place under quasi-equilibrium conditions and can be assumed to be governed by the familiar Young-Laplace equation that relates the mean curvature of a fluid interface to the pressure difference across the interface. In addition to the Laplace pressure ($2\sigma/R_0$) between the two sides of the curved interface, there are two additional contributions to the pressure difference, namely, the

disjoining pressure Π on the interface due to colloidal forces of electrochemical origin between the mica and the mercury and the hydrodynamic pressure profile p, due to drainage of the aqueous film trapped between the mica plate and the deformable interface. Thus if the drop surface deformations are axially symmetric as observed experimentally and after using Eq. (2.6), the profile $z(r,t)$ of the drop obeys the Young-Laplace equation

$$p + \Pi = \frac{2\sigma}{R} + \frac{\sigma}{r}\frac{\partial}{\partial r}\left(r\frac{\partial z}{\partial r}\right) \tag{2.18}$$

where $(2\sigma/R)$ is the Lagrange multiplier that ensures the drop obeys the constant volume constraint. Now we use the geometrical relation

$$h(r,t) = X(t) - z(r,t) \tag{2.19}$$

to write Eq. (2.18) as

$$p + \Pi = \frac{2\sigma}{R} - \frac{\sigma}{r}\frac{\partial}{\partial r}\left(r\frac{\partial h}{\partial r}\right) \tag{2.20}$$

Eqs. (2.17) and (2.20) are to be solved numerically over the interval $0 \leq r \leq r_{max}$, subject to suitable initial conditions and boundary conditions where r_{max} is the largest radial distance at which we compute the profile numerically. The initial condition must be consistent with Eq. (2.20) in that it must produce a zero film pressure. This requirement is satisfied by a parabolic surface for the drop, which is also the local approximation to a sphere, as the initial condition

$$h(r,0) = h_0 + \frac{r^2}{2R_0} \tag{2.21}$$

where h_0 is the initial separation. To complete the system, four boundary conditions should be defined. Due to axial symmetry, we have

$$\frac{\partial h}{\partial r} = 0 \quad \text{at} \quad r = 0 \tag{2.22}$$

$$\frac{\partial p}{\partial r} = 0 \quad \text{at} \quad r = 0 \tag{2.23}$$

and at large radial distances the pressure decays as r^{-4} [76] and this condition is implemented as

$$r\frac{dp}{dr} + 4p = 0 \quad \text{at} \quad r = r_{max} \tag{2.24}$$

We need another boundary condition for $\frac{\partial h}{\partial t}$ at large separations. In previous works [22, 1, 47], the following constant velocity boundary condition was used

$$\frac{\partial h}{\partial t} = V \quad \text{at} \quad r = r_{max} \tag{2.25}$$

assuming no deformation outside the interaction region. To get agreement with experiments they needed r_{max} bigger than R_0 in some cases [48]. We show, with examples later in this chapter, that this boundary condition is unable to model the AFM and SFA experiments studied in this thesis. A new boundary condition will be derived to replace Eq. (2.25), taking into account the small deformations at constant volume, the effects of interfacial tension, the influence of the three-phase contact line and the cantilever deflection in the AFM case.

2.5 Equations for two interacting drops

The derivation of evolution equations for two interacting drops is performed next. A schematic of the situation is presented in Figure 2.2 in which the drops have different radii, R_1 and R_2, contact angles and contact lines. The derivation is similar to the drop/wall interaction and some details are omitted.

For the same reasons as in the previous case, we assume that the drop/liquid interface is immobile. Therefore, the tangential component of velocity at the interface must be zero.

$$u_r = 0 \quad \text{at} \quad z = z_1(r,t) \tag{2.26}$$

$$u_r = 0 \quad \text{at} \quad z = z_2(r,t) \tag{2.27}$$

where z_1 and z_2 represent the drop surfaces and $h = z_2 - z_1$ is the film thickness between the drops. As p does not depend on z according to Eq. (2.11), Eq. (2.10) can be integrated twice to give

$$u_r = \frac{1}{2\mu}\frac{\partial p}{\partial r}\left(z^2 - (z_1 + z_2)\, z + z_1 z_2\right) \tag{2.28}$$

where the no-slip boundary conditions Eqs. (2.26) and (2.27) were applied.

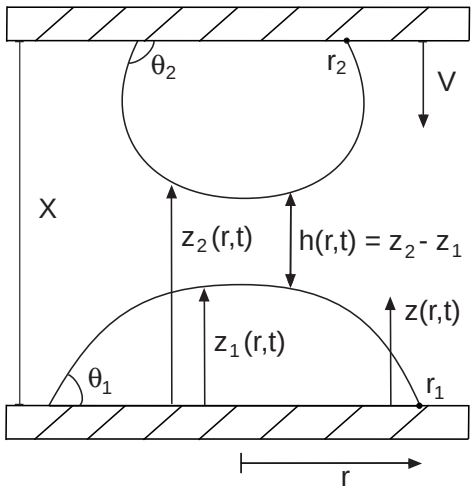

Figure 2.2: Schematic diagram of two interacting drops, which are sitting on two stages opposite to each other. The stages are placed at a distance X from each other and approach with velocity V. The film thickness is $h(r,t)$, the difference between the drop profiles $z_2(r,t)$ and $z_1(r,t)$. The drops have different radii R_1 and R_2 with contact angles θ_1 and θ_2 and contact lines r_1 and r_2 respectively. Radial coordinate r as well as $z(r,t)$ are also indicated.

The drops are approaching with velocity V, where $V = \partial h/\partial t$ and therefore

$$u_z = V = \frac{\partial h}{\partial t} \quad \text{at} \quad z = h(r,t) \tag{2.29}$$

The continuity equation (2.12) is integrated with respect to z to give

$$u_z = \frac{1}{4\mu r}\frac{\partial}{\partial r}\left[r\frac{\partial p}{\partial r}\left(\frac{z_2^3}{3} - z_1 z_2^2 + z_1^2 z_2 - \frac{z_1^3}{3}\right)\right] \tag{2.30}$$

resulting in since $h = z_2 - z_1$

$$\frac{\partial h}{\partial t} = \frac{1}{12\mu r}\frac{\partial}{\partial r}\left(rh^3\frac{\partial p}{\partial r}\right) \tag{2.31}$$

which is the same equation as for drop-wall interaction (Eq. (2.17)).

The Young-Laplace equations for each drop are written as

$$p + \Pi = \frac{2\sigma}{\hat{R}_1} + \frac{\sigma}{r}\frac{\partial}{\partial r}\left(r\frac{\partial z_1}{\partial r}\right) \tag{2.32a}$$

$$p + \Pi = \frac{2\sigma}{\hat{R}_2} - \frac{\sigma}{r}\frac{\partial}{\partial r}\left(r\frac{\partial z_2}{\partial r}\right) \tag{2.32b}$$

where $2\sigma/\hat{R}_1$ and $2\sigma/\hat{R}_2$ are the Lagrange multipliers associated with the constant drop volume constraint with $\hat{R}_1 \approx R_1$ and $\hat{R}_2 \approx R_2$. Eqs. (2.32a) and (2.32) can be added to give since $h = z_2 - z_1$

$$p + \Pi = \frac{2\sigma}{\hat{R}_0} - \frac{\sigma}{2r}\frac{\partial}{\partial r}\left(r\frac{\partial h}{\partial r}\right) \tag{2.33}$$

where

$$\frac{1}{\hat{R}_0} = \frac{1}{2}\left(\frac{1}{\hat{R}_1} + \frac{1}{\hat{R}_2}\right) \tag{2.34}$$

The initial condition for the two different drops is written as

$$h(0,r) = h_0 + \frac{r^2}{2R_1} + \frac{r^2}{2R_2} = h_0 + \frac{1}{2}\left(\frac{1}{R_1} + \frac{1}{R_2}\right)r^2 = h_0 + \frac{r^2}{R_0} \tag{2.35}$$

where h_0 is the initial separation between the drops and R_0 is the harmonic mean radius of the two drops defined as

$$\frac{1}{R_0} = \frac{1}{2}\left(\frac{1}{R_1} + \frac{1}{R_2}\right) \tag{2.36}$$

The boundary conditions are defined as:

$$\frac{\partial h}{\partial r} = 0 \quad \text{at} \quad r = 0 \tag{2.37}$$

$$\frac{\partial p}{\partial r} = 0 \quad \text{at} \quad r = 0 \tag{2.38}$$

$$r\frac{dp}{dr} + 4p = 0 \quad \text{at} \quad r = r_{max} \tag{2.39}$$

A suitable boundary condition for $\dfrac{\partial h}{\partial t}$ at large radial distances will be derived in Section 2.7.

2.6 Equations for drop-sphere interaction

We derive equations for the interaction of a sessile drop of radius R_d interacting with a solid sphere of radius R_s. Once again we assume the no-slip

hydrodynamic boundary condition at the liquid-liquid as well as at the solid-liquid interface resulting in the thin film equation

$$\frac{\partial h}{\partial t} = \frac{1}{12\mu r}\frac{\partial}{\partial r}\left(rh^3\frac{\partial p}{\partial r}\right) \tag{2.40}$$

as shown before. The Young-Laplace equation is written as

$$p + \Pi = \frac{2\sigma}{\hat{R}_d} + \frac{2\sigma}{R_s} - \frac{\sigma}{r}\frac{\partial}{\partial r}\left(r\frac{\partial h}{\partial r}\right) \tag{2.41}$$

where $2\sigma/\hat{R}_d$ is Lagrange multipliers associated with the constant drop volume constraint.

The initial condition for a drop and a sphere is written as

$$h(0,r) = h_0 + \frac{r^2}{2R_d} + \frac{r^2}{2R_s} = h_0 + \frac{1}{2}\left(\frac{1}{R_d} + \frac{1}{R_s}\right)r^2 = h_0 + \frac{r^2}{R_0} \tag{2.42}$$

where h_0 is the initial separation and R_0 is the harmonic mean radius between the drop and the sphere.

Three of the boundary conditions are the same as for drop-drop interaction and a suitable boundary condition for $\frac{\partial h}{\partial t}$ at large radial distances will be derived in the next section.

2.7 Derivation of new asymptotic boundary condition

The derivation of the new boundary condition necessary to model the experiments studied in this thesis follows previous works performed by Chan et al. [15] and Bardos et al. [5] and was published in Carnie et al. [13]. In the former cases, the analytical stationary solution of a small spherical solid particle moved against an oil drop in AFM was obtained. The same ideas of those works are used in this section, but making the necessary adjustments to solve the static drop-wall interaction. Generalization for two different drops and drop-sphere cases and the introduction of cantilever deflection for the AFM will be performed later. One main difference is the definition of new scales

appropriate to this case, since in the former the small particle introduced a scale that had to be taken into account.

Gravity has a negligible effect in the experiments studied in this thesis and will be neglected. Later in this chapter we discuss its effects. The free energy $\mathcal{F}$ without gravity can be written as

$$\mathcal{F} = 2\pi \int_0^{r_1} r[\sigma(1 + z'^2)^{1/2} + E(h(r, z))]\ dr \tag{2.43}$$

where E is the interaction energy per unit area between the drop and the plate and r_1 is position of the three-phase contact line.

The drop volume is

$$V_d = 2\pi \int_0^{r_1} rz\ dr \tag{2.44}$$

The drop shape is determined by minimising the free energy, while constraining the drop volume to remain constant. Introducing the Lagrange multiplier

$$\Lambda = \frac{2\sigma}{R} \tag{2.45}$$

and minimising $\mathcal{F}(z) - \Lambda V_d(z)$, we obtain the augmented Young-Laplace equation

$$\sigma \frac{d}{dr}\left[\frac{z'r}{(1 + z'^2)^{1/2}}\right] - r\Pi(h(r)) = -\Lambda r \tag{2.46}$$

with the boundary condition

$$z'(0) = 0 \tag{2.47}$$

and the definition of disjoining pressure

$$\frac{\partial E}{\partial z} \approx \frac{\partial E}{\partial h} = -\Pi(h(r)) \tag{2.48}$$

using the Derjaguin approximation [32] for the interaction energy. The film is so weakly varying in the radial scale that we can use the disjoining pressure at the local separation $h(r)$ with negligible error.

A first integral of (2.46) is, using (2.47)

$$\frac{z'r}{(1 + z'^2)^{1/2}} = -\frac{r^2}{R} + \Gamma(r) \tag{2.49}$$

where

$$\Gamma(r) = \frac{1}{\sigma}\int_0^r r\Pi(h(r))\ dr \tag{2.50}$$

Rearranging Eq. (2.49) gives

$$z' = \frac{-r^2/R + \Gamma(r)}{[r^2 - (-r^2/R + \Gamma(r))^2]^{1/2}} \tag{2.51}$$

Equation (2.51) is the start of the process of generating inner and outer solutions for matching purposes.

2.7.1 Inner region

For the inner region, we introduce the following scales

$$r = \sqrt{R_0 h_s}s \tag{2.52}$$

$$z - z_0 = h_s\chi(s) \tag{2.53}$$

where R_0 is the unperturbed radius of the drop, h_s a characteristic separation and z_0 the unperturbed apex height. Substituting these scales in Eq. (2.51) yields

$$\chi' = -s + \frac{\Gamma(s)}{h_s s} + O(h_s/R) \tag{2.54}$$

Integrating with respect to s gives

$$\begin{aligned}\chi &= -\frac{s^2}{2} + \frac{1}{h_s}\int_0^s \frac{\Gamma(s')}{s'}\ ds' \\ &= -\frac{s^2}{2} + \frac{1}{h_s\sigma}\int_0^s \frac{ds'}{s'}\int_0^{s'} s''\Pi(h(s''))\ ds'' \\ &= -\frac{s^2}{2} + \frac{R_0}{\sigma}\int_0^s s'\Pi(h(s'))(\ln s - \ln s')\ ds'\end{aligned} \tag{2.55}$$

with a change of order of integration. For large s, $\Pi(h(s))$ restricts the integration range by vanishing. Thus

$$\chi(s) \sim -\frac{s^2}{2} + \frac{1}{h_s}[G\ln s - H] \tag{2.56}$$

where

$$G = \frac{h_s R_0}{\sigma}\int_0^\infty s\Pi(h(s))\ ds \tag{2.57}$$

$$H = \frac{h_s R_0}{\sigma} \int_0^\infty s \ln s \; \Pi(h(s)) \; ds \tag{2.58}$$

In unscaled variables the outer behaviour of the inner solution is

$$z(r) = z_0 - \frac{r^2}{2R} - H + G \ln \left(\frac{r}{\sqrt{h_s R_0}} \right) \tag{2.59}$$

We note that the total force is (in the Derjaguin approximation)

$$F = 2\pi \int_0^\infty r \Pi(h(r)) \; dr = 2\pi\sigma G \tag{2.60}$$

2.7.2 Outer Region

For the outer solution, the following scales are adopted

$$r = (GR)^{1/2} s \tag{2.61}$$

$$z(r) = (GR)^{1/2} \chi(s) \tag{2.62}$$

and recognize that $\Gamma(r)$, in this distance regime, can be replaced by $\Gamma(\infty)$, which is simply G. The profile equation (2.51) for the outer region becomes

$$\chi' = \frac{\pm(1 - s^2)}{(s_+^2 - s^2)^{1/2}(s^2 - s_-^2)^{1/2}} \tag{2.63}$$

where we define s_+ and s_- so that

$$s_+^2 s_-^2 = 1 \tag{2.64}$$

$$s_+^2 + s_-^2 = \frac{R}{G} + 2 \tag{2.65}$$

with solution

$$\chi = \int_s^{s_+} \frac{ds(s^2 - 1)}{(s_+^2 - s^2)^{1/2}(s^2 - s_-^2)^{1/2}} \mp \int_{s_1}^{s_+} \frac{ds(s^2 - 1)}{(s_+^2 - s^2)^{1/2}(s^2 - s_-^2)^{1/2}} \tag{2.66}$$

being

$$s_1 = r_1/(GR)^{1/2} \tag{2.67}$$

In Eq. (2.66) the upper sign refers to acute drop profiles and the lower sign refers to obtuse drop profiles. The integral can be evaluated exactly in terms of incomplete elliptic integrals E and F to give

$$\chi(s) = s_+ E(K(s), q) - \frac{1}{s_+} F(K(s), q) \mp \left(s_+ E(K(s_1), q) - \frac{1}{s_+} F(K(s_1), q) \right) \tag{2.68}$$

where

$$K(s) = \arcsin\left(\frac{s_+^2 - s^2}{s_+^2 - s_-^2}\right)^{1/2} \tag{2.69}$$

$$q^2 = 1 - \left(\frac{s_-}{s_+}\right)^2 \tag{2.70}$$

$$F(K,q) = s_+ \int_s^{s_+} \frac{ds}{(s_+^2 - s^2)^{1/2}(s^2 - s_-^2)^{1/2}} \tag{2.71}$$

$$E(K,q) = \frac{1}{s_+} \int_s^{s_+} \frac{s^2 ds}{(s_+^2 - s^2)^{1/2}(s^2 - s_-^2)^{1/2}} \tag{2.72}$$

to match this solution to the inner solution, s is considered to be in the range $s_- \ll s \ll s_+$ (ie., $G \ll r \ll R$). It follows that

$$s_+ = (R/G)^{1/2}(1 + G/R + \cdots) \tag{2.73}$$

$$s_- = (G/R)^{1/2}(1 - G/R + \cdots) \tag{2.74}$$

Hence

$$q^2 = 1 - O((G/R)^2) \tag{2.75}$$

$$\sin K(s) = 1 - \frac{G}{2R}s^2(1 + O(G/R)) \tag{2.76}$$

$$\sin K(s_1) = (1 - (r_1/R_+)^2)^{1/2}(1 + O(G/R)^2) \tag{2.77}$$

where

$$R_+ = (RG)^{1/2}s_+ = R + G + \cdots \tag{2.78}$$

Note that for $q^2 \approx 1$,

$$E(K,q) = \sin K + \cdots \tag{2.79}$$

$$F(K,q) = \frac{1}{2}\ln\left(\frac{1 + \sin K}{1 - \sin K}\right) + \cdots \tag{2.80}$$

Substitution of these limiting forms into the exact equation (2.68) yields

$$\chi(s) = \left(\frac{R}{G}\right)^{1/2}\left(1 + \frac{G}{R}\right)\left[1 - \frac{Gs^2}{2R} \mp \left(1 - \left(\frac{r_1}{R_+}\right)^2\right)^{1/2}\right] - \left(\frac{G}{R}\right)^{1/2}\left[-\frac{1}{2}\ln\left(\frac{Gs^2}{4R}\right) \mp \frac{1}{2}\ln\left(\frac{1 + (1 - (r_1/R_+)^2)^{1/2}}{1 - (1 - (r_1/R_+)^2)^{1/2}}\right)\right] + \cdots \tag{2.81}$$

which in unscaled variables can be written as

$$z(r) = R\left[1 \mp \left(1 - \left(\frac{r_1}{R_+}\right)^2\right)^{1/2} - \frac{r^2}{2R^2}\right] + G\left[1 \mp \left(1 - \left(\frac{r_1}{R_+}\right)^2\right)^{1/2} + \frac{1}{2}\ln\left(\frac{r^2}{4R^2}\right) \pm \frac{1}{2}\ln\left(\frac{1 + (1 - (r_1/R_+)^2)^{1/2}}{1 - (1 - (r_1/R_+)^2)^{1/2}}\right)\right] + \cdots \quad (2.82)$$

where r_1 is the radial extent of the drop where it touches the solid base, R_+ is the maximum radial width of the drop and the upper(lower) sign refers to drops with an acute(obtuse) contact angle at the base.

2.7.3 Matching the inner and the outer regions

We have the following geometric relation between the drop profile $z(r,t)$, the film thickness $h(r,t)$ and displacement $X(t) = Vt$

$$h(r,t) = X(t) - z(r,t) \quad (2.83)$$

In the numerical solution of the thin film equations, an asymptotic condition for the time derivative $\dot{h}(r,t)$ for $r \gg r_c$ is required. This can be obtained by differentiating Eq. (2.83) to give

$$\dot{h}(r,t) = V - \dot{z}(r,t) \quad (2.84)$$

We apply Eq. (2.84) at the outer part of the inner region at some large distance r_{max} on the inner scale, where we can use Eq. (2.59):

$$\dot{h}_{rmax} = V - \dot{z}_{rmax} = V - \left[\dot{z}_0 - \dot{H} + \dot{G}\frac{1}{2}\ln\left(\frac{r_{max}^2}{r_c^2}\right)\right] \quad (2.85)$$

after discarding terms that are negligible. To find $\dot{z}_0 - \dot{H}$, we have to match with the solution Eq. (2.82) from the outer region.

Now we take a G/R_0 expansion, using the following definition

$$R_+ \equiv R_0 + \delta R + G \quad (2.86)$$

to get

$$R = R_0 + \delta R \quad (2.87)$$

Using the geometrical relation

$$\sqrt{1-\frac{r_1^2}{R_0^2}} = \pm\cos\theta \tag{2.88}$$

leads to

$$\begin{aligned} z(r) &= -\frac{r^2}{2R} + R_0[1-\cos\theta] + \delta R\left[1-\frac{1}{\cos\theta}\right] \\ &\quad + G\left[1-\frac{1}{\cos\theta}+\frac{1}{2}\ln\left(\frac{r^2}{4R_0^2}\right)+\frac{1}{2}\ln\left(\frac{1+\cos\theta}{1-\cos\theta}\right)\right] \end{aligned} \tag{2.89}$$

By comparing Eq. (2.89) with (2.59), we see that the terms in r^2 and $\ln r$ match, while equating the constants give:

$$\begin{aligned} z_0 - H &= R_0[1-\cos\theta] + \delta R\left[1-\frac{1}{\cos\theta}\right] \\ &\quad + G\frac{1}{2}\ln\left(\frac{r_c^2}{4R_0^2}\right) + G\left[1-\frac{1}{\cos\theta}+\frac{1}{2}\ln\left(\frac{1+\cos\theta}{1-\cos\theta}\right)\right] \end{aligned} \tag{2.90}$$

At this stage, we must specify the behaviour of the three-phase contact line at the base of each drop. In [15], the contact line was considered pinned at some fixed radial position r_1 during interaction. In [5], the contact line was also allowed to slip while keeping a constant contact angle θ_p.

Considering the pinned case (constant r_1) first, we differentiate Eq. (2.89) with respect to time to get:

$$\dot{z}_{rmax} = \dot{\delta R}\left[1-\frac{1}{\cos\theta}\right] + \dot{G}\frac{1}{2}\ln\left(\frac{r_{max}^2}{4R_0^2}\right) + \dot{G}\left[1-\frac{1}{\cos\theta}+\frac{1}{2}\ln\left(\frac{1+\cos\theta}{1-\cos\theta}\right)\right] \tag{2.91}$$

where we have evaluated the result at some suitably large value of $r = r_c = r_{max}$. Now we need an expression to the change in mean curvature δR as a function of the force G. By constraining the volume we get [5]

$$\delta R = -G\frac{1}{1-\cos\theta} \tag{2.92}$$

Using this result we can then simplify Eq. (2.91) to give

$$\dot{z}_{rmax} = \dot{G}\left[1+\frac{1}{2}\ln\left(\frac{r_{max}^2}{4R_0^2}\right)+\frac{1}{2}\ln\left(\frac{1+\cos\theta}{1-\cos\theta}\right)\right] \tag{2.93}$$

which from Eq. (2.84) provides the required boundary condition for $\dot{h}$ for the pinned contact line case:

$$\dot{h}_{rmax} + \frac{\dot{G}}{2}\left[2 + \ln\left(\frac{r_{max}^2}{4R_0^2}\right) + \ln\left(\frac{1+\cos\theta}{1-\cos\theta}\right)\right] = V \tag{2.94}$$

A constant contact angle $\theta = \theta_p$ is equivalent to constant profile derivative at the contact line, this means [5],

$$\delta R = -G\frac{1}{(2+\cos\theta_p)(1-\cos\theta_p)} \tag{2.95}$$

The boundary condition for the constant contact angle case is then

$$\dot{h}_{rmax} + \frac{\dot{G}}{2}\left[2 + \ln\left(\frac{r_{max}^2}{4R_0^2}\right) + \ln\left(\frac{1+\cos\theta_p}{1-\cos\theta_p}\right) - \frac{2}{2+\cos\theta_p}\right] = V \tag{2.96}$$

Eqs. (2.94) or (2.96) are the requisite large r boundary conditions for the numerical solution of the inner film drainage equation.

2.8 The AFM experiment

In the AFM experiment the two drops are different and the cantilever deflects. It is necessary to develop a more general boundary condition accounting for these differences. This situation is presented in Figure 2.3. The drops have radii R_1 and R_2 and the respective contact angles are θ_1 and θ_2 and contact lines are at r_1 and r_2. Both drops are assumed to be of the same material and therefore have the same interfacial tension σ.

2.8.1 Boundary condition for two different drops

Starting from the quasi static shapes of two deformable drops z_1 and z_2, that are related to the velocity of approach and separation by the geometric relation

$$h(r,t) = X(t) - (z_2 - z_1) = \mp Vt - (z_2 - z_1) \tag{2.97}$$

The static shapes z_1 and z_2 of two deformable drops are governed by the Young-Laplace equation written as

$$\sigma\frac{d}{dr}\left[\frac{z_i' r}{(1+z_i'^2)^{1/2}}\right] - r\Pi(h(r)) = -\Lambda_i r \quad \text{for} \quad i = 1,2 \tag{2.98}$$

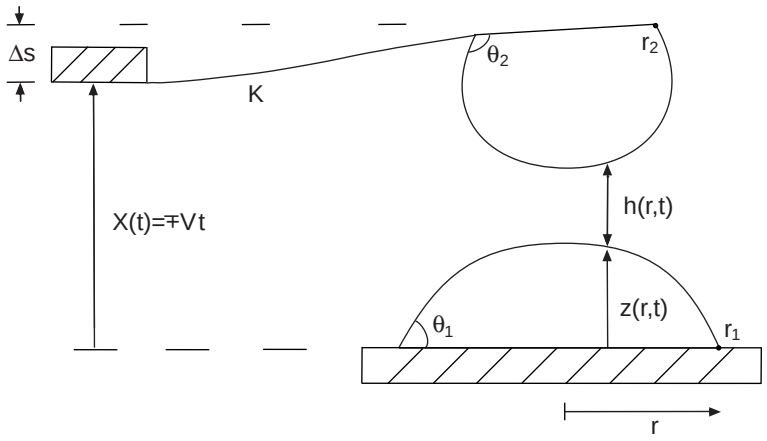

Figure 2.3: Schematic diagram of the AFM geometry of two interacting drops. X measures the distance between the piezo stage and some fixed platform, Δs is the cantilever deflection, $z(r,t)$ is the drop height and $h(r,t)$ is the film thickness.

where $\Lambda_1 = 2\sigma/\hat{R}_1$ and $\Lambda_2 = 2\sigma/\hat{R}_2$. These equations can be solved separately going through the process shown previously. The outer form of z_1 and z_2 for the inner region for each case is

$$z_i(r,t) = z_{0i}(t) - \frac{r^2}{2R_i} - H + G\ln(r/r_c) \quad \text{for} \quad i = 1,2 \tag{2.99}$$

where $r_c = \sqrt{h_s R_0}$ is the radial scale. Taking the derivative yields

$$\dot{h} = \mp V - (\dot{z}_2 - \dot{z}_1) \tag{2.100}$$

By substituting gives

$$\dot{h}_{rmax} = \mp V - \left[\dot{z}_0 - 2\dot{H} + \dot{G}\ln\left(\frac{r_{max}^2}{r_c^2}\right)\right] \tag{2.101}$$

To find $\dot{z}_0 - 2\dot{H}$, we have to match the outer region, whose solutions are given by

$$\begin{aligned} z_i(r) &= R_i\left[1 - \frac{r^2}{2R_i^2} \mp \sqrt{1 - \frac{r_i^2}{R_{+i}^2}}\right] \\ &\quad + G\left[1 \mp \sqrt{1 - \frac{r_i^2}{R_{+i}^2}} + \frac{1}{2}\ln(\frac{r^2}{4R_i^2}) \pm \frac{1}{2}\ln\left(\frac{1 + \sqrt{1 - \frac{r_i^2}{R_{+i}^2}}}{1 - \sqrt{1 - \frac{r_i^2}{R_{+i}^2}}}\right)\right] \end{aligned}$$

for i = 1, 2. Taking small deformation expansion and going through the process shown before results

$$\dot{z}_{irmax} = \dot{G}\left[1 + \frac{1}{2}\ln\left(\frac{r_{max}^2}{4R_i^2}\right) + \frac{1}{2}\ln\left(\frac{1+\cos\theta_i}{1-\cos\theta_i}\right)\right] \tag{2.102}$$

and the boundary condition for two different drops writes

$$\dot{h} + (\alpha_1 + \alpha_2)\dot{G} = \mp V \quad \text{at} \quad r = r_{max} \tag{2.103}$$

where, for the stick contact line case

$$\alpha_i = 1 + \ln\left(\frac{r_{max}}{2R_i}\right) + \frac{1}{2}\ln\left(\frac{1+\cos\theta_i}{1-\cos\theta_i}\right) \quad i = 1, 2. \tag{2.104}$$

and for the slip contact line case

$$\alpha_i = 1 + \ln\left(\frac{r_{max}}{2R_i}\right) + \frac{1}{2}\ln\left(\frac{1+\cos\theta_i}{1-\cos\theta_i}\right) - \frac{1}{2+\cos\theta_i} \tag{2.105}$$

2.8.2 Boundary condition for a drop and a sphere

For the interaction between a sessile drop of radius R_d and contact angle θ and a sphere of radius R_s, the asymptotic boundary condition for dh/dt at large r takes the form, for the stick contact line case

$$\dot{h}_{rmax} + \dot{G}\left[1 + \frac{1}{2}\ln\left(\frac{r_{max}^2}{4R_d^2}\right) + \frac{1}{2}\ln\left(\frac{1+\cos\theta}{1-\cos\theta}\right)\right] = \mp V \tag{2.106}$$

taking into account contributions from one deformable drop. Note that the radius of the drop appears in the equation, but not the radius of the sphere, and as a consequence a system with a big drop and small particle is different compared to that of a big particle and a small drop with same radius values. If we take the limit of the radius of the sphere to infinity we recover the drop-wall system and therefore the drop wall problem is just a particular case of the drop-sphere one.

2.8.3 Incorporating the cantilever deflection

The results in the preceding section have been derived on the assumption that the cantilever does not deflect. In fact as the bottom drop approaches

the top drop, all interactions will cause the cantilever to deflect which in turn increases the separation between the drops. This coupled motion of the cantilever and the drops must be incorporated into the formulation.

We model the cantilever as a plane attached to a fixed platform by a spring of stiffness K. Then Eq. (2.84) will be replaced by

$$h(r,t) = X - 2z(r,t) + \Delta s \tag{2.107}$$

where Δs is the *deflection* of the cantilever. Assuming a linear spring with spring constant K, Δs is related to the force F by

$$\Delta s = F/K = 2\pi\sigma G/K \tag{2.108}$$

where we use the convention that a positive force produces a positive (upwards) deflection of the spring. Differentiating Eq. (2.107) we have

$$\dot{h}(r,t) = \mp V - 2\dot{z}(r,t) + 2\pi\sigma\dot{G}/K \tag{2.109}$$

which shows that the motion of the cantilever can be included through an extra term in the asymptotic boundary conditions, which in final form is

$$\dot{h}_{rmax} + \dot{G}\left[\alpha_1 + \alpha_2 - \frac{2\pi\sigma}{K}\right] = \mp V \tag{2.110}$$

For the case of a drop interacting with a solid sphere in AFM, the boundary condition becomes

$$\dot{h}_{rmax} + \dot{G}\left[1 + \frac{1}{2}\ln\left(\frac{r_{max}^2}{4R_d^2}\right) + \frac{1}{2}\ln\left(\frac{1+\cos\theta}{1-\cos\theta}\right) - \frac{2\pi\sigma}{K}\right] = \mp V \tag{2.111}$$

We observe that the contribution due to deflections of the cantilever is always negative. This is because cantilever deflection will allow the top drop to back away as the bottom drop approaches and to follow the bottom drop as the latter withdraws. These boundary conditions are needed to completely determine the numerical solution of the thin film drainage equations.

2.9 Disjoining pressure

The disjoining pressure used is based on the DLVO theory [69, 41]. To model the SFA experiment performed by Connor and Horn [25], a numerical solution of the Poisson-Boltzmann equation was used to account for the different

surface potential giving disjoining pressures ranging from repulsive to attractive. The Poisson-Boltzmann equation can be written as [54]

$$\frac{d^2y(\xi)}{d\xi^2} = \sinh y(\xi) \tag{2.112}$$

where $y = e\nu\psi/k_BT$ is the potential scaled by the thermal potential, with k_B being the Boltzmann constant, T the absolute temperature, and e is the protonic charge. The coordinate x normal to the surface is related to the scaled variable $\xi = \kappa x$ being $\kappa = \sqrt{2ne^2/\epsilon kT}$ is the usual Debye-Hückel parameter that depends on salt concentration n. This equation is solved numerically using the algorithm proposed by [17] in which for a given pressure we get the distance.

2.10 Scaling and numerical solution

Before solving numerically, we first scale the equations using the scales suggested by Klaseboer et al. [47]. The time scale set by the approach velocity $t_c = h_c/V$, the Laplace pressure sets the pressure scale, the radial scale is set by the region of significant deformation $r_c^2 = R_0h_c$ and h_c is chosen to nondimensionalize the equations. Different scales are typically used for approach at constant force [77, 64]. With this choice, the various physical quantities are:

$$\begin{aligned} h_c &= R_0Ca^{1/2} \\ r_c &= R_0Ca^{1/4} \\ p_c &= \sigma/R_0 \\ t_c &= \mu Ca^{-1/2}/p_c \end{aligned}$$

where $Ca = \mu V/\sigma$ is the capillary number – the ratio of viscous forces to surface tension forces. Taking as an example the two equal drops in AFM

case, the non-dimensional form of the Eqs. (2.31), (2.33) and (2.60) becomes:

$$\frac{\partial h}{\partial t} = \frac{1}{12r}\frac{\partial}{\partial r}(rh^3\frac{\partial p}{\partial r}) \tag{2.113}$$

$$p + \Pi = 2 - \frac{1}{2r}\frac{\partial}{\partial r}(r\frac{\partial h}{\partial r}) \tag{2.114}$$

$$G = \int_0^\infty r[p(r,t) + \Pi]dr \tag{2.115}$$

In calculating G numerically, we divide the range of integration into two parts:

$$G = \int_0^{r_{max}} r[p + \Pi]\ dr + \int_{r_{max}}^\infty rp\ dr \tag{2.116}$$

where the first integral is evaluated from the numerical solution and the second integral, in which the disjoining pressure Π is negligibly small, can be evaluated analytically from the asymptotic r^{-4} form of the pressure.

Initial and boundary conditions become

$$h(r,0) = h_0 + r^2 \tag{2.117}$$

$$\frac{\partial h}{\partial r} = 0 \text{ at } r = 0 \tag{2.118}$$

$$\frac{\partial p}{\partial r} = 0 \text{ at } r = 0 \tag{2.119}$$

$$r\frac{dp}{dr} + 4p = 0 \text{ at } r = r_{max} \tag{2.120}$$

$$\frac{\partial h}{\partial t} + \alpha\frac{dG}{dt} = \mp 1 \text{ at } r = r_{max} \tag{2.121}$$

where

$$\alpha = \left[2 + \ln\left(\frac{r_{max}^2 Ca^{1/2}}{4}\right) + \ln\left(\frac{1+\cos\theta}{1-\cos\theta}\right) - \frac{2\pi\sigma}{K}\right] \tag{2.122}$$

in the case in which the three-phase contact line of the drop is fixed at $r = r_1$. For the constant contact angle boundary condition $\theta = \theta_p$ (fixed)

$$\alpha = \left[2 + \ln\left(\frac{r_{max}^2 Ca^{1/2}}{4}\right) + \ln\left(\frac{1+\cos\theta_p}{1-\cos\theta_p}\right) - \frac{2\pi\sigma}{K} - \frac{2}{2+\cos\theta_p}\right] \tag{2.123}$$

A detailed numerical study of two large drops (radius ∼1500 μm) has been carried out by Klaseboer et al. [47]. They considered film drainage and

dimple formation at a film thickness of order of 1 μm, where surface forces can be omitted. For the range of drop sizes considered in the present work (radius 40 μm), the drainage films have a thickness at which surface forces cannot be neglected.

Our new boundary condition Eq. (2.121), involving the derivative of a functional of the dependent variable h, changes the mathematical nature of the problem – we no longer have a simple boundary condition. However, on discretization in r as in the Method of Lines, we get a system of equations with a more standard form.

We use central differencing in r in Eq. (2.113) and (2.114) to obtain a system of differential equations for $h_j(t) \equiv h(j\Delta r, t), j = 0 \cdots N$ where $N = r_{max}/\Delta r$. We use a uniform grid in $r = [0, r_{max}]$ with $\Delta r = 0.05$ and $r_{max} = 10$ producing a system of 200 equations. The boundary conditions at $r = 0$ are used to produce the equation for $\dot{h}_0$ and Eq. (2.121) provides the equation for $\dot{h}_N$. This requires G as an extra variable to solve for. The functional G is obtained by evaluating the following integral using Simpson's rule

$$G = \int_0^{r_{max}} r[p(r,t) + \Pi]\, dr$$

which relates G to all the other variables h_j as an algebraic constraint.

In summary, the final system of equations has the form

$$\begin{pmatrix} 1 & 0 & \cdots & 0 & 0 \\ 0 & 1 & 0 & \cdots & 0 \\ & & \vdots & & \\ 0 & 0 & \cdots & 1 & \mathcal{F} \\ 0 & 0 & \cdots & 0 & 0 \end{pmatrix} \begin{pmatrix} \dot{h}_0 \\ \dot{h}_1 \\ \vdots \\ \dot{h}_N \\ \dot{G} \end{pmatrix} = \begin{pmatrix} f_0 \\ f_1 \\ \vdots \\ \mp 1 \\ G - \sum_j w_j g(h_j) \end{pmatrix} \tag{2.124}$$

where $\mathcal{F}$ is the coefficient of $\dot{G}$ in Eq. (2.121) and f_j represent the discretized contributions of the thinning equation and normal stress balance.

This system has a singular mass matrix and is a differential-algebraic equation (DAE) of index 1. It can be solved by standard software, in our case Matlab's `ode15s`.

Previous work [47] used the boundary condition for the thinning rate

$$\frac{\partial h}{\partial t} = \mp 1 \quad \text{at} \quad r_{max} \tag{2.125}$$

which neglects the deformation of the whole drop by the force G. In their work, they compared the film profile $h(r,t)$, especially the central film thickness $h(0,t)$ with experiments. We shall see that the central film thickness is not sensitive to the thinning rate boundary condition, which explains why their results appeared reasonably independent of the choice of r_{max}. The force however is sensitive to the position r_{max} where we apply the boundary condition.

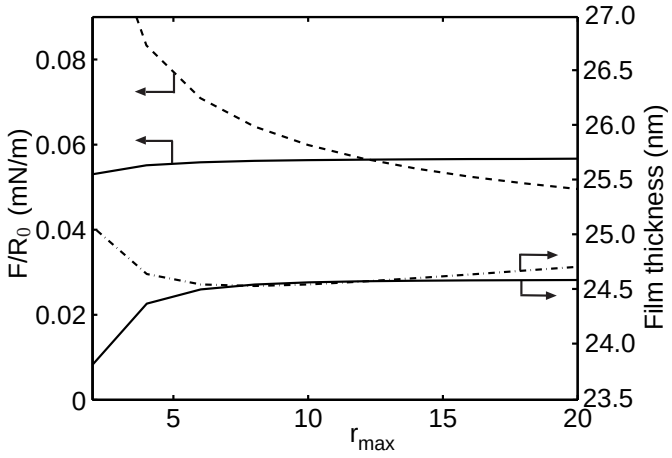

Figure 2.4: The scaled force F/R_0 ($R_0 = 41$ μm) and central film thickness at the end of 1 μm approach of two drops initially 0.7 μm apart, as a function of r_{max}, the size of the computational domain. The broken curves correspond to results using the simple boundary condition Eq. (2.125) and the solid curves are results obtained with the new boundary condition Eq. (2.121).

To see why the new boundary condition is necessary in our calculations, consider the central film thickness $h(0,t)$ and force F calculated for different choices of r_{max}. To have confidence in the numerical results, the results need to be independent of r_{max} once it is large enough to be outside the interaction zone. In Fig. 2.4, we show results for the central film thickness for a range of r_{max} values. The other parameters are: the initial central film thickness

(surface separation) is 0.7 μm, the piezo is driven in 1 μm at a velocity $V =$ 13.2 μm/s, the undeformed contact angle $\theta = \pi/3$ and the cantilever stiffness is $K = 28$ mN/m. Also shown are results using the simple boundary condition Eq. (2.125). For the film thickness, the choice of boundary condition is not crucial, although the new boundary condition does give results noticeably less dependent on r_{max}. By contrast, a similar plot for the force divided by R_0, shows that no sensible choice of r_{max} can be made using Eq. (2.125) but that the results are stable for $r_{max} \geq 6$ with our new boundary condition.

Numerical results should be independent of grid size. Different values of Δr were tested and compared in Figure 2.5. As can be seen, using $\Delta r = 0.5$ does not give a reasonable solution while for $\Delta r = 0.01$, 0.05 and 0.1, almost the same result is obtained. The value chosen and used in the comparisons is $\Delta r = 0.05$, because it is small enough to give accurate solutions and not time consuming.

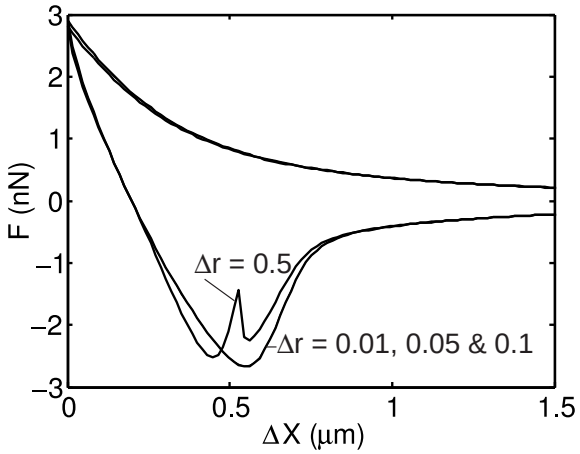

Figure 2.5: Force F as a function of displacement ΔX for grid sizes $\Delta r = 0.01$, 0.05, 0.1 and 0.5 for a typical AFM run as in Figure 2.4 using $r_{max} = 10$.

2.11 Introducing Navier slip

In all comparisons performed in this thesis, the no-slip boundary condition at the liquid/liquid as well as solid/liquid interfaces proved to be adequate.

A recent review by Neto et al. [57] referred to hundreds of papers on the topic covering from the first efforts in trying to describe what happens in the solid/liquid interface up to sophisticated experiments performed nowadays. It turns out that if slip is present it becomes important only for scales smaller than 100 nm, which is the case in the present study.

An important characteristic in determining boundary slip behaviour is roughness since most real systems are rough. Its presence in the surface was found to both increase the degree of slip at the surface [11] or alternatively reduce the degree of slip [60, 80]. Some questions arise about the definition of roughness and how to deal with it. Rough surfaces were obtained via different ways in the experiments. In some cases, by treating the surface; in others, by attaching a layer of polymers see, for example [79]. Another issue in rough surfaces is where to define the location of the solid-fluid interface where a particular boundary condition should be applied: at the peak or at the valleys or in the middle? Most experimental results were obtained by measuring interaction forces using the AFM or SFA and comparing with the classical Reynolds theory.

The interpretation of the experimental results were characterized in terms of a 'slip length' b, defined as the distance inside the wall where the velocity of the fluid would be zero. This means that the flow has a finite velocity at the wall. Figure 2.6 presents an schematic of the slip length assuming Stokes flow.

The slip velocity u_s on the wall is assumed to be proportional to the shear stress (Navier slip) at the surface

$$u_s = b\frac{\partial u_r}{\partial z} \tag{2.126}$$

In this case, $b = 0$ corresponds to the conventional no-slip boundary condition and $b = \infty$ corresponds to fully mobile interface, which is a conventional condition for a liquid/gas interface.

The no-slip boundary condition combined with the Navier-Stokes equations gives the following expression for the interaction between a solid sphere of radius R approaching a flat surface with velocity V, known as the Reynolds

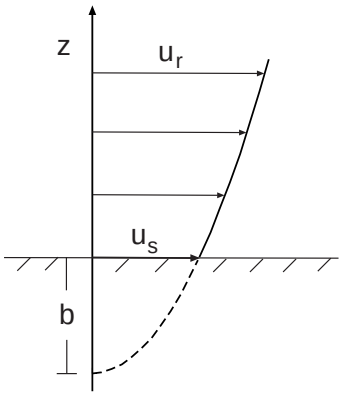

Figure 2.6: Schematic of the slip length b for a viscous flow near a solid surface. u_s represents the velocity of the fluid at the interface and u_r the velocity of the flow.

equation

$$F_H = f^* \frac{6\pi\mu R^2 V}{h} = f^* \frac{6\pi\mu R^2}{h} \frac{dh}{dt} \tag{2.127}$$

where f^* was introduced as the dimensionless number that quantifies the deviation from the classical prediction. If $f^* = 1$ we have the classical no-slip boundary condition. Vinogradova [70] derived the following expression for f^* for a given slip length b

$$f^* = \frac{h}{3b}\left[\left(1 + \frac{h}{6b}\right)\ln\left(1 + \frac{6b}{h}\right) - 1\right] \tag{2.128}$$

Many experimental works use this expression to estimate their slip length. Unfortunately there is no agreement between experiments with the slip length b ranging from few nanometres to few micrometres. Slip length was also found to depend on shear rates and viscosity [26].

Spikes and Granick [66] proposed a new model to account for slip. Instead of using the Navier boundary condition, they assume there exists a critical shear stress, below which the interface behaves as no-slip and above which Navier slip applies. They obtained good agreement with some experiments, but this model introduces another fitting parameter that has to be obtained in comparing theory and experiments.

Joseph and Tabeling [45] used particle image velocimetry to measure the flow profile inside a glass channel about 12 μm high. They obtained a parabolic profile and extrapolated the parabola into the wall to get the slip length. After analyzing the data, they concluded slip length up to 50 $\pm$ 100 nm. The data has lots of scatter and the slip length obtained is of the same order of the uncertainty of the position of the wall (about 30 nm).

We present evolution equations considering Navier slip in either or both interfaces following the work of Vinogradova and Feuillebois [71]. Once again the starting point are continuity equation (2.12) and thin film equations (2.10) and (2.11). This time it is assumed that one interface has slip length b_h and the other has slip length b_0. Therefore, the following boundary conditions are defined

$$u_r = b_0 \frac{\partial u_r}{\partial z}, \quad u_z = 0; \quad \text{at} \quad z = 0 \tag{2.129}$$

$$u_r = -b_h \frac{\partial u_r}{\partial z}, \quad u_z = \frac{\partial h}{\partial t}; \quad \text{at} \quad z = h \tag{2.130}$$

Using Eq. (2.11), we can integrate Eq. (2.10) twice with respect to z to get

$$u_r = \frac{1}{\mu}\frac{\partial p}{\partial r}\left(\frac{z^2}{2} + Az + B\right) \tag{2.131}$$

Now we apply the boundary condition for u_r and take into account that

$$\frac{\partial u_r}{\partial z} = \frac{1}{\mu}\frac{\partial p}{\partial r}(h + A) \quad \text{at} \quad z = h \tag{2.132}$$

and

$$\frac{\partial u_r}{\partial z} = \frac{1}{\mu}\frac{\partial p}{\partial r}A \quad \text{at} \quad z = 0 \tag{2.133}$$

to get

$$u_r = \frac{1}{2\mu}\frac{\partial p}{\partial r}\left(z^2 + \bar{A}z + b_0\bar{A}\right) \tag{2.134}$$

where

$$\bar{A} = -\frac{h(h + 2b_h)}{h + b_h + b_0} \tag{2.135}$$

Using the continuity (Eq. (2.12)) and applying the boundary conditions for u_z gives

$$\frac{\partial h}{\partial t} = \frac{1}{12\mu r}\frac{\partial}{\partial r}\left(r\frac{\partial p}{\partial r}\left[h^3 + 3\frac{(b_h + b_0)h^3 + 4b_0 b_h h^2}{h + b_h + b_0}\right]\right) \tag{2.136}$$

Note that when $b_h = b_0 = 0$ we recover the classical no-slip result Eq. (2.31). This equation is only used in few plots to indicate the effects of slip.

2.12 The effect of gravity

In this section we quantify the effect of gravity for the experiments we are analysing. For the AFM case the drops are small and gravity can be safely neglected due to small Bond numbers. On the other hand, for the SFA experiments the drops are larger and a discussion about the effect of gravity becomes necessary. The mercury drop protrudes from a capillary of radius r_1. At equilibrium, the shape of the drop is governed by the Young-Laplace equation

$$\sigma \frac{d}{dr}\left[\frac{rz'}{(1+z'^2)^{1/2}}\right] - r\Pi(h(r,z)) - r\Delta\rho g z = -\Lambda r \tag{2.137}$$

where Λ is the Lagrange multiplier associated with enforcing the constant volume constraint and $\Delta\rho$ is the density difference between the drop and the bathing medium.

By introducing the dimensionless variables s, χ

$$r = r_1 s; \qquad z = r_1 \chi \tag{2.138}$$

Eq. (2.137) (in the absence of disjoining pressure Π) can be written as

$$\frac{d}{ds}\left[\frac{s\chi'}{(1+\chi'^2)^{1/2}}\right] - \left(\frac{r_1}{\lambda}\right)^2 s\chi = -\frac{\Lambda r_1}{\sigma} s \tag{2.139}$$

This shows that the effect of gravity is measured by the dimensionless Bond number $Bo = (r_1/\lambda)^2$ where the capillary length λ is given by

$$\lambda = \left(\frac{\sigma}{\Delta\rho g}\right)^{\frac{1}{2}} \tag{2.140}$$

The Bond number in the present mercury experiment ($Bo \sim 0.6$) is larger than that encountered in the oil drop experiments [13] both because the drops are larger and mercury is much denser than water so the effect of gravity on the static drop shape is not small.

However, if we consider the change in the static profile of the drop under the imposition of a force F at the apex we can associate with the force a length scale $G = F/(2\pi\sigma)$ and the radial scale of deformations is given by $r_c = \sqrt{r_1 G}$ (see e.g. [15, 5]). The Bond number at the scale of r_c instead of r_1 is $(r_c/\lambda)^2 \sim 0.01 \ll 1$ which shows that gravity can be neglected in computing the profile for $r < r_c$. Since Eq. (2.20) is only used in this inner region, the appropriate value of R is the radius of curvature at the apex which has been measured experimentally when the mica surface is far from the mercury/electrolyte interface.

Our attempt to modify the derivation in [13] to include gravity proved intractable, so we argue that for the purpose of providing a matching outer boundary condition for the inner solution we can replace the mercury drop in gravity by an 'equivalent' gravity-free (spherical) drop. Now the solution of the Young-Laplace equation for a drop in the presence of gravity with an apex radius of curvature $R = 1.9$ mm and a capillary radius $r_1 = 1.5$ mm produces a nonspherical drop with volume 3.2 mm^3 and a contact angle $\theta = 59.6^\circ$ at the capillary edge $r = r_1$. So if we wish to treat the drop as a gravity-free spherical drop with radius R being the actual radius of curvature at the apex of the drop, then the two plausible options are either to use a spherical drop with the same capillary radius r_1 of 1.5 mm but a smaller volume or one with the same volume as the actual drop but with a larger capillary radius. The first choice gives a drop of volume 2.8 mm^3 and a contact angle $\theta = 52.1^\circ$ at $r = r_1$ and this is the value we will use throughout. The second choice requires a capillary radius r_1 of 1.54 mm and a contact angle $\theta = 54.2^\circ$ at the capillary. It turns out that none of the results we present below are sensitive to such small differences in the values of θ [14]. In Figure 2.7 we compare the drop shapes with and without gravity.

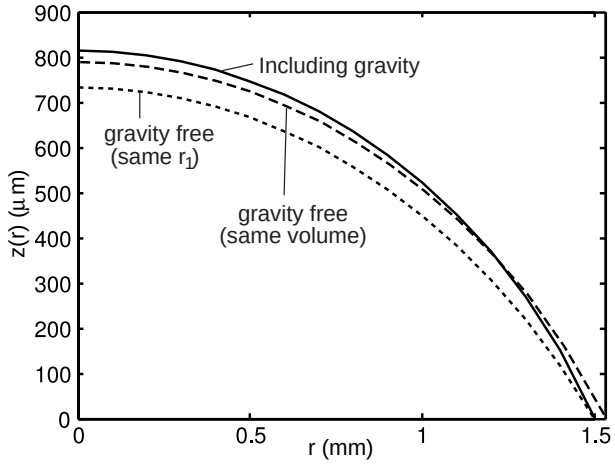

Figure 2.7: Comparison of solutions of the Young-Laplace equation (2.137) for the shape of the drop including gravity and two gravity free cases: one with the same volume and the other with the same contact line r_1.

Chapter 3

The AFM experiment

3.1 Introduction

The Atomic Force Microscope (AFM) has long been used to make direct measurements of the forces acting between rigid particles of colloidal dimensions. Attention has since turned to the interaction between deformable surfaces, such as the interaction between rigid probe particles and oil drops [55, 65, 15, 30] or between a particle and a bubble [34]. The hydrodynamic interaction of a rigid colloid probe with a solid surface [26, 11] and with a liquid drop [3] has also been studied using the AFM.

The first direct AFM measurements of the force between two approaching droplets of decane ($\sim$40 μm radius) in an aqueous solution of sodium dodecyl sulphate (SDS) was performed by Dagastine et al. [29]. The observed forces are velocity dependent at relative velocities comparable to that due to thermal motion of such droplets in suspension. Recently, Dagastine et al. [28] performed force measurements over a wide range of SDS concentrations (0.1 to 10 mM) and approach velocities (2 to 28 μm/s) and compared the experimental results with the theory developed by Carnie et al. [13].

In this experimental setup, one drop is attached to the AFM cantilever with known spring constant K. The other drop is attached to a piezoelectric stage that is moved according to a programmed velocity schedule. For example, the stage is moved towards the cantilever with constant velocity V

over a displacement X_{max} and is then reversed over the same distance. That is, the piezo displacement follows a triangular sweep.

During the programmed velocity schedule, the deflection of the spring is recorded and converted to a force F using the spring constant of the cantilever. Therefore, the experimental data consist of pairs of values (X_i, F_i), the piezoelectric stage position and the corresponding force. Note that the separation between the piezoelectric stage and the cantilever, much less the minimum separation between the drops, is unknown, even initially. Hence there is the need to relate experimental data to a force-separation law.

A characteristic feature seen in the measured forces between deformable drops [29, 28] is the dependence on the approach velocity V, which is also observed in similar experiments between a solid colloid probe and a liquid drop [3]. At low velocities, the force law is reversible, being the same on approach and retract, with an approximately constant compliance region that has a slope much less than that for rigid-rigid surface contact. At higher velocities that are comparable to velocities due to thermal motion of drops in a suspension, the force curves show hysteresis. Attractive forces of significant magnitude are observed when the drops are at the retract phase of the programmed velocity schedule.

This chapter is divided as follows. Firstly, we introduce the parameters of the experiment performed by Dagastine followed by a comparison between experiments and the theory developed in this work together with an experimental error analysis. The chapter follows with a parameter sensitivity study and lastly some predictions of the model, in which we extract information not provided by the experiment.

3.2 Parameters of the experiment

The experimental setup presents physical, geometrical and chemical parameters, which are all considered in the model. Measured values, experimental error as well as theoretical values used for comparisons are reported in tables.

The surface tension is known to decrease as sodium dodecyl sulfate (SDS) concentration is added to the system [56]. Table 3.1 presents SDS concen-

tration and corresponding surface tensions for the case of decane droplets in water [56] for the four cases modelled. Once the SDS concentration reaches the critical micelle concentration (cmc), which is around 8 mM in this case, the surface tension remains constant even with the introduction of more SDS. The experimental error is about ±1 mN/m in the interfacial tension measurements.

Electrolyte concentration, n (mM SDS)	0.1	1	3	10
Drop surface tension, σ (mN/m)	39	26.5	17.5	8.6

Table 3.1: Variation of the surface tension due to SDS concentration [56] with added salt of 1 mM $NaNO_3$.

The remaining experimental parameters are summarized in Table 3.2 together with possible experimental error. Their variations due to the addition of SDS were found to be small and are within experimental error.

Type	Physical parameter	Value
Surface force	Drop surface potential, ψ_0	-100 ± 10 mV
	Electrolyte concentration	1 mM $NaNO_3$
Fluid	Viscosity (water), μ	0.89 mPa s
	Drop radius cantilever, R_c	43 ±2 μm
	Drop radius piezo, R_p	90 ± 2 μm
	Drop contact angle p, θ_1	50° ± 5°
	Drop contact angle c, θ_2	90° – 180°
AFM	Cantilever spring constant, K	0.12 ±0.01 N/m
	Maximum piezo travel, ΔX_{max}	2.0 μm
	Piezo drive velocity, V	2 – 28 μm/s
	Initial separation, h_0	unknown

Table 3.2: Experimental parameters of the drop-drop interaction in an AFM.

In the theory we use values within experimental error to obtain the best fit between theory and experiment. Table 3.3 indicates the values used in the

theory for the 0.1, 1, 3 and 10 mM SDS cases. When a set of parameters was found, those were maintained fixed for all velocities at that concentration. The initial separation h_0 is unknown, but was not changed for more than 30 nm through all velocities. All comparisons presented in this chapter use values displayed in this table.

Physical parameter	0.1 mM	1 mM	3 mM	10 mM
Surface potential, ψ_0 (mV)	-100	-100	-100	-100
Surface tension, σ (mN/m)	39	27.5	16.5	11
Radius - cantilever, R_c (μm)	41	41	41	41
Radius - piezo, R_p (μm)	90	90	90	90
Contact angle p, θ_1	50	50	50	50
Contact angle c, θ_2	100	100	110	100
Spring constant, K (N/m)	0.13	0.13	0.13	0.13

Table 3.3: Theoretical parameters of the drop-drop interaction in an AFM.

Each run is expected to have a different initial separation h_0. It is shown in Figure 3.4 that the results are strongly sensitive to h_0, therefore h_0 can be extracted accurately using the model. In Table 3.4, we present all initial separations used in the compared results for 3 different velocities and 4 different SDS concentrations. Note that for a given concentration, all h_0 are close to each other.

V / Conc.	0.1 mM SDS	1 mM SDS	3 mM SDS	10 mM SDS
2 μm/s	1.86 μm	1.92 μm	1.75 μm	1.80 μm
9.3 μm/s	1.86 μm	1.92 μm	1.76 μm	1.80 μm
28 μm/s	1.89 μm	1.94 μm	1.77 μm	1.80 μm

Table 3.4: Theoretical initial separations, h_0, for different velocities and concentrations

3.3 Results: theory and experiments

The derived model can well represent AFM interactions between deformable droplets. The comparisons between the model and the experiments show excellent agreement in all tested cases. Experiments consist of a series of runs over a range of SDS concentrations (0.1 to 10 mM) and approach velocities (2 to 28 μm/s). Eqs. (2.113) and (2.114) are solved numerically subjected to the boundary conditions (Eq. (2.121)) and assuming that the three-phase contact line does not move (Eq. (2.122)). The disjoining pressure is calculated using the nonlinear Poisson-Boltzmann equation (Eq. (2.112)).

Figure 3.1 shows force displacement comparisons between experiments and theory for 3 mM SDS concentration and velocities 2, 9.3 and 28 μm/s, as indicated in the figure. The other parameters used are presented in Table 3.3 and the initial separations h_0 in Table 3.4.

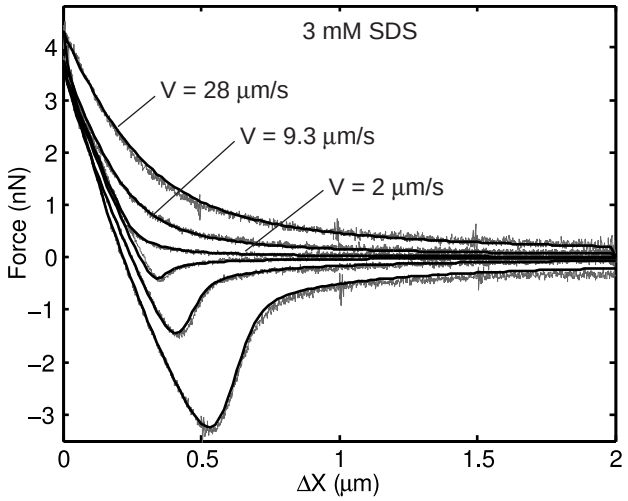

Figure 3.1: Theoretical and experimental forces for 3 mM SDS concentration and velocities $V = 2$, 9.3 and 28 μm/s. For the experimental parameters see Tables 3.3 and 3.4.

While the agreement is notable a discussion of the impact of the experimental error on the comparison with the theory is necessary. The independently measured parameters have an experimental uncertainty, but the

largest source of error on these force data is the experimental error in the calibration of the cantilever spring constant with an accuracy of ten percent [42]. The theory is sensitive to statistically significant errors in each of the above parameters, but a comparison of the impact of all these errors on the theoretical calculations offers a more practical comparison to the experimental data. The gray regions in Figure 3.2 are bounded by the maximum and minimum experimental uncertainties for all these parameters for a velocity of 28 μm/s.

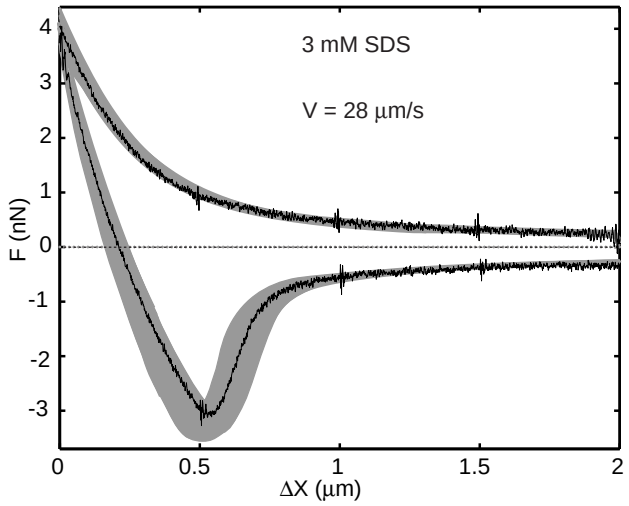

Figure 3.2: Parameters sensitivity band and experimental data for V = 28 μm/s and 3 mM SDS concentration.

Comparisons for the remaining cases are presented in Figure 3.3. The agreement is impressive for all cases using mostly experimental measured values. As can be seen, the experimental force curve falls well inside the band representing all possible theoretical solutions within experimental error. The only exception is the case of 10 mM concentration, where the best fit is achieved by putting all uncertainties to one side of the error band. This case is above the CMC for SDS, approximately 8.0 mM, and the presence of micelles has been accounted for in the solution ionic strength, but not any possible additional effect on the disjoining pressure.

The agreement between the experimental data and the quantitative model identifies a number of significant points related to describing the dynamics in

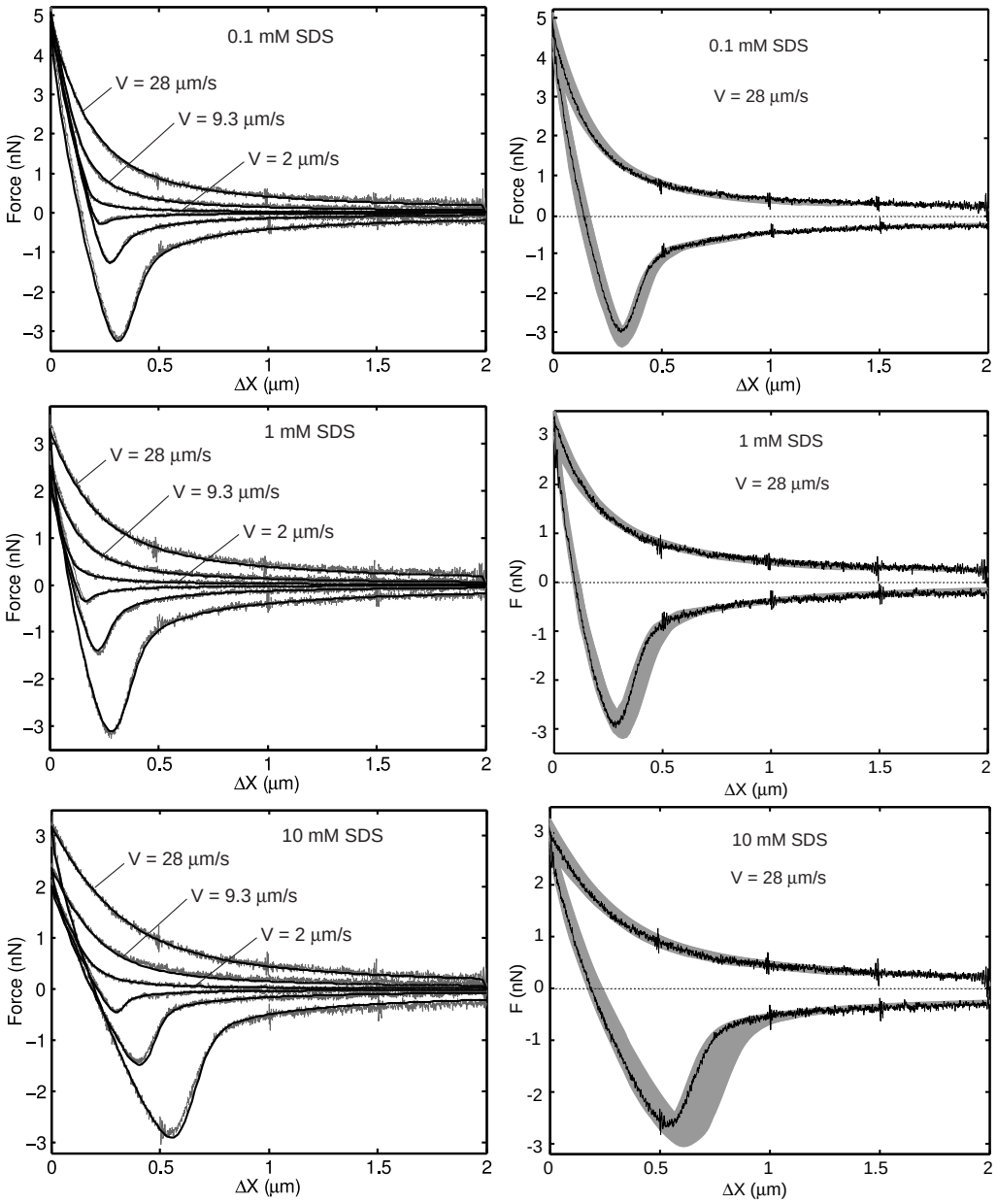

Figure 3.3: Comparison between theory and experiments for V = 2, 9.3 and 28 μm/s and 0.1, 1.0 and 10 mM SDS concentrations. For the experimental parameters see Table 3.3.

liquid-liquid systems. Equilibrium forces, hydrodynamic drainage effects and interfacial deformation all have a significant impact on the dynamic droplet interactions in a size range that was previously experimentally inaccessible. The traditional description of drainage as a two stage process with decoupled physics does not apply to droplets of this size and the concepts developed have the potential to be carried over to larger scale models used to predict emulsion stability and design of processes reliant on drop coalescence.

3.4 Parameter sensitivity

The sensitivity of each parameter alone is compared using a typical case from the experiments. The choice of velocity ($V = 28$ μm/s) was mainly for visual purposes, since most changes happen at higher velocities and it is easy to visualise. Similar behaviours are observed for all the velocities studied as well as concentrations. The following physical and AFM parameters are used in all runs of this section: $\Delta X = 2$ μm, $h_0 = 1.95$ μm, $\sigma = 26.5$ mN/m, $\theta_1 = 50°$, $\theta_2 = 100°$, $R_p = 90$ μm, $R_c = 41$ μm, $K = 0.13$ N/m, ψ_0 = -100 mV, and 1 mM concentration of SDS and 1 mM of sodium nitrate giving a Debye length of $\kappa^{-1} = 6.8$ nm. These set of parameters are analyzed one at a time.

The sensitivity analysis turns important for the initial separation, h_0, because it is the only unknown of the experiment. Results presented in Figure 3.4a show that a small change in h_0 provides a considerable change in the maximum force at the end of the push, which is used to obtain the initial separation value. Such sensitivity provides an accuracy within 1% of the actual experimental value in extracting it from the model. Clearly, if h_0 is shorter the magnitude of the interaction force will be bigger both repulsive and attractive for the same amount of push. Important to observe that when $h_0 = 2.05$ μm, the total push is shorter than the initial separation, being the force given solely by hydrodynamic interaction.

Related to the initial separation is the piezo displacement ΔX_{max}. In practice, for the range studied increasing initial separation and keeping total push fixed is equivalent to decrease total push by the same amount and keeping the initial separation fixed. Figure 3.4b compares the force curves

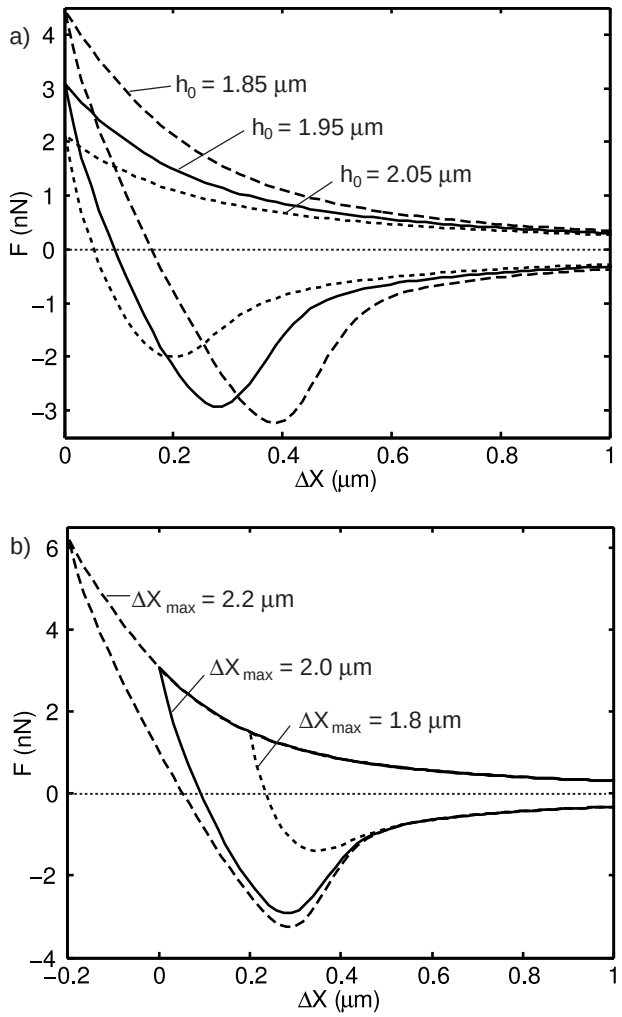

Figure 3.4: Force curves for: a) Initial separations h_0 = 1.85, 1.95, and 2.05 μm. Note that ΔX is defined to give the maximum force at the origin. b) Total displacements ΔX_{max} = 1.8, 2.0 and 2.2 μm.

for $\Delta X = 1.8$, 2.0 and 2.2 μm keeping h_0 fixed at 1.95 μm apart. It is important to point out that the attraction force does not go deeper than the curve for $\Delta X_{max} = 2.3$ μm even for longer pushes. The repulsive force during approach keeps increasing but, during retract, the curves meet each other and go together up to the end of the process.

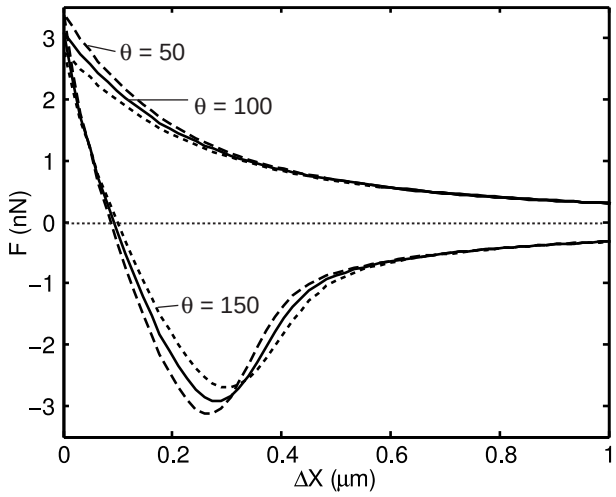

Figure 3.5: Force curves considering variations on the initial contact angle in the cantilever: $\theta = 50°$, 100° and 150°.

The contact angle θ_1 between the drop and the piezo can be measured experimentally and is around 50°. The contact angle between the drop and the cantilever had to be guessed and was chosen in order to give the best agreement. As seen in Figure 3.5, the results are not too sensitive even to large changes in the initial contact angle. Higher contact angles correspond to greater drop volumes – the initial radius of curvature is kept constant here but as the initial contact angle increases, the drops become a larger fraction of a sphere. For larger contact angles, the larger drops can 'back off' more, leading to thicker films and lower forces, both repulsive and attractive. It is important to point out that drops with small contact angles ($\theta \lesssim 30°$) are harder to be solved by the model because the portion of the drop on the piezo will be shorter than the computational domain needed to get accurate results.

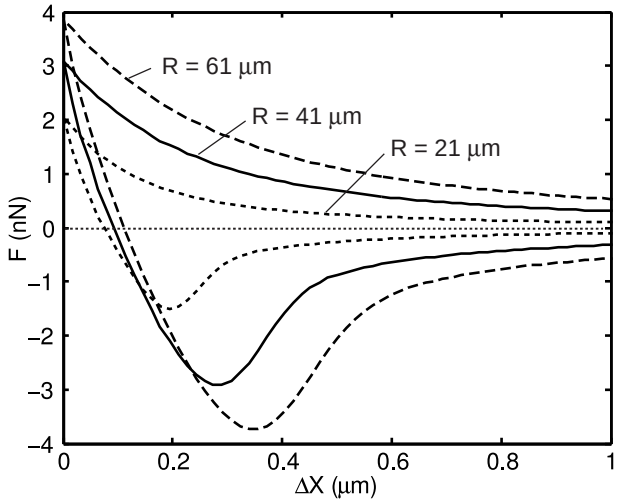

Figure 3.6: Force curves for different drop radius attached to the cantilever: R_c = 21, 41 and 61 μm

The radii of the drops play an important role in this problem. In the regime of drop sizes and velocities used in AFM experiments, surface tension forces are sufficiently strong (very small capillary numbers) to prevent the occurrence of a dimple in the drop surface during interaction. However, when the drop size is increased by 1 – 2 orders of magnitude, dimpling will occur as a result of hydrodynamic interactions. Figure 3.6 shows comparisons changing the radius of the drop in the cantilever. As can be seen, the radius has a considerable effect in the force curve: smaller radius result in smaller hydrodynamic interaction forces and big radius result in bigger interaction forces in a longer range of displacement. The harmonic mean radius is used in the calculations, being most of the influence given by the drop with the smaller value. Therefore, we present the sensitivity by changing the value of the radius of the drop in the cantilever.

The addition of SDS to the system decreases the interfacial tension of the drops [56]. Results presented in Figure 3.7 show that the interaction force is strongly sensitive to differences in surface tension. Higher surface tensions represent stiffer drops and therefore higher forces are needed to deform them. Floppier drops deform earlier and easier generating lower forces but over a

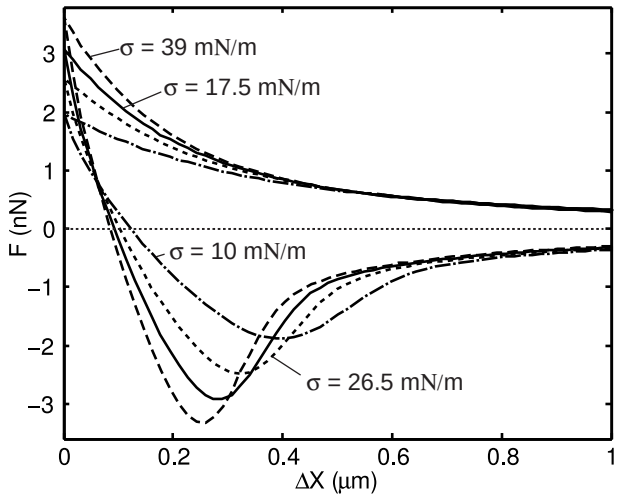

Figure 3.7: Force for $\sigma = 10$, 17.5, 26.5, and 39 mN/m

wider range of displacement. If similar approach and retract calculation were carried out with rigid surface (or infinite surface tension) where there is no deformation, the approach branch of the force curve would rise steeper and reach a higher magnitude. Upon the reversal of the piezo stage velocity, the retract branch of the force curve would be a mirror image of the approach branch about the $F = 0$ axis. Thus as the surface tension of the drop decreases, the attractive minimum in the retract branch would be shallower and will be located nearer the point $\Delta X = 0$.

Figure 3.8 shows the effects of introducing a Navier slip length compared with a experimental run. For really low slip length b values, let say 2 nm, it is hard to distinguish the difference comparing to no-slip but when b becomes higher than 5 nm the force curves are driven away from the experimental one. With the introduction of slip, the thin liquid film can drain much faster both in during approach and out during retract generating much weaker repulsive and attractive hydrodynamic forces.

Although the attractive minimum is due to hydrodynamic effects, the nature of the disjoining pressure Π can also affect the depth of this minimum in the range of drop size and velocity range we have studied. Within the current range of parameters, the distance of closest approach is controlled

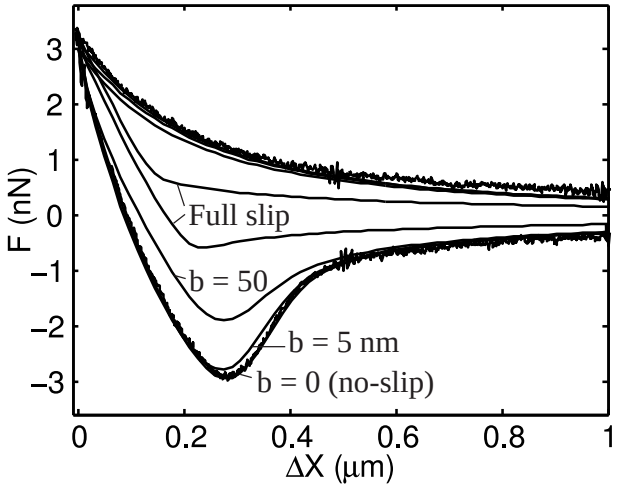

Figure 3.8: Comparisons between experiment and results using different Navier slip lengths $b = 0$ (no-slip), 5 nm, 50 nm and ∞ (full slip).

by the magnitude of the repulsive disjoining pressure. If this is reduced say by decreasing the Debye length, this will allow the two drop surface to come closer together on approach. On retraction, the hydrodynamic drainage flow associated with a thinner film will result in a deeper attractive minimum in the retraction branch of the force curve.

3.5 Predictions of the model

The comparisons presented attest the accuracy of the model in predicting force *vs* displacement curves as measured using the AFM. Moreover, the model provides insight into the dynamical behaviour of the drop surface during interaction and can also quantify the interplay between surface forces, hydrodynamic interactions and surface deformations during drop-drop interaction.

For this study, we use the experimental parameters extracted from Dagastine et al. [29]. Here, the initial separation is $h_0 = 0.7$ μm, the velocity V ranges between 0.16 μm/s and 13.2 μm/s for $\Delta X_{max} = 0.9$ μm. The three-phase contact line at the base of the drop is assumed to be fixed at r_1 and

the unperturbed contact angle is assumed to be $\theta = 90°$ for both drops. The harmonic mean radius of the drops is $R_0 = 41$ μm and will be used to scale the force.

3.5.1 Forces at low velocities

A convenient way to visualise the behaviour of the system is to plot both (F/R_0) and the distance of closest approach $h(0,t)$ between the two drops as a function of time as has been done in Figure 3.9. It is evident that a low speed – 0.16 μm/s, $h(0,t)$ tracks the piezo stage displacement initially until the undeformed drops are about to come into contact (point labelled A). Then $h(0,t)$ stops decreasing relatively abruptly at $h(0,t) = h_{min} \sim 0.026$ μm between $t \sim 4 - 7$ s. During this time interval the force (F/R_0) increases and then decreases almost linearly with time. Salient points along the force curve are labelled A – D and the corresponding drop profiles and pressure profiles are given as a function of radial position in Figure 3.10.

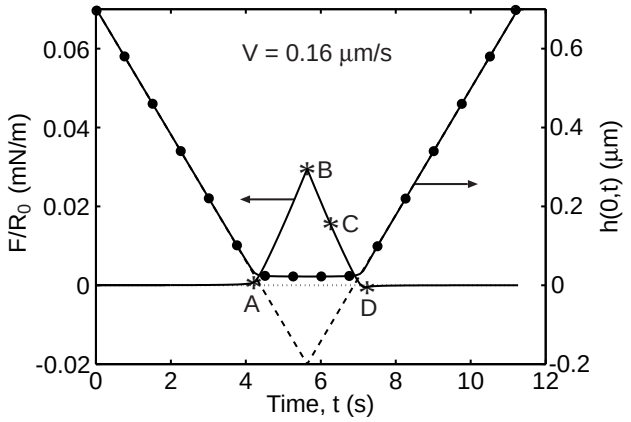

Figure 3.9: The force (solid curve), piezo stage position (broken curve) and central film thickness (•) as a function of time, on approach and withdrawal. Approach velocity is 0.16 μm/s.

Turning first to the drop profiles, Figure 3.10a, we see that there is significant flattening of the drop surfaces at points B and C. At the point of maximum force, point B, the radial extent of the flattened regions is ~ 1

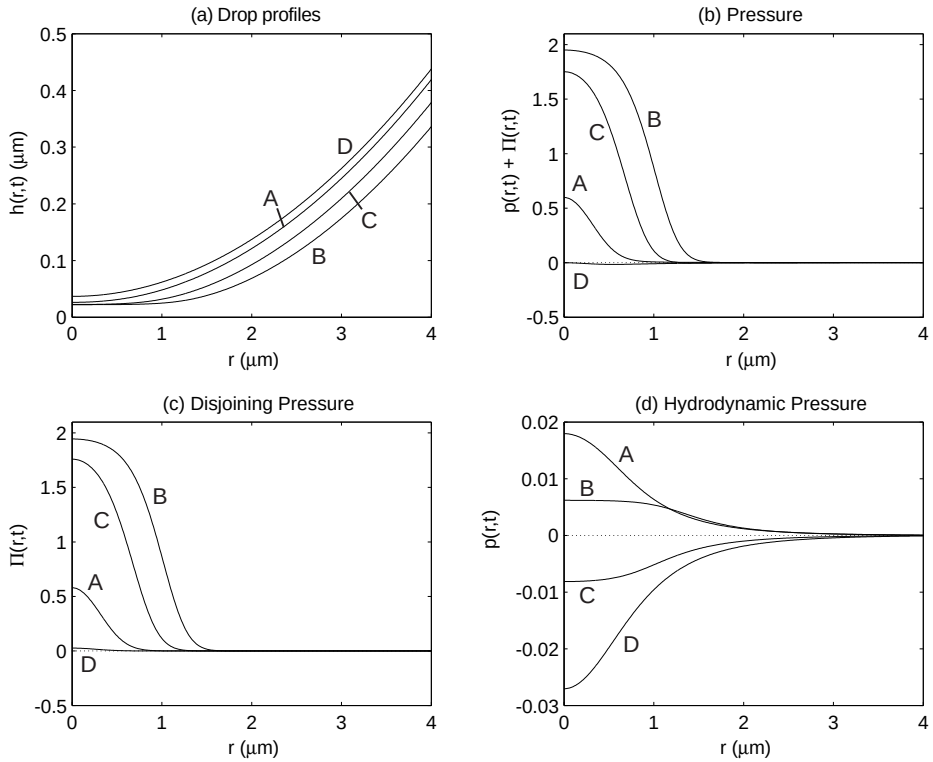

Figure 3.10: The film profiles (top left), film pressure profiles (top right), disjoining pressure profiles (bottom left) and hydrodynamic pressure profiles (bottom right) at 4 selected stages of approach followed by withdrawal. Pressure values are scaled by σ/R_0. Approach speed is 0.16 μm/s.

μm or about 5% of the undistorted radius. Outside this flattened region, for instance at points A and D, the drop profile is very close to parabolic. At low velocities, the general behaviour of the drop surface during interaction is clear: the drops approach each other as almost undeformed surfaces until the separation h_{min} when disjoining pressure due to surface forces $\Pi(h_{min})$ is equal to the Laplace pressure $2\sigma/R_0$. The distance of closest approach then remains approximately constant and the drop surfaces flatten to increase the effective area of interaction. It is this increased area of interaction that contributes to the increase in the observed repulsive force. Thus force measurements in this regime sample colloidal forces at relatively large separations

(see Figure 3.14).

The total pressure profile as well as the separate contributions to the pressure from electrical double layer and hydrodynamic interactions are detailed in Figure 3.10b-d. In this low velocity case, the pressure is due almost entirely to surface forces that arise from electrical double layer interactions and this is in accord with that observation that there is little hysteresis in the approach and retract traces. The hydrodynamic pressure profile has a larger range in the radial direction than the disjoining pressure profile, but the magnitude is smaller by a factor of 100. Also the magnitudes of the hydrodynamic pressure at points B and C are smaller than that at points A and D (Figure 3.10d) because the velocities of the drop surfaces at B and C are lower.

3.5.2 Forces at high velocities

At high speed (13.2 μm/s) as shown in Figure 3.11, the drop separation $h(0,t)$ no longer tracks the displacement of the piezo stage closely. At the point labelled A when the undeformed drops are about to come into contact, the repulsive force is almost 40% of the maximum value. There is also considerable asymmetry in the function $h(0,t)$ about the point velocity reversal. However, between the force maximum (point B) and minimum (point D), $h(0,t)$ is nearly constant with a value of around 0.026 μm which is very close to that in the low speed result. At the force maximum, point B, the value of $h(0,t)$ at low (0.16 μm/s) and high (13.2 μm/s) speeds are similar and the radial extent of flattening of the drop surface is also comparable between the two cases, see Figures 3.10a and 3.12a. However, the pressure profile at this point in the high speed case has significant contributions from both electrical double layer forces and hydrodynamic effects. Although the magnitude of the pressure profile from electrical double layer forces is slightly larger, it is of shorter range in the radial direction compare to the hydrodynamic contribution – and the latter has the characteristic r^{-4} algebraic decay.

At point C where the net force is zero, the shorter ranged (in the radial extent) repulsive contribution to the pressure profile from surface forces is

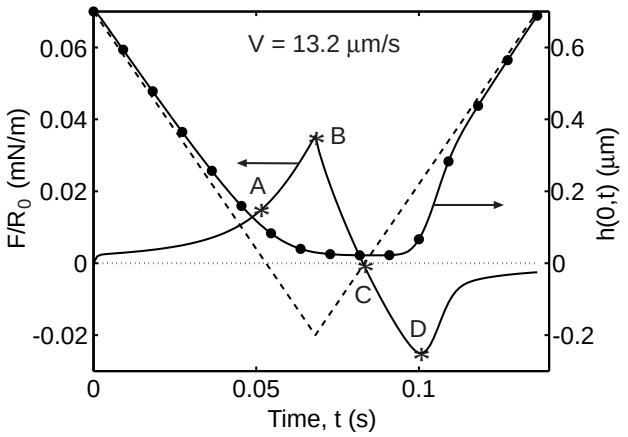

Figure 3.11: The force (solid curve), piezo stage position (broken curve) and central film thickness (•) as a function of time, on approach and withdrawal. Approach velocity is 13.2 μm/s.

balanced by the longer ranged (in the radial extent) attractive contribution from hydrodynamic interactions. Also at point C the portion of the interface for which $r \lesssim 1$ μm are close together than that at the force maximum (point B). However the portion of the interface for which $r \gtrsim 2$ μm are further apart at point C than at point B. This implies that during the initial part of the retract phase the velocity of the drop interface changes sign along the interface – see results in Figure 3.15 for details.

At point D, where the force between the drops is at the attractive minimum, the drop surfaces are at a separation (~ 0.1 μm) where surface forces are negligible compared to the hydrodynamic attraction, Figure 3.12c,d. It is interesting to observe that the drop profiles at point D are pulled in closer to each other in the region around the point of closest approach ($r \lesssim 2$ μm) by the attractive hydrodynamic interaction, Figure 3.12a.

In Figure 3.13, we quantify the deviations of the drop surface from an apparent parabolic profile along the retract branch, at a velocity of 13.2 μm/s. It is clear that the magnitudes of the deformations are small compared to the drop size and are consistent with the small deformation treatment we have used in this model to separate the inner and outer solutions. Between

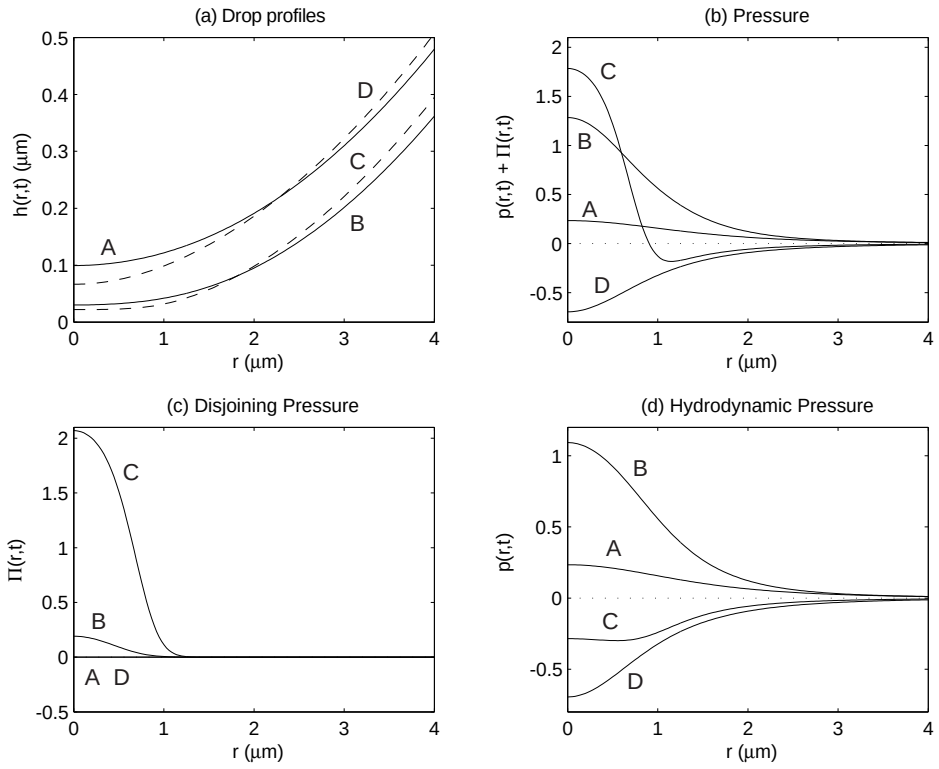

Figure 3.12: The film profiles (top left), film pressure profiles (top right), disjoining pressure profiles (bottom left) ad hydrodynamic pressure profiles (bottom right) at 4 selected stages of approach followed by withdrawal. Approach speed is 13.2 μm/ s.

the force maximum (point A) and the force minimum (point D) the drop surfaces change from being in compression to being in extension.

In Figure 3.14, the results are presented in terms of the force scaled by the drop radius (F/R_0) as a function of the distance of closest approach $h(0,t)$ for the three velocities considered. In all three cases, the force curves rise sharply at $h(0,t) = h_{min} \sim 0.026$ μm, the separation at which the disjoining pressure from surface forces is balanced by the Laplace pressure of the drop. The attractive hydrodynamic minima extend to larger separations as the speed increases.

Insight about the dynamical behaviour of the drop surface can also be

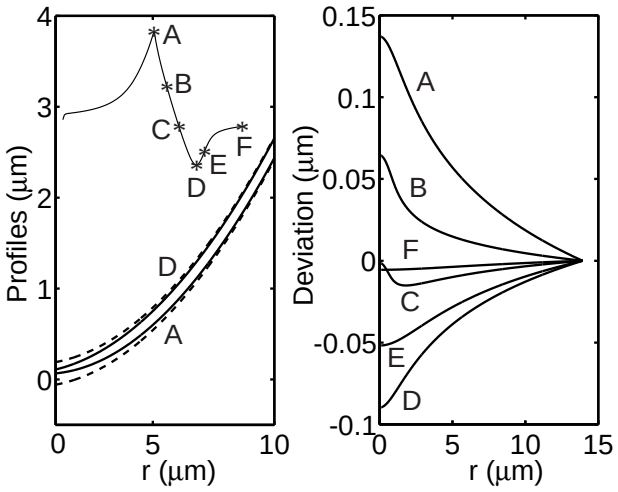

Figure 3.13: Profiles (solid) with parabolic approximation (dashed) (left) and deviation of the profiles compared to a parabolic approximation (right) for $V = 13.2$ μm/s

obtained from this model. In Figure 3.15, we show the velocity profile of the drop surface at various points in the inner region of the drop surface along the approach and retract traces of the force curves at 13.2 μm/s.

- Along the approach branch, when the interaction between the drops become significant, the region of the drop surface near the point of closest approach ($r \sim 0$) becomes nearly stationary – curves C and D in Fig. 3.15.

- During the early part of the retract trace, the central parts of the drop surfaces at small r are still approaching each other while the parts at large r are retracting – curve E in Fig. 3.15. When the net force is zero between the two drops (point F) the central portion of the drop surface remains almost stationary.

- However, at the force minimum (point H) the velocity of the surfaces near $r = 0$ begins to exceed – in magnitude – the retracting speed of the piezo stage. Indeed, shortly after the force minimum (point I) the entire inner part of the drop surface develops a velocity overshoot and

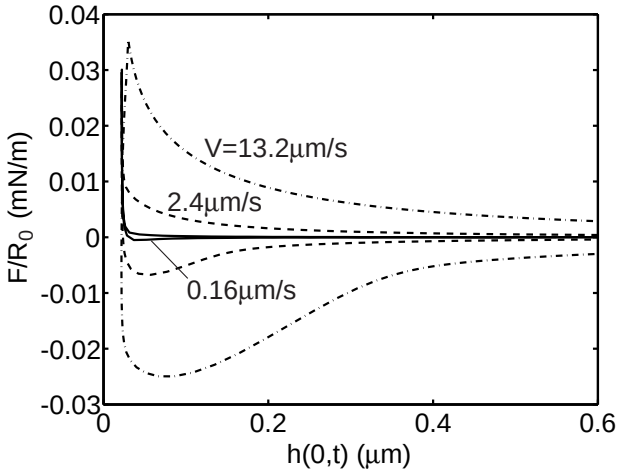

Figure 3.14: The force between two drops as a function of closest approach $h(0,t)$. Approach speeds are 0.16 (solid), 2.4 (broken) and 13.2 (dash-dotted) μm/s

retracts faster than the speed of the piezo stage.

- Eventually, the whole drop surface does attain the velocity of the piezo stage as expected (points J to L).

We should note that the observed velocity overshoot of the drop surface describe above cannot occur without a proper matching of the inner solution of the drop profile to the outer solution that gave the proper boundary conditions for $\partial h/\partial t$ as given in Eq. (2.110).

We have modeled the oil/water interface populated with surfactants simply as a deformable surface with a specified surface tension. Effects related to surfactant transport within the interface and between the interface and the bulk solution are omitted. Having obtained numerical results with our simple model we can return to examine the validity of omitting surfactant transport effects. We can calculate the magnitude of hydrodynamic shear forces at the oil/water interface in the thin drainage film (the inner region) as follows. In the lubrication approximation, the shear rate at the fluid interface $\dot{\gamma}$ is given by

$$\dot{\gamma} = -\frac{h}{2\mu}\frac{\partial p}{\partial r} \tag{3.1}$$

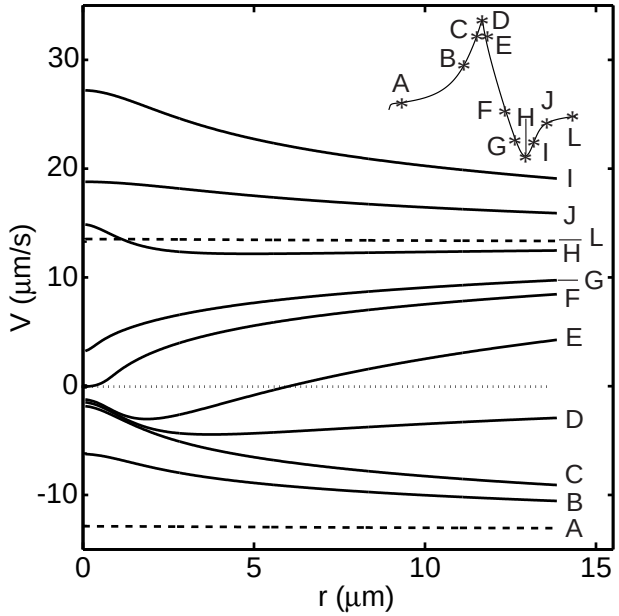

Figure 3.15: Velocity profiles of the drop surface along the approach and retract traces of the force curve for $V = 13.2$ μm/s.

because u_r has the usual parabolic dependence on z. Results show that the shear stress is of the order 3 N m^{-2}, the same order of magnitude as found in ref. [47] for much larger drops. For the present inner region the hydrodynamic shear stress exerts a shear force of around 10^{-11} N. This shear force is small compared to the interfacial tension force acting on the perimeter of the inner region which is estimated to be 5x10^{-8} N from an interfacial tension of 8 mN m^{-1}. Therefore, surfactant transport as a result of hydrodynamic shear is likely to be insignificant.

Figure 3.16 presents shear rate ($\dot{\gamma}$) results for a typical run. In this case positive shear rates mean that the bathing liquid is flowing out from the interaction zone and negative flowing in. During approach the shear rate grows as the drops get close to each other. At early stages of retraction the shear rates are still positive meaning that the drop is approaching for as concluded previously through the velocity of the film. At some stage there are regions in which the flow goes in one direction and regions on the opposite.

At a later stage, the liquid is flowing in to fill the gap that was left.

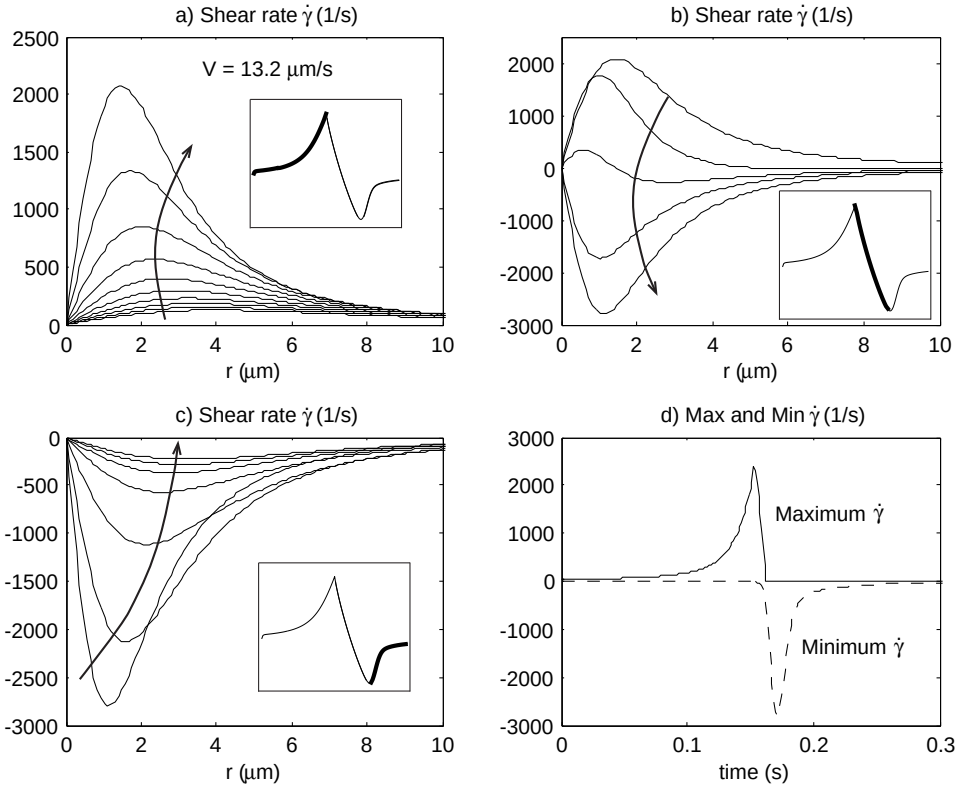

Figure 3.16: Shear rate $\dot{\gamma}$ for a typical run using $V = 13.2$ μm/s and 10 mM SDS concentration. a) During approach from $t = 0$ to 0.15 s. b) Early stage of retract from $t = 0.15$ to 0.17 s. c) Late stages of retract from $t = 0.17$ to 0.3 s. The inset force curve show the range covered on the plot and arrows indicate growing time. d) Maximum and minimum shear rate values evolving with time.

Finally we observe that we do not need to invoke the existence of a slip length or slip boundary condition that appears to be required to fit similar AFM measurements conducted between interacting solid surfaces. One possible explanation for this is that at small separations, surface roughness that is present at solid surfaces renders the treatment of the film drainage by a lubrication approximation inappropriate and therefore a slip boundary condition has to be invoked as a heuristic correction. For fluid interfaces such surface roughness effects may not be an important issue.

Chapter 4

Drop-sphere Interaction in AFM

Colloidal interaction forces between rigid particles and deformable interfaces are of concern in many industrial and chemical processes such as froth flotation and solvent extraction, and are of great importance in the food processing and personal care industries where the stability of complex emulsions is crucial. In recent years, many experiments as well as theoretical developments have been performed involving the static interaction between a colloidal particle and a drop [6, 55, 65, 38, 2, 9, 15, 56] or bubble [34, 12, 61] using adaptations of the Atomic Force Microscope. Aston and Berg [3] were the first to observe hydrodynamic repulsion and attraction when a small particle is driven and retracted from an oil drop of radius about 2.5 mm. They also pointed out that a drop or bubble cannot be treated as a perfect Hookean spring as used in early works [34]. This observation is also one conclusion of the present work and will be shown in Chapter 7.

In this chapter we compare our theoretical model with recent experiments involving the interaction of a silica colloidal sphere (radius $\sim$ 10 μm) and a deformable drop (radius $\sim$ 50 μm) in AFM performed by Webber et al. [72]. To model the drop-sphere interaction, we use Eqs. (2.40), (2.41) and (2.60) together with initial condition Eq. (2.42) and boundary conditions Eq. (2.37) and (2.111) presented in Chapter 2.

The only unknown of the experiment is the initial separation between the drop and the particle, which can be accurately extracted from the model. The addition of 5 mM of SDS is known to lower the surface tension of the system and immobilise the oil/electrolyte interface. Experimental measured and theoretical parameters used for the comparison are summarized in Table 4.1 together with experimental tolerance of the measured values. All the parameters for the theory correspond to the experimentally measured values inside the error band.

Physical parameter	Experiment	Theory
Drop surface tension, σ (mN/m)	10	8.5
Drop surface potential, ψ_0 (mV)	-100 $\pm$ 10	-100
Sphere surface potential, ψ_0 (mV)	-40 $\pm$ 10	-40
Electrolyte concentration (mM SDS)	5 $\pm$ 0.01	5
Viscosity (water), μ (mPa s)	0.89	0.89
Drop radius, R_d (μm)	50 $\pm$ 5	55
Sphere radius, R_s (μm)	10 $\pm$ 2	12
Drop contact angle, θ	58° $\pm$ 5°	55°
Cantilever spring constant, K (mN/m)	16 $\pm$ 1.5	17
Maximum piezo travel, ΔX_{max} (μm)	2	2
Piezo drive velocity, V (μm/s)	1 – 23	1 – 23
Initial separation, h_0 (μm)	unknown	1.5

Table 4.1: Experimental and theoretical parameters of the drop-sphere interaction in an AFM.

In Figure 4.1 we present a comparison between experimental measured forces and theoretical forces using the model for three different velocities. The agreement is reasonable for all cases showing the ability of the model in predicting drop-particle interactions. We observe that the hydrodynamic repulsion and attraction strongly depend on velocity, a result also seen for the interaction between two deformable drops (see chapter 3). Moreover results

show that for $\Delta X < -0.2$ μm the slopes of the force curve during approach and retract are the same for all three velocities and are on top of each other (see inset). We point out that when the particle is far away from the drop the latter is hardly deformed and the force curves can be well predicted by the classical Reynolds theory for the interaction between two solid spheres.

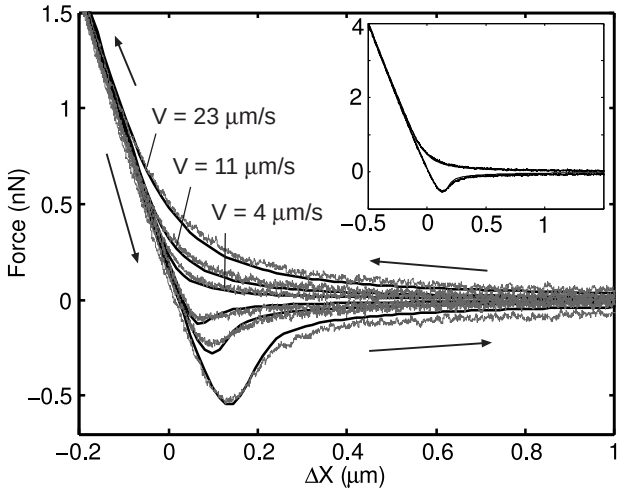

Figure 4.1: Force versus displacement from AFM experiments (grey lines) and theory (black full lines) for nominal drive velocities $V = 4$, 11 and 23 μm/s in the region where the repulsive approach branches and retract branches with attractive minima corresponding to different velocities are more evident. Results over the full measured force range are shown in the inset. See Table 4.1 for experimental and theoretical parameters.

Given the good agreement between theory and experiment, we are now able to use the model to provide more information about the drop-particle system that cannot be measured experimentally. In Figure 4.2 we show the variation of the velocity of the interface for two different positions, where interesting features can be seen. At the centre of symmetry $r = 0$ the velocity decreases during approach and remains equal to zero while the interfaces are separated by a thin film of constant thickness and when the drop is retracted it shows an overshoot of almost twice the retract velocity. At $r = r_{max}$ where our new boundary condition is applied we see that even though

the sphere is approaching with velocity V = -23 μm/s the velocity at that position is less than half the velocity of approach. Just after the reversal the velocity changes sign but still lower that the retract velocity and later it also overshoots. This behaviour of the velocity at $r = r_{max}$ can only be obtained by using the boundary condition derived in this work. All the other points inside the computational domain would show similar behaviour being all the lines concentrated inside the ones that have been shown.

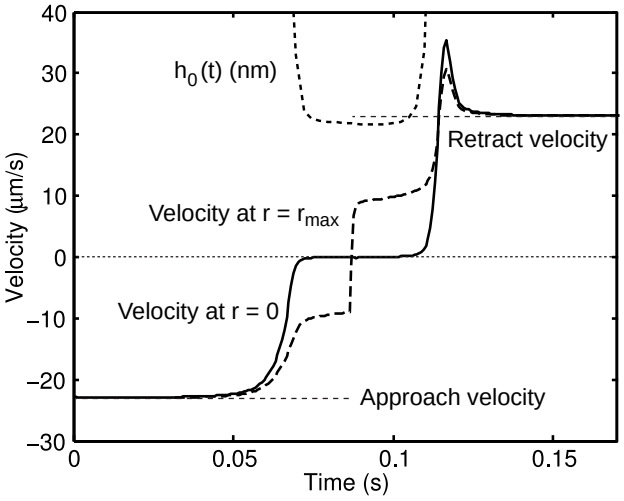

Figure 4.2: Variation of the interfacial velocity of the drop ($\partial h/\partial t$) at $r = 0$ (full line) and at $r = r_{max}$ (dashed line) and the central thickness of the film $h(0, t)$ for V = 23 μm/s where we define negative V as approach and positive as retract.

For this interaction between a drop and a solid sphere we can easily recover the shape of the drop during interaction since the sphere does not deform. In Figure 4.3 we look at the macroscopic scale of the system in which we plot the relative position of the drop approaching the solid sphere from the initial separation until the reversal of the motor. Note that the radius of the particle (12 μm) is smaller than the radius of the drop (55 μm) and in this scale it appears that the drop is just touching the sphere. We can only see deformation of the drop in the last few interface profiles that are close to the particle when we see that deformation of the drop is long range. The amount of wrapping of the drop around the particle is small compared to

deformation as will be seen in the next figure.

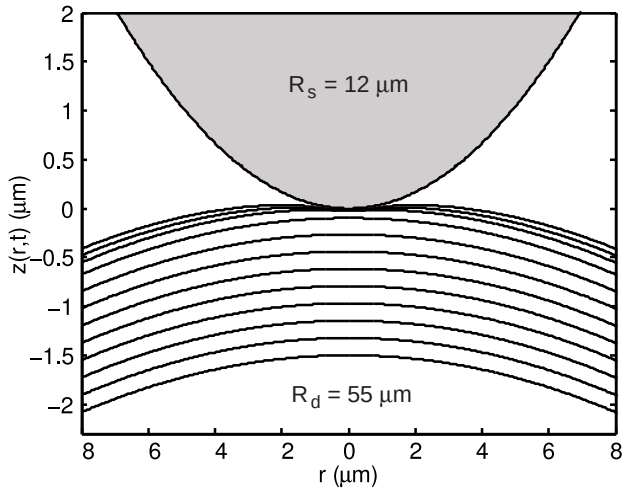

Figure 4.3: Variations of the drop profile during the course of interaction with the particle. The radial extent of the interaction zone is less than 2 μm compared to the particle radius of 12 μm. Over the interaction zone, the parabolic approximation to the particle shape is adequate.

In Figures 4.4a and 4.4b, we show details of the profiles $z(r,t)$ the fluid interface as predicted by the model during the approach and retract phases. From Figures 4.4c and 4.4d we see that the thickness, $h(r,t)$ of the aqueous film between the drop and the particle is no less than at $h_f \sim 22$ nm, which is the separation when the internal pressure equates the disjoining pressure given by the condition $\Pi(h_f) = (2\sigma/R_p)$ where $\Pi(h)$ in the present system is the disjoining pressure due to electrical double layer repulsion between the drop and the particle. We observe that unlike the case of the interaction between a mercury drop and a mica surface, the film thickness, $h(r,t)$ for the present particle-drop system shows no signs of a dimple within the range of current experimental parameters.

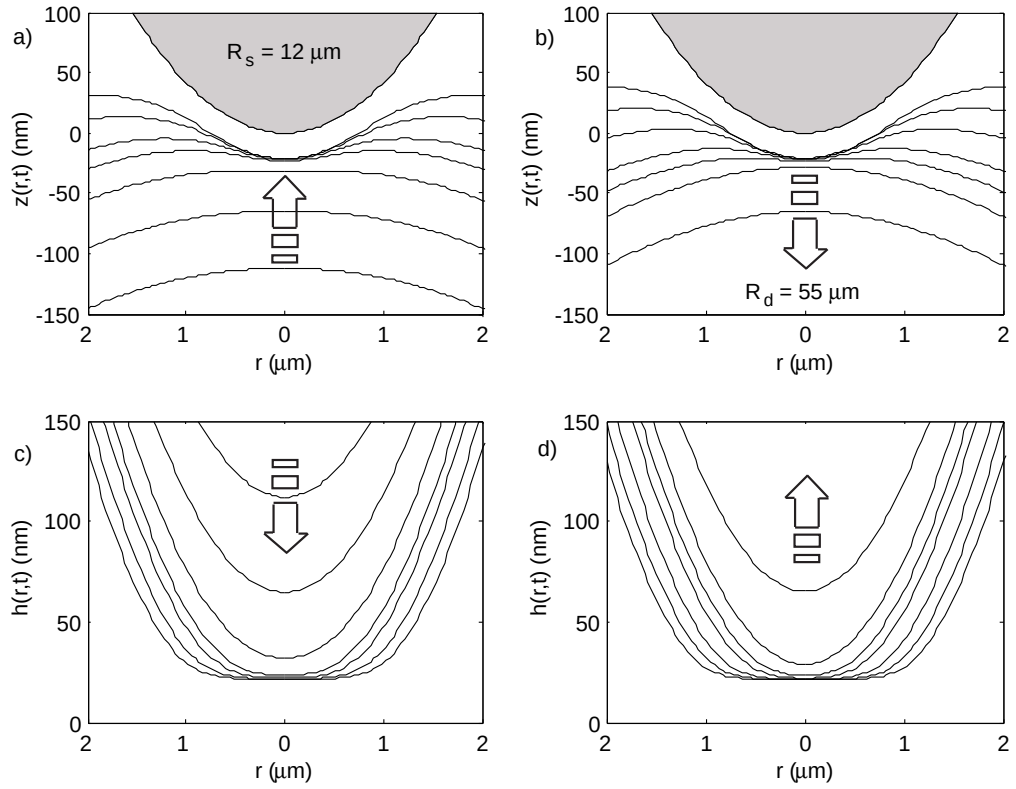

Figure 4.4: Time variations of the calculated drop profile $z(r,t)$ during (a) the approach phase and (b) the retract phase. The corresponding thicknesses of the aqueous film between the drop and the particle during (c) approach and (d) retract are also shown.

4.1 Discussion

The approach and retract velocities are now functions of time taking into account new experimental data which measure the position of the cantilever as a function of time. Using this extra information we were able to extract the actual velocity of approach and retract. Figure 4.5 shows the velocity as a function of displacement in which we can see that what was believed to be almost constant is changing significantly from 19 to 25 μm/s during approach and from 17 to 26 μm/s during retract. This experimental velocity can easily be implemented in the model, but we observed that by using a mean velocity of about 23 μm/s for this particular case in the comparison

between theory and experiment would make slight visual difference in the agreement when compared to using the plotted velocity.

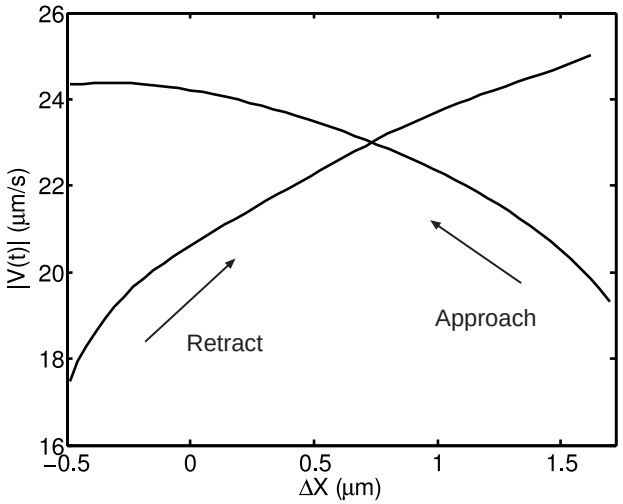

Figure 4.5: Velocity of approach and retract extracted from experimental data. The nominal velocity was set to be $V = 20$ μm/s but it is growing both during approach and retract. Note that we plot the magnitude of the velocities for visual reasons; the approach velocity is negative according to our definition.

In early works [13, 28], we assumed that the velocity was constant and we used the nominal values. This new information help us to better understand how the experimental system is behaving and can improve our predictions in future works involving interaction using the Atomic Force Microscope.

Chapter 5

The dimple experiment in SFA

5.1 Introduction

This chapter presents comparisons between the theory developed in this thesis for drop-wall interaction and the experiments performed by Connor and Horn [25] using the Surface Force Apparatus (SFA). Good agreement will be shown for the wimple formation for attractive and repulsive situations.

A schematic representation of the Connor-Horn SFA experimental system is shown in Figure 5.1. White light optical interference between reflections from the silver and mercury surfaces is analysed with the aid of a spectrometer, which allows the silver-mercury distance and hence the aqueous film thickness h to be determined over a range of r, where r is the horizontal distance from the symmetry axis passing through the top of the drop. Readers should consult the original paper [25] for full details. A mercury drop is formed at the top of a sealed capillary of radius 1.5 mm immersed in an aqueous electrolyte solution of 0.1 mM KCl. At this electrolyte concentration, the mica surface has a surface potential of -100 mV [59]. The potential difference between the mercury and a reference calomel electrode in the bulk electrolyte can be adjusted by an external potential source. As a result, the equilibrium dissimilar electrical double layer interaction between the mica and the mercury surface can be made to be repulsive or attractive.

Detailed experimental studies have been undertaken for four cases of such

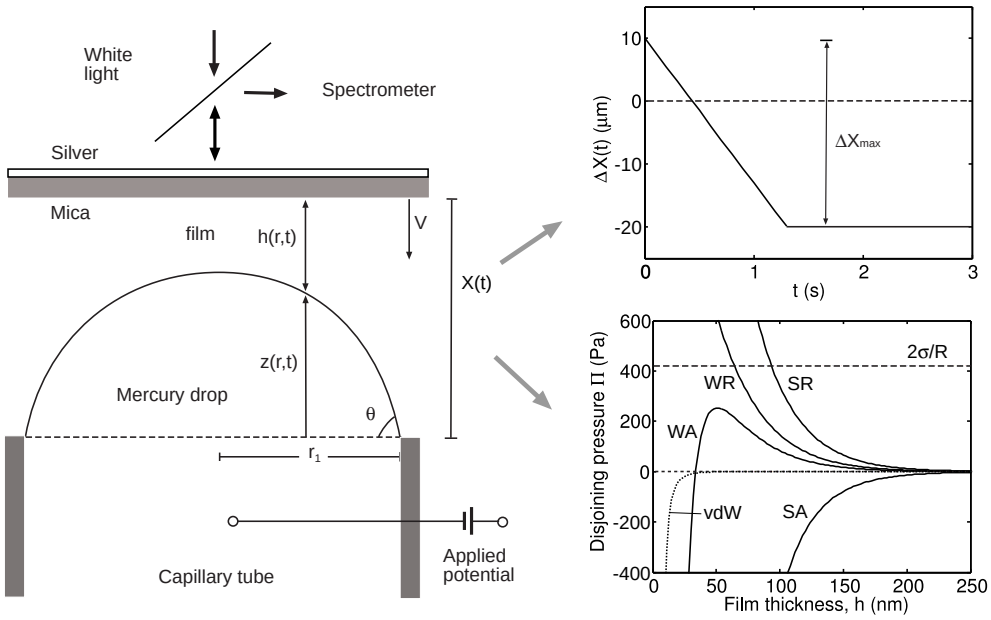

Figure 5.1: Schematic diagram of a mica surface approaching a mercury drop. Top inset: Variations of the position of the mica with time. Bottom inset: Disjoining pressures due to electrical double layer interaction designated as Strongly Repulsive (SR), Weakly Repulsive (WR), Weakly Attractive (WA) and Strongly Attractive (SA) as calculated from the non-linear Poisson-Boltzmann theory. The disjoining pressure due to van der Waals forces is shown in the dotted line and the magnitude of the Laplace pressure ($2\sigma/R$) is indicated by the horizontal dashed line.

interactions, designated as Strongly Repulsive (SR), Weakly Repulsive (WR), Weakly Attractive (WA) and Strongly Attractive (SA). The force per unit area or the disjoining pressure, $\Pi(h)$ of these four cases as functions of the separation, h, between a flat mica and a flat mercury surface are shown in the inset of Figure 5.1. The non-linear Poisson-Boltzmann theory is used to calculate these results. In comparison to the electrical double-layer interactions, the magnitude of the attractive van der Waals interaction is negligibly small at the range of film thicknesses of interest (>50 nm). For this system, the non-linear Poisson-Boltzmann theory is able to account accurately for measurements of equilibrium film thickness [24].

The capillary radius r_1 is 1.5 mm, but with slight flattening of the mercury

drop due to gravity, the radius of curvature, R, of the mercury at the apex is measured to be 1.9 mm. The interfacial tension, σ of the mercury/electrolyte interface is 426 mN/m when the applied potential is near its point of zero charge (the WR and WA cases) and slightly lower, 420 mN/m, when the applied potential has a magnitude of $\pm$ $\sim$450 mV for the SR and SA cases. The viscosity μ of the electrolyte is taken to be 0.89 mPa s at a temperature of 25°C. Mercury has a viscosity of 1.53 mPa s.

In the experimental protocol, the (rigid) mica plate is driven towards the fixed mercury drop at a constant velocity, V (nominally 23 μm/s but as high as 67 μm/s in one case) for a total travel distance ΔX_{max} that ranges from 15 to 30 μm from an initial distance of closest approach h_0 that varies between 5 to 20 μm. Thus the mica plate is driven towards the mercury surface for around one second and is then held at the final position. In response, the mercury/electrolyte interface is observed to deform in an axially symmetric manner and the separation between the mercury surface and the mica surface, $h(r,t)$ can be deduced from variations of the shape of the FECO with position and time. The separation $h(r,t)$ can be determined with sub-nanometre resolution in the direction normal to the mica surface and micrometre resolution in the r direction.

At large separations, the mercury/electrolyte interface has a near parabolic shape with the point of closest approach at the axis of symmetry ($r = 0$). As the separation decreases, the interface will develop a characteristic dimple shape [35, 37, 33] where the minimum separation between the mica and the mercury will no longer be at the axis of symmetry. Instead, the minimum separation will occur at a radial distance r_{rim} (> 0) at what is sometimes called barrier rim. If the disjoining pressure is sufficiently repulsive, the mercury interface will eventually be flattened by its interaction with the mica surface and separated from it by an equilibrium aqueous film of thickness h_{eq}. If the disjoining pressure is sufficiently attractive at small separations, the aqueous film will drain away completely and the mercury surface will collapse onto the mica surface. In approaching either final state, hydrodynamic pressures in the film cause the mercury/electrolyte interface to exhibit the familiar dimpling at intermediate separations.

5.2 Theoretical and experimental parameters

Theoretical results are computed using the model outlined in Chapter 2. Input parameters are taken from independent measurements or literature values and these are summarised in Table 5.1 together with values used to give theoretical results using our model. The surface potentials for 3 different cases: SR, WA, and SA are obtained by subtracting a constant from the applied potential, which was shown in [24] to account correctly for the equilibrium drop profile according to the non-linear Poisson-Boltzmann model.

Physical parameter	Experiment	Theory
Surface force parameters		
Mica surface potential,	-100 ± 10 mV	-100 mV
Drop surface potential,	-492 ± 20 mV (SR)	-492 mV
	-12 ± 20 mV (WA)	-24 mV
	408 ± 20 mV (SA)	408 mV
Electrolyte concentration, n	0.1 ± 0.01 mM KCl	0.11 mM KCl
Fluid properties		
Viscosity (water), μ	0.89 mPa s	0.89 mPa s
Drop surface tension, σ	426 mN/m (SR, SA)	426 mN/m
	420 mN/m (WA)	420 mN/m
Drop radius, R, at apex	1.9 ±0.02 mm	1.9 mm
SFA parameters		
Maximum mica travel, ΔX_{max}	30 ± 3 μm	24 – 29 μm
Drive velocity, V	23 or 67 ± 2 μm/s	24 or 67 μm/s
Initial separation, h_0	10 ± 0.1 μm	10 μm

Table 5.1: Experimental and theoretical parameters of the mercury-mica system in the Surface Force Apparatus.

It was reported in [25] that mica was driven towards mercury at a constant speed of 23 μm/s for a set time. In fact the actual velocity drive func-

tion of the mica has a small rise and decay time with a linear acceleration and deceleration ramp. According to the manufacturer of the Nanomover$^{(R)}$ microstepping motors used for the mica drive (Melles Griot, USA) the acceleration and deceleration rates are 458 μm/s^2. These transients in the velocity function are included as input to our computation although the effect is only significant when the nominal velocity is high (around 67 μm/s). However, it is found that the drive stop times t_{stop} (when the mica velocity reaches zero) required to fit the data – or equivalently, the maximum mica travel – differ from those quoted in Ref. [25] in which the deceleration ramp was neglected (see Table 6.1).

In the next sections we present comparisons between theory and experiments. Section 5.3 shows the results for the strong repulsive case; different initial separations and approach velocities are also analysed. In Sections 5.4 and 5.5 we consider attractive systems in which the mercury drop jumps into the mica. Some predictions of the model are presented in Section 5.6 and the chapter closes with a discussion.

5.3 Strongly Repulsive (SR) disjoining pressure

In Figure 5.2a we compare experimental measurements and theoretical predictions of the mica-mercury separation $h(r,t)$ for the case in which the interaction is a monotonic strong repulsion – the Strongly Repulsive (SR) case (see Figure 5.1). The experimental results are cross sections of an almost perfectly axisymmetric deformation profile. In the experiment, the mica surface, initially at a separation of $h_0 = 10$ μm from the mercury/electrolyte interface, is driven towards the mercury interface at a nominal constant velocity $V = 23$ μm/s for a total displacement $\Delta X_{max} = 30$ μm. The theoretical curves are calculated using $V = 24$ μm/s for a total displacement $\Delta X_{max} = 27.1$ μm; these values are within experimental error of the nominal values.

The mica-mercury separation $h(r,t)$ during later stages of the approach is shown in Figure 5.2a when the aqueous film thins down from a thickness

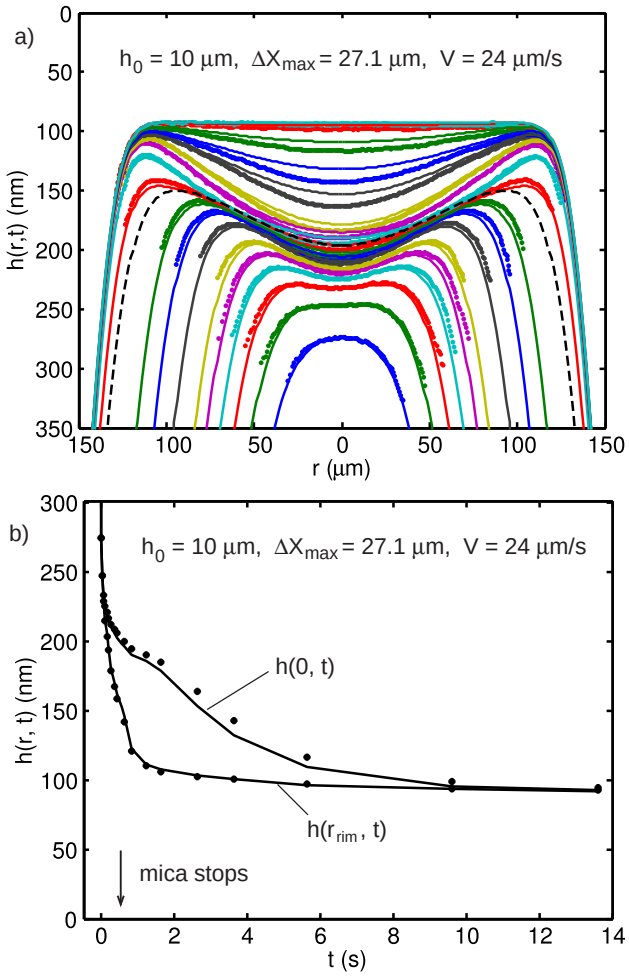

Figure 5.2: Comparison between theory (lines) and experiment (dots) for the Strongly Repulsive (SR) case. a) Drop profiles $h(r,t)$ - from bottom to top: t = -0.02, 0.02, 0.06, 0.10, 0.14, 0.18, 0.26, 0.34, 0.42, 0.555 (dashed curve, without data points – mica stops), 0.62, 0.82, 1.22, 1.62, 2.62, 3.62, 5.62, 9.62 and 13.62 s. Note that $t = 0$ corresponds to the time at which the curvature of the profile at $r = 0$ changes sign. b) Film thickness at the center $h(0,t)$ and at the barrier rim $h(r_{rim},t)$. The initial separation h_0, mica travel ΔX_{max} and mica velocity V are indicated in the figure. Again, the dots denote experimental results.

of about 300 nm to the final equilibrium thickness of about 100 nm. The time value associated with each $h(r,t)$ profile is relative to the reference time $t = 0$ at which the curvature of mercury/electrolyte interface at $r = 0$ is observed to change sign and signals the formation of a dimple. There is an uncertainty of one video half frame or $\pm$ 0.02 s in determining the value of this reference time.

Our calculations show that at $t = 0$ where $h(0,t) \sim 300$ nm, the mica surface has already travelled 14 μm, so with an initial separation of $h_0 = 10$ μm, the apex of the mercury drop has already deformed by 4 μm by this time. From $t = 0$ onwards we see that the curvature of the mercury/electrolyte interface changes sign and begins to develop the familiar dimple shape with the associated development of a barrier rim at position $r = r_{rim}$. Although the mica drive stopped after $t_{stop} = 0.555$ s, where the corresponding profile $h(r, t_{stop})$ is given by the dashed line in Figure 5.2a, the dimple continues to develop as the deformation relaxes to its equilibrium shape. The thinning profile maintains a high degree of axial symmetry which justifies our use of an axisymmetric theory to describe the problem.

A comparison of the variation with time of the observed and predicted film thickness at the center of the dimple $h(0,t)$ and at the barrier rim $h(r_{rim},t)$ is given in Figure 5.2b. Note that the thickness at the barrier rim $h(r_{rim},t)$ decreases faster with time than the film thickness $h(0,t)$ at the center of the dimple. The interface then takes a further 10 seconds to attain equilibrium after the mica has stopped moving at $t = 0.555$ s.

At large times the dimple resolves to an equilibrium flat film with thickness h_{eq} equal to the separation at which the disjoining pressure due to electrical double layer repulsion is equal to the Laplace pressure of the mercury drop: $\Pi(h_{eq}) = 2\sigma/R$.

In Figure 5.3 we show similar profiles of the mercury/electrolyte interface for the SR case but with different initial mica-mercury separations, different total displacements of the mica and different mica velocities. In all cases the agreement between experiment and theory is very good with the possible exception for the portion of $h(r,t)$ near $r \sim 0$, for times after the development of the dimple where theory predicts that the film thins too rapidly.

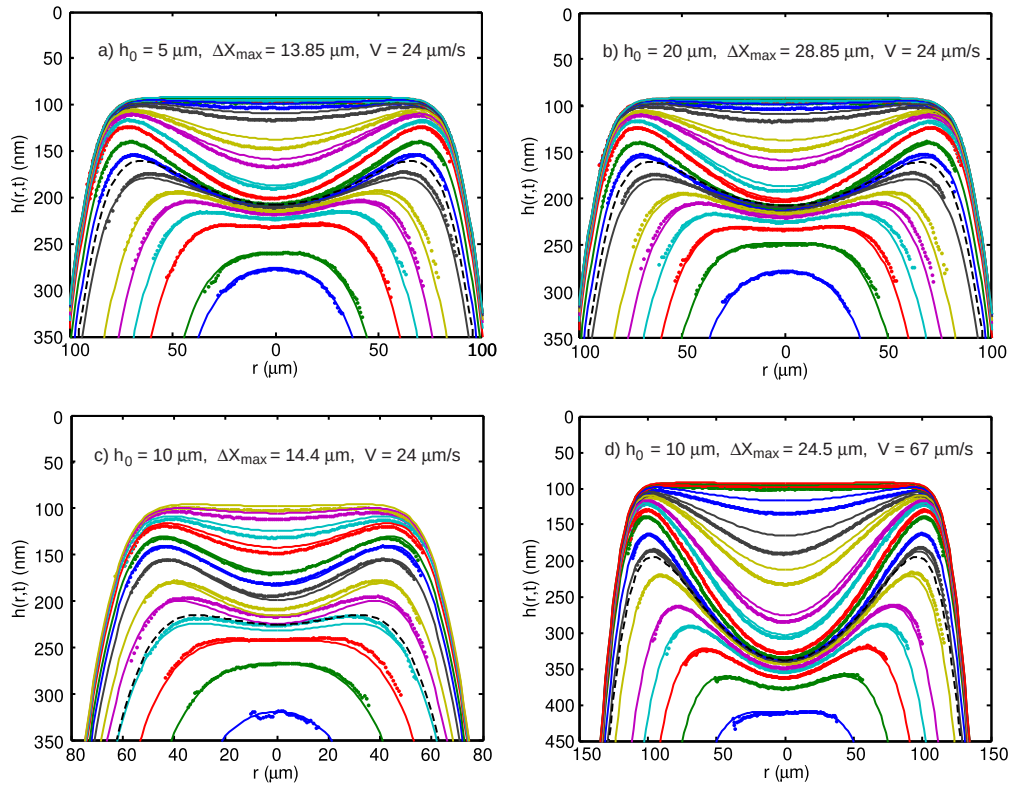

Figure 5.3: Comparison between theory (lines) and experiment (points) of the mercury/electrolyte interfacial profile $h(r,t)$ for the Strongly Repulsive (SR) case at various combinations of initial separations h_0, total mica travel ΔX_{max} and mica velocity V. The dashed curves are theoretical profiles at the instant that the mica drive stops in the computation and they have no corresponding data points. From bottom to top: a) t = -0.02, 0., 0.06, 0.10, 0.14, 0.18, 0.26, 0.313 (dashed curve – mica stops), 0.34, 0.42, 0.62, 0.82, 1.22, 1.62, 2.62, 3.62, 5.62, 9.62, and 13.62 s. b) t = -0.02, 0., 0.06, 0.10, 0.14, 0.18, 0.26, 0.313 (dashed curve – mica stops), 0.34, 0.42, 0.62, 0.82, 1.22, 1.62, 2.62, 3.62, 5.62, 9.62, and 13.62 s. c) t = -0.04, 0, 0.04, 0.08, 0.088 (dashed curve – mica stops), 0.12, 0.16, 0.24, 0.32, 0.4, 0.6, 0.8, 1.2, and 1.6 s. d) t = 0, 0.04, 0.08, 0.12, 0.16, 0.24, 0.293 (dashed curve – mica stops), 0.32, 0.4, 0.6, 0.8, 1.2, 1.6, 2.6, 3.6, 5.6, 9.6, and 13.6 s.

Note that the allowance of a partial slip hydrodynamic boundary condition at the mica/electrolyte or mercury/electrolyte interface would only increase the divergence between experiment and theory. We will suggest a plausible

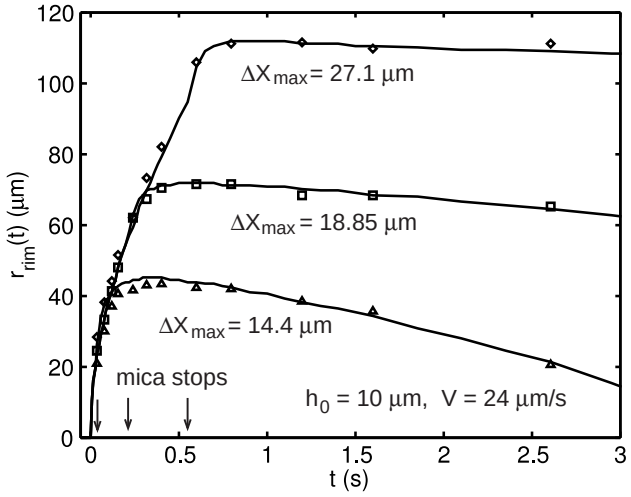

Figure 5.4: Variations of the barrier rim position $r_{rim}(t)$ with time: experimental results (symbols) and theory (lines) from an initial mica-mercury separation $h_0 = 10$ μm, and a mica velocity $V = 24$ μm/s. The distance travelled by the mica is indicated in the figure and correspond (from top to bottom) to results shown in Fig. 5.2a, 5.3b, and 5.3c respectively. Arrows indicate the stopping times.

explanation for this discrepancy in the Discussion section. In any event, the volume of electrolyte enclosed within the barrier rim differs by less than 4% between the experimental and theoretical profile shapes.

In Figure 5.4, we show the variation of the position of the barrier rim r_{rim} with time for the SR case for three different total displacements of the mica surface. In all cases the agreement between experiment and theory is very good. At small times, r_{rim} increases like $t^{1/2}$ as observed in the constant velocity case [47].

The calculated total pressure profile that comprises the hydrodynamic pressure p and the disjoining pressure Π profiles within the film at various stages of thinning are shown in Figure 5.5. Results for the decomposition of the total pressure into the hydrodynamic and the electrostatic disjoin-

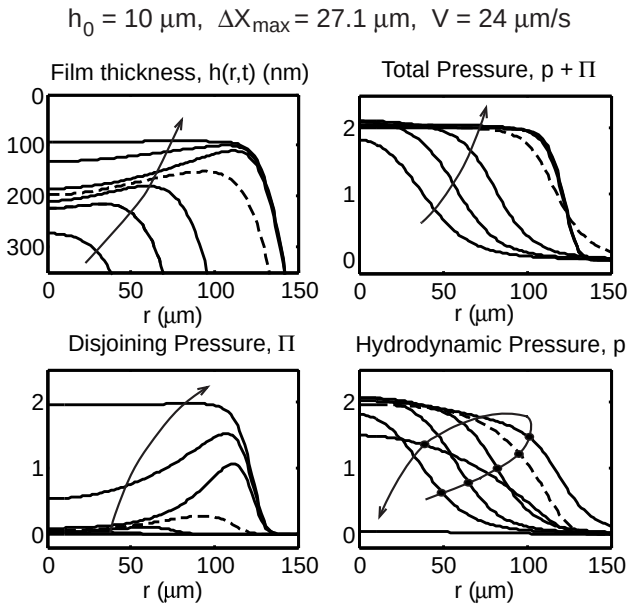

Figure 5.5: Variations of the hydrodynamic pressure p, disjoining pressure Π, and total pressure $(p+\Pi)$ for the Strongly Repulsive (SR) case with initial separation $h_0 = 10$ μm, mica travel $\Delta X_{max} = 27.1$ μm and mica velocity $V = 24$ μm/s (same parameters as results in Figure 5.2): t= -0.02, 0.1, 0.26, 0.555, 1.22, 3.62, and 13.62 s. The arrow indicates increasing time. The dashed curve corresponds to the time when the mica stopped.

ing pressure components are shown in separate panels. As already noted from analysis of the experimental data [39], we observe that while the relative contributions to the total pressure from hydrodynamic effects and from electrostatic effects vary significantly during the thinning process, the total pressure, being the sum of these two contributions, remains remarkably constant across the extent of the film throughout the film thinning process. This can perhaps be expected because variations of the film thickness which are of the order of 100 nm, are small compared to the deformation zone which is ~ 200 μm in radial extent. The radial deformation zone is in turn only a small fraction of the mercury drop which has dimensions on the mm scale (see Section 5).

5.4 Strongly Attractive (SA) disjoining pressure

In the Strongly Attractive (SA) case, the mercury interface is positively charged so the electrical double layer interaction with the negative mica surface gives a disjoining pressure that is monotonically attractive (see Figure 5.1). A comparison between experimentally observed profiles of the mercury/electrolyte interface $h(r,t)$ with theoretical predictions using the data in Table 1 is given in Figure 5.6a.

In this case, instead of forming a stable equilibrium film, the mercury surface collapses onto the mica surface because of the strongly attractive disjoining pressure. This collapse is very rapid as the observed jump of the mercury/electrolyte interface into contact with the mica surface occurred within one video frame of the last recorded profile at $t = 0.64$ s (see Figure 5.6). The predicted theoretical profile at $t = 0.66$ s (corresponding to the next video frame) is also shown in Figure 5.6 to illustrate that the barrier rim has jumped 50 nm or more towards the mica surface. In reality, it is expected that the rupturing process of the trapped dimple is likely to occur in an asymmetric manner that will not be reproduced in an axially symmetric model considered here. Nonetheless the agreement between theory and experiment before the jump-in is gratifying, as is the fact that the theory predicts accurately the time at which the film collapse occurs.

From the results in Figures 5.2a, 5.6a, and 5.6b, we can see that at large separations ($h \geq 200$ nm), the mercury interfaces are almost identical for the SR and SA cases. This is in accord with the disjoining pressure results in Figure 5.1 where for the SA case, the electrical double layer attraction only becomes significant below about 200 nm and demonstrates that deformations in this large separation regime are only dependent on the long ranged hydrodynamic interactions.

In Figure 5.6b, we compare experimental time variations of the film thickness at the center of the dimple, $h(0,t)$, and the film thickness at the barrier rim $h(r_{rim},t)$ with theoretical predictions. Again the agreement is very good.

The pressure profiles calculated from our theory that correspond to the

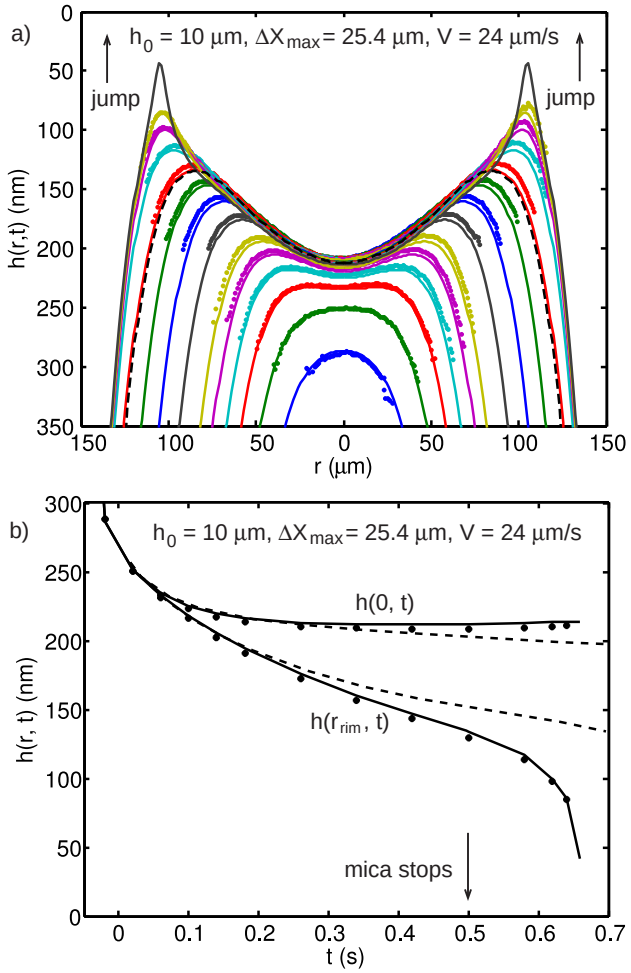

Figure 5.6: Comparison between theory (lines) and experiment (points) for Strongly Attractive (SA) disjoining pressure. a) Drop profiles $h(r,t)$ from bottom to top: t = -0.02, 0.02, 0.06, 0.1, 0.14, 0.18, 0.26, 0.34, 0.42, 0.497 (dashed – mica stops), 0.5, 0.58, 0.62, and 0.64 s. The theoretical profile at the next video frame at $t = 0.66$ s is also shown. b) Film thickness at the center $h(0,t)$ and at the barrier rim $h(r_{rim},t)$. The experimental results for the Strongly Repulsive (SR) case (dashed lines) are included for comparison.

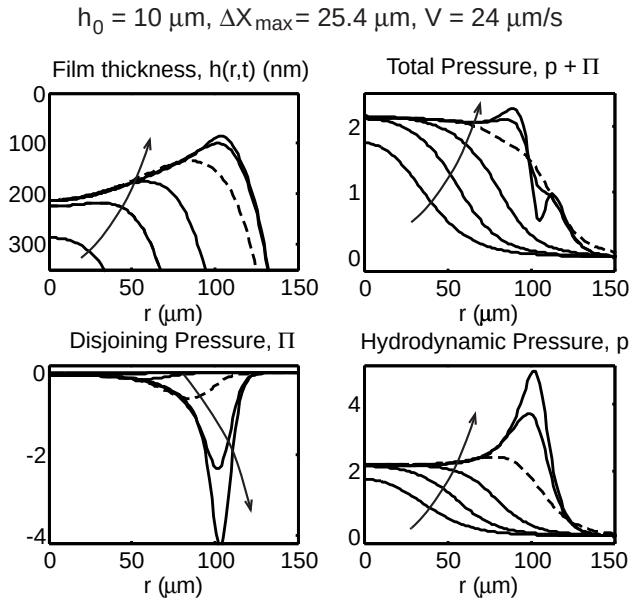

Figure 5.7: Variations of the hydrodynamic pressure p, disjoining pressure Π, and total pressure $(p+\Pi)$ for the Strongly Attractive (SA) case with initial separation $h_0 = 10$ μm, mica travel $\Delta X_{max} = 25.4$ μm and mica velocity $V = 24$ μm/s (same parameters as results in Figure 5.6): t = -0.02, 0.1, 0.26, 0.497 (dashed - mica stops), 0.62, and 0.64 s. The arrow indicates increasing time.

Strongly Attractive case are shown in Figure 5.7. We observed that up until just prior to the collapse of the dimple, the total pressure remains essentially constant even though individually the hydrodynamic and disjoining components begin to show large spatial variations which mutually cancel [39].

5.5 Weakly Attractive (WA) disjoining pressure

The comparison between experiment and theory for the Weakly Attractive case is given in Figure 5.8. In this case, the disjoining pressure curve is repulsive at large separations, possesses a small maximum at around 50 nm that is less than the Laplace pressure of the drop (see Figure 5.1) and is

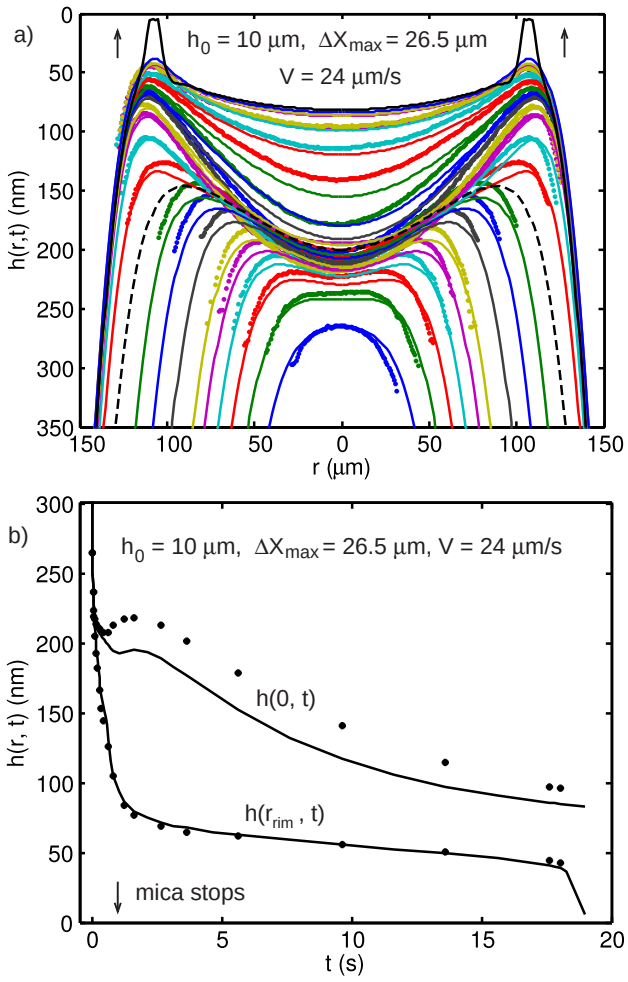

Figure 5.8: Comparison between theory (lines) and experiment (points) for the Weakly Attractive (WA) disjoining pressure. a) Drop profiles from bottom to top: t = -0.02, 0.02, 0.06, 0.1, 0.14, 0.18, 0.26, 0.34, 0.42, 0.51 (dashed – mica stops), 0.5, 0.58, 0.62, 0.82, 1.22, 1.62, 2.62, 3.62, 5.62, 9.62, 13.62, 17.62, 18.02, and 19 s. b) Film thickness at the center $h(0,t)$ and at the barrier rim $h(r_{rim},t)$.

attractive at separations below about 40 nm. While the mica surface was driven towards the mercury drop at constant velocity for about one second and was then stopped, the drainage process continued further for about 18 seconds before the film collapsed – a time that is predicted accurately by the theory. The agreement between theory and experiment at intermediate times during the film drainage process is not as close as for the Strongly Repulsive or Strongly Attractive cases, but the calculations still reproduce all the features reasonably well, including a 'bounce' in which h_0 increases for a short time after the drive stops. No bounce occurs in the SA or SR cases, but it is observed in both the data and the computation for the WA case.

5.6 Predictions of the model

The comparisons given in the previous section provide compelling evidence that our theoretical model is capable of providing an accurate description of the thin film drainage process under the action of repulsive and attractive surface forces. We can now interrogate the model for information that was not accessed or is not accessible experimentally.

The experimental profiles show nanometre dimpling in a millimetre mercury drop relative to the mica surface. Using the model we can quantify the relative extent of the deformations by viewing the deforming drop on different length scales. The key features are illustrated in Figure 5.9 for the Strongly Repulsive (SR) interaction. In the rear panel the drop is shown on a millimetre scale which makes it clear that the deformation and interaction zone are confined to a region of ~ 300 μm in radius which is small compared to the size of the drop. Moreover, on this scale, it appears that the mercury drop and the mica are in contact. In the middle panel of Figure 5.9 we show the drop profiles drawn on the 100 μm scale. Once again, on this scale, mica and the mercury drop seem to be in contact and dimpling of the mercury/electrolyte interface is not yet visible. The nanometre scale dimpling and film thickness, as measured in the experiment, are shown in the front panel of Figure 5.9.

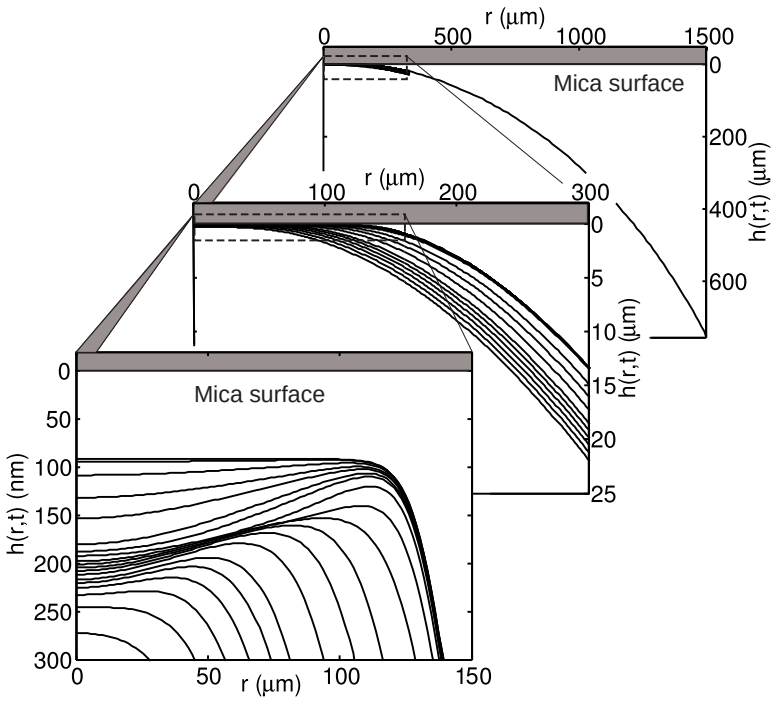

Figure 5.9: Views of the deforming mercury/electrolyte interface on different length scales to illustrate nanometre deformations on a millimetre drop for the Strongly Repulsive case: initial separation $h_0 = 10$ μm, mica travel $\Delta X_{max} = 27.1$ μm, and mica velocity $V = 24$ μm/s for t = -0.02 to 13.62 s.

The amount of deformation in the mercury interface, that is, the difference in height between the actual interface and its undeformed spherical shape, as time evolves is shown in Figure 5.10 for the Strongly Repulsive case. As can be seen, when the first experimental profile is measured the mercury drop has already deformed about 4 μm at $r = 0$, since the mica has already travelled for about 14 μm from an initial separation of 10 μm. Note that after the mica has stopped, further deformations of the mercury interface are very small on the micrometre scale shown in Figure 5.10. However, on the nanometre scale the dimple still continues to evolve (see Figure 5.2).

The relative velocity between the mercury/electrolyte interface and the mica is plotted in Figure 5.11. Initially the magnitude of the relative velocity of all parts of the mercury/electrolyte interface is 24 μm/s, which is the

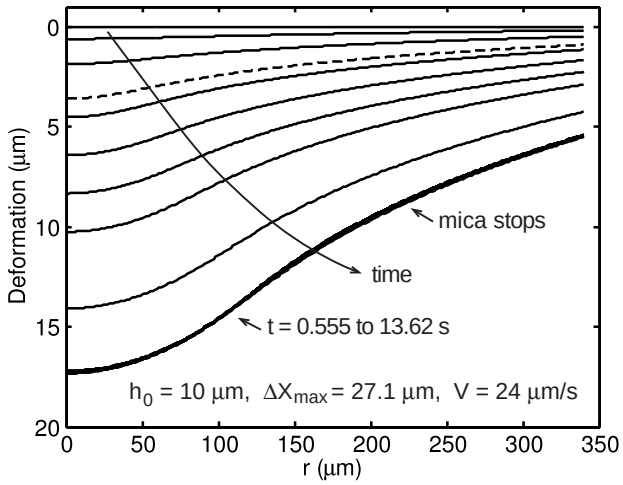

Figure 5.10: Deformation of the mercury interface as the mica approaches for the Strongly Repulsive (SR) case: from bottom to top: t = -0.575, -0.2, -0.1, -0.02 (dashed curve – first experimental profile), 0.02, 0.1, 0.18, 0.26, 0.42, 0.555 (mica stops), 0.62, 0.82, 1.22, 1.62, 2.62, 3.62, 5.62, 9.62, and 13.62 s.

velocity of the mica. As the film thins, the mercury interface starts to deform and the relative velocity in the center of the film decreases in magnitude. By the time the first profile is measured ($t = -0.02$ s) the approach velocity is almost zero in the center while the velocity at r_{max} is around two thirds of the the mica velocity. When the mica stops at $t = 0.555$ s the velocity at r_{max} is about half the the mica velocity. After the mica stops, the magnitude of the relative velocity decreases to values $\ll 1$ μm/s.

5.6.1 Hydrodynamic effects

To illustrate the effects of hydrodynamic interactions in film thinning in our system, we present some theoretical results in the absence of disjoining pressure, $\Pi = 0$ but otherwise under the same experimental conditions as those in Figure 5.2.

In Figure 5.12a we show the evolution of the film thickness under the experimental protocol in which the mica surface is driven at constant velocity towards the mercury drop for a pre-determined time and then stopped. In

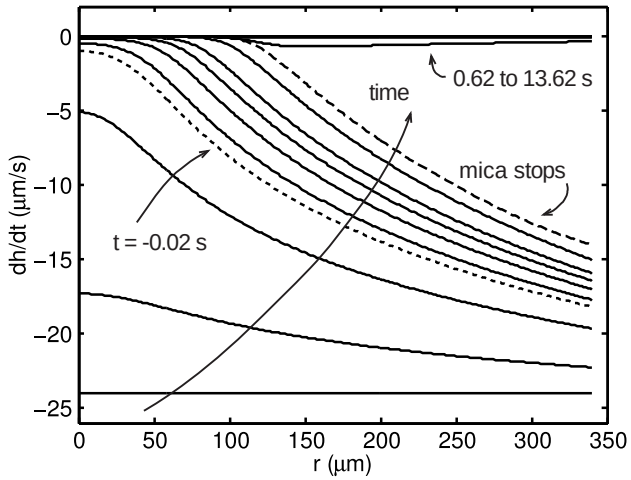

Figure 5.11: Relative velocity of approach between the mercury/electrolyte interface and the mica for the Strongly Repulsive (SR) case: initial separation $h_0 = 10$ μm, mica travel $\Delta X_{max} = 27.1$ μm and mica velocity $V = 24$ μm/s for t = -0.575, -0.2, -0.1, -0.02 (dashed curve – first experimental profile), 0.02, 0.1, 0.18, 0.26, 0.42, 0.555 (mica stops), 0.62, 0.82, 1.22, 1.62, 2.62, 3.62, 5.62, 9.62, and 13.62 s

this case, the aqueous film and dimple that is formed will drain very slowly. In the absence of a repulsive disjoining pressure to maintain a minimum value for the barrier rim thickness $h(r_{rim}, t)$ to facilitate drainage of fluid trapped in the dimple or an attractive disjoining pressure to cause the collapse of the intervening film, the barrier rim thickness thins very slowly and takes $\sim 10^4$ s to reach sub-nanometre thickness beyond which a continuum hydrodynamic model for the intervening film ceases to be valid. An interesting observation, made clear in Figure 5.12b, is that the film thickness at the centre, $h(0, t)$ initially decreases with time as expected, but then increases to a maximum at $t \sim 10$ s and then finally decreases again. Such a maximum or 'bounce' in the behaviour of $h(0, t)$ is detectable in cases where the disjoining pressure in the system is small, such as the Weakly Attractive case shown in Figure 5.8.

A cusp is observed in the plot of $h(r_{rim}, t)$ in Figure 5.12(b) at the point where the mica drive stops. At this time the approach conditions change from constant speed to quasi-constant force. The force between the drop and the mica surface is associated with the macroscopic deformation of the

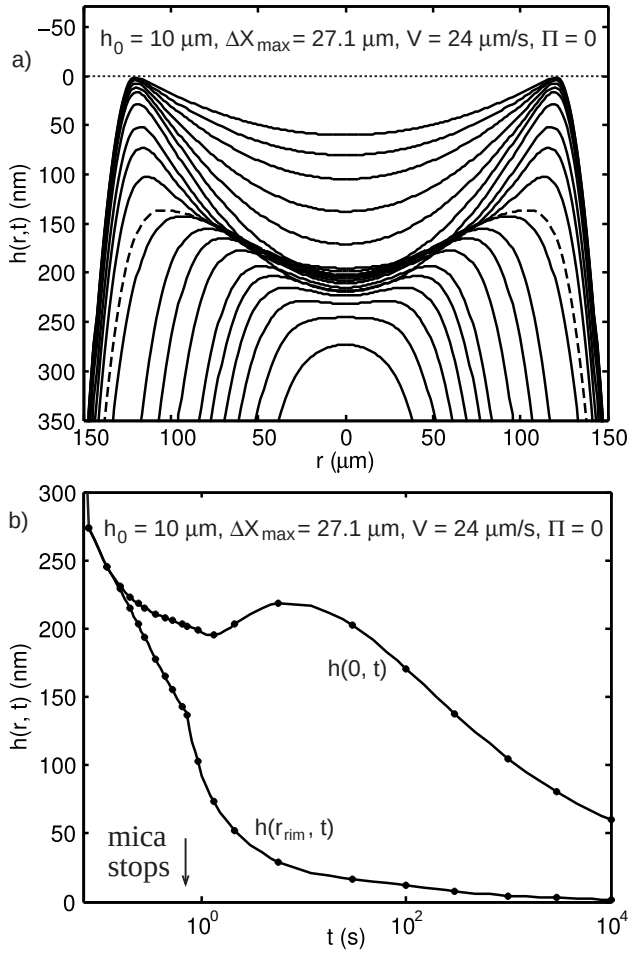

Figure 5.12: Predictions of the evolution of the mercury/electrolyte in the absence of a disjoining pressure ($\Pi = 0$) where the initial separation h_0, the velocity V and the total push ΔX_{max} were chosen to be the same as in the Strongly Repulsive (SR) case (see Figure 5.2). a) Drop profiles from bottom to top: t = -0.02, 0.02, 0.06, 0.10, 0.14, 0.18, 0.26, 0.34, 0.42, 0.555 (dashed curve – mica stops), 0.62, 0.82, 1.22, 2.62, 13.62, 30, 100, 300, 1000, 3000, and 10000 s. b) Film thickness at the center $h(0,t)$ and barrier rim $h(r_{rim},t)$. Dots indicate the time steps plotted in part a. Note the logarithmic scale of t.

drop, which changes very little after the mica stops moving (Figure 5.10). The cusp indicates an increase in the approach rate of the barrier rim when the drive changes from quasi-constant speed to constant force, consistent with the results in Klaseboer et al. [47] and Yiantsios and Davis [76]. This 'closing down' of the barrier rim forces some of the aqueous phase back into the dimple, which has the effect of forcing an increase in h_0 at a slightly later time (the bounce), before the drainage continues again in the usual direction of film thinning.

The stabilizing influence of hydrodynamic interactions is illustrated in Figure 5.13 in which the mica surface is driven continually, without stopping, towards the mercury interface again in the absence of disjoining pressure ($\Pi = 0$). Here we see that at $t = 2.62$ s (the last profile plotted in Figure 5.13) where the mica has traveled 76.7 μm, the film thickness remains over 100 nm but the radial position of the barrier rim continues to increase. Thus the repulsion arising from hydrodynamic interactions alone drastically reduced the film thinning rate.

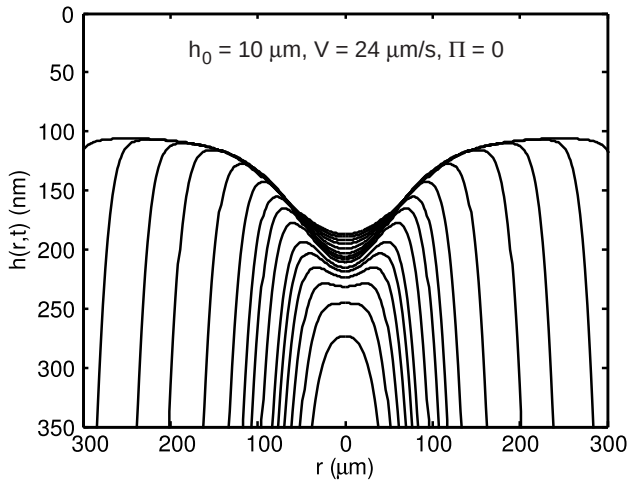

Figure 5.13: Predictions of the evolution of the mercury/electrolyte in the absence of a disjoining pressure ($\Pi = 0$) where the initial separation h_0, the velocity V were chosen to be the same as in the Strongly Repulsive (SR) case (see Figure 5.2), but the mica was driven continuously. Drop profiles from bottom to top: t = -0.02, 0.02, 0.06. 0.10, 0.14, 0.18, 0.26, 0.34, 0.42, 0.62, 0.82, 1.22, 1.62, and 2.62 s.

5.6.2 Shear rates and flow in the film

In Figure 5.14, we present results for the shear rate $(dv_r/dz)(r,t)$ evaluated at the mica/electrolyte interface for the Strongly Repulsive (SR) case. These give insight into details of fluid flow within the draining film. From Figure 5.14a and 5.14b for the shear rate as a function of radial position on the mercury surface we observe that the profile for the shear rate grows in magnitude as the mica surface approaches the mercury drop. The profile reaches a maximum just before $t = 0$ then it starts to decrease because the mean radial velocity in the intervening film begins to fall. During the drainage phase (Figure 5.14b) the shear rate profiles continue to decrease as the drainage process slows down. In Figure 5.14c we show the variation of the maximum value of the shear rate with time. The small maximum in the shear rate at the time when the mica is stopped is a consequence of the discontinuity in acceleration as the mica stops. We see that during the drainage of the dimple across the narrow gap at the barrier rim, the shear rate is less than $10^3\ s^{-1}$. In Figure 5.14d, we present the time variation of the position of the maximum in the shear stress at the mercury surface. We see that after the formation of the dimple the maximum is located close to but slightly outside the barrier rim.

In Figure 5.15, we present shear rate results for the Strongly Attractive (SA) case. The results in Figure 5.15a show similar features as in the SR case during approach. This is expected since double layer interactions are unimportant at large separations during these early times. However, after the mica stops (Figure 5.15b), the magnitude of the shear rate begins to increase significantly. This is caused by the attractive disjoining pressure that, at this stage, is acting to pull the mercury surface towards the mica. The accelerated thinning at the barrier rim due to attractive disjoining pressures increases the shear rate and outflow velocity in the radial position just beyond the barrier rim. However, at radial positions inside the barrier rim the shear rate has become negative so the flow of the intervening fluid is directed towards the center of the dimple at $r = 0$. This radially inward flow then causes the film thickness at the center of the dimple to decrease slower than the SR

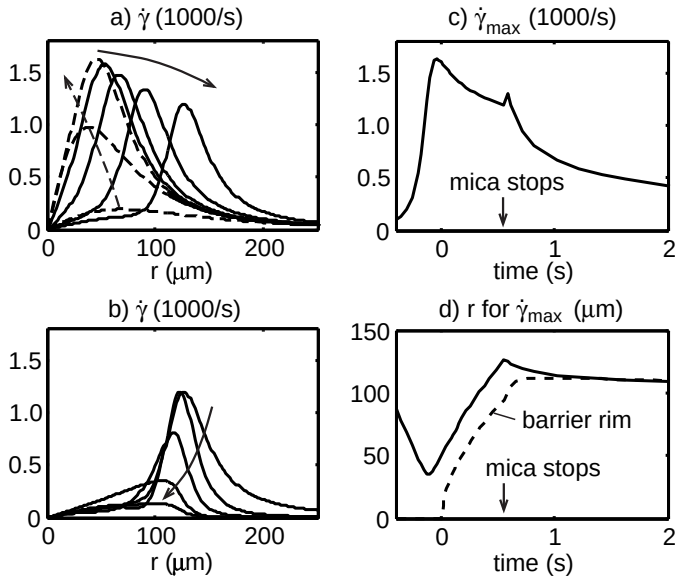

Figure 5.14: Behaviour of the shear rate ($\dot{\gamma}$) at the mercury/electrolyte interface for the Strongly Repulsive (SR) case corresponding to results presented in Figure 5.2. a) During mica approach: t = -0.3, -0.15, -0.02, 0.02, 0.1, 0.26, and 0.555 s (mica stops). The 3 first profiles (dashed lines) correspond to $t < 0$. b) During drainage after the mica has stopped: t = 0.555, 0.62, 0.82, 1.62, and 5.62 s. c) Maximum value of the shear rate ($\dot{\gamma}_{max}$) as a function of time. d) Radial position of the maximum in the shear rate (solid line) and barrier rim (dashed line). The arrows indicate increasing time.

case (see Figure 5.6b). Analysis of shear rates in the calculations without disjoining pressure presented in Section 5.1 also shows a region of negative shear rate close to but inside the barrier rim at times shortly after the drive stop time. Again, this indicates a flow of liquid towards $r = 0$ within the film, as required for the observed bounce in $h(0, t)$ to occur (Figure 5.12).

5.7 Discussion

We have made a detailed comparison between experimental observations and theoretical predictions for the thinning of an aqueous film between an approaching mica plate and a deformable mercury drop under both repulsive

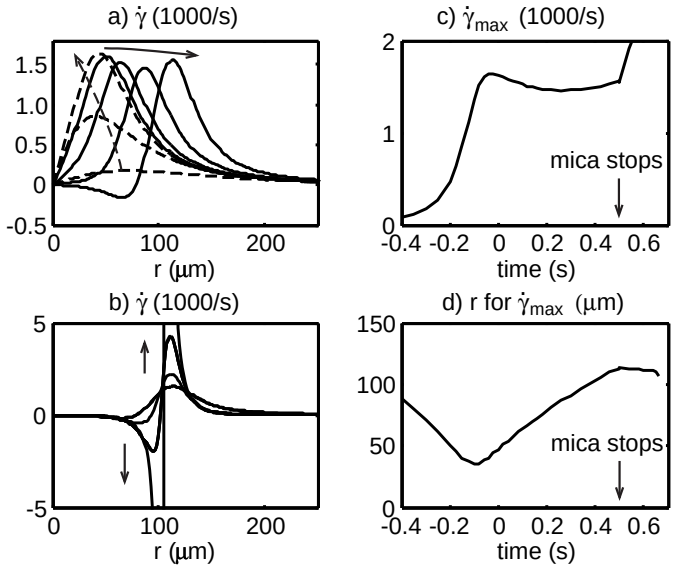

Figure 5.15: Behaviour of the shear rate ($\dot{\gamma}$) for the Strongly Attractive (SA) case from Figure 5.6. a) During mica approach: t= -0.3, -0.15, -0.02, 0.02, 0.1, 0.26, and 0.497 s (mica stops). b) 0.497, 0.58, 0.64, and 0.66 s. c) Maximum value of the shear rate ($\dot{\gamma}_{max}$) as a function of time. d) Radial position of the maximum in the shear rate. The arrows indicate increasing time.

and attractive electrical double layer forces between the interfaces. Like other theoretical models already in the literature, ours is based on the Young-Laplace equation, Reynolds lubrication theory, and the inclusion of a disjoining pressure to account for surface forces. However, an important feature of the present theory is that it includes consideration of the far-field deformation of the fluid drop. As seen in Figure 5.10, the deformation is significant in regions of the drop well beyond the barrier rim, where hydrodynamic pressures are very small and surface forces are negligible. Proper consideration of far-field deformation allows modeling of the experimental situation for any prescribed drive function of a solid approaching a drop that is held at a fixed capillary. More generally, the present approach can be readily extended to other modes of interaction between deformable drops which may be driven by externally imposed flow fields and/or are under the effects of thermal motion.

The theoretical model provides good fits to the experimental data which encourages one to believe that the physics on which it is based is sound and the approximations and assumptions made are reasonable. It is of particular interest that no-slip boundary conditions were required to provide agreement with experimental data, not only at the mica/electrolyte interface but also at the mercury/electrolyte interface. It was noted at the outset that these assumptions were made in the interests of starting with a simple model. The fact that the model has been shown to fit the data gives *a posteriori* justification to the assumptions. In Figure 5.16, we use Eq. (2.136) to compare the time dependence of the central film thickness $h(0,t)$ for various values of slip length b_h at the mercury interface for the SR case while the no-slip ($b_0 = 0$) boundary condition is applied at the mica surface (see also Figure 5.2). Here we see that even with the no-slip condition ($b_h = 0$), the predicted form of $h(0,t)$ already thins a little faster than experimental values. The allowance of any degree of slip only increases the divergence between theory and experiment.

There are a number of reports in the recent literature [57] that purport to show that partial slip occurs at many solid/liquid interfaces and follows the Navier slip boundary condition. Slip lengths ranging from ∼10 nm up to a few micrometres have been reported, although other reports find that the no-slip boundary condition applies within 1 – 2 nm of the solid/fluid interface. Allowing slip at the mica/electrolyte interface ($b_0 > 0$) in our model would make agreement with experiment worse, similar to what is shown in Figure 5.16, since b_0 and b_h are interchangeable in Eq. 2.136. Our results therefore lead to the conclusion that a no-slip boundary condition applies within 1 or 2 nm of the solid/liquid interface, at least for the conditions of our experiment – aqueous electrolyte water against a smooth hydrophilic solid, shear rates up to $\sim 10^3$ s^{-1}.

At the mercury/electrolyte interface, the classical expectation is that a partial-slip condition should hold because these two liquids have comparable viscosities. Our model neglects fluid circulation within the mercury drop and assumes that the radial component of the velocity of water at the mercury/electrolyte interface is zero. With these assumptions we are able to

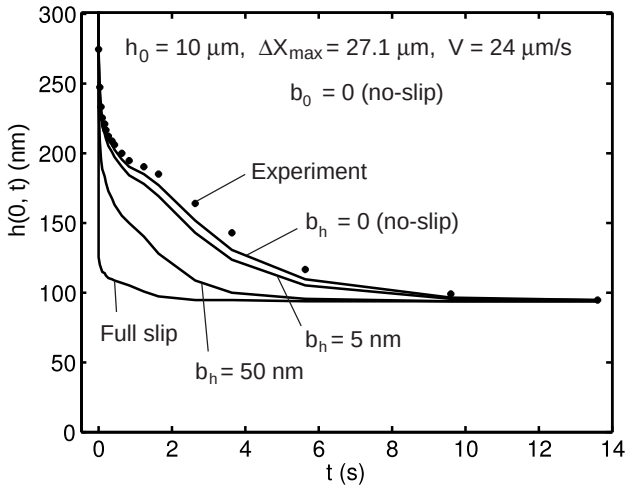

Figure 5.16: Film thickness at the centre $h(0,t)$, where dots represent the experimental values and lines are solutions based on Eq. 2.136 for $b_h = 0$ (no-slip), $b_h = 5$ nm, $b_h = 50$ nm and $b_h = \infty$ (full slip) at the mercury/electrolyte interface and $b_0 = 0$ at the mica/mercury interface. The initial separation h_0, mica travel ΔX_{max} and mica velocity V are indicated in the figure.

obtain a good fit to experimental data. By adjusting other physical parameters to the extremes allowed by experimental uncertainty, it is possible to accommodate a slip length of no larger than 2 nm at each interface while still being able to maintain a reasonable fit between theory and experiment. The use of a full slip boundary condition at either interface would have yielded film drainage times ten times shorter than those observed experimentally (see Figure 5.16). In our view, there is no compelling need to invoke the slip length as an additional parameter to fit experiments and our results support the conclusion of zero or negligible slip at the interfaces.

The fact that our data is consistent with a no-slip boundary condition at the mercury/electrolyte interface requires further discussion. A no-slip boundary condition is known to occur at fluid/fluid interfaces if sufficient surfactant (less than a monolayer) is adsorbed to immobilize the interface. In the experiments reported in [25] strenuous efforts were made to minimise contamination in both the mercury and aqueous phases and to work with

a freshly-prepared mercury/electrolyte interface no more than ∼10 minutes old, but it is never possible to guarantee that the level of surface-active material was zero. Hence it is impossible to state unequivocally that the absence of slip that seems to fit our experimental data was not caused by immobilization of the interface by trace contaminants. However, other experimental data – measurements of surface forces [24] and of mercury/electrolyte interfacial tension – gave no indication that the interface was contaminated.

There is also the possibility that in the presence of adsorbed surface-active species, compression or redistribution of such species along the interface can occur as a result of hydrodynamic flow in the adjacent fluids, giving rise to the Marangoni effect [67, 21]. Such coupling between fluid flow and adsorbate distribution in the interface acts to retard the flow, which is the direction required to improve agreement between theory and experiment within the dimple region. However, it can only be effective if the amount of surfactant at the interface is less than the amount required to immobilize the interface – no Marangoni effect can occur if there are no-slip boundary conditions. Hence inclusion of Marangoni coupling would require use of a partial-slip boundary condition as a starting point, which as we have discussed above is not consistent with our data.

Apart from the question of hydrodynamic boundary conditions discussed above, there is another factor that could possibly account for the minor discrepancy between theory and experiment near $r = 0$. The discrepancy would be removed if a small additional pressure (∼20 Pa, or ∼5% of the Laplace pressure in the drop) were acting in a region of radius 50 μm around $r = 0$, and a possible source is osmotic pressure due to a locally high concentration of solute. An additional concentration of 8 μM in this central region is all that would be required to produce 20 Pa of pressure. In this regard, there is one experimental detail that has not been considered thus far in the discussion. While mercury is generally regarded as a perfectly polarizable electrode, we in fact observe a small leakage current of about 0.3 μA throughout the experiment. The current may be associated with an electrode process that produces new molecular or ionic species, such as reduction of oxygen that remains dissolved at trace levels in the aqueous phase despite our best efforts

to remove it. The portion of leakage current in the interaction zone (of lateral radius say ∼100 μm and thickness ∼100 nm) would be sufficient to generate a significant concentration of new solute (as much as 1 mM each second) in the small volume of the aqueous film. If the new solute is slow to diffuse out of this constricted region, a local increase in osmotic pressure could easily be accounted for. While a detailed consideration of this effect will require additional experimentation and consideration of solute transport parallel to the trapped electrolyte film, we can see that the difference between theory and experiment in the interfacial profile around $r = 0$ could be caused by small local variations in solute concentration.

Interestingly, both experiment and theory show that the mercury continues to approach the mica after the latter has stopped moving. In particular, not only does $h(0, t)$ continue to decrease as the dimple relaxes, but $h(r_{rim}, t)$ also decreases. This cannot be an effect of inertia of any of the media involved, since inertia is not included in the model. Instead, it is associated with the experimental design which has a transition from constant velocity while the mica is being driven, to quasi-constant force after the drive stops. The drop shape continues to evolve from its instantaneous shape at t_{stop} to its equilibrium shape under the influence of disjoining pressure and hydrodynamic effects. This includes a change in the far-field deformation, which drives a continuing evolution of the barrier rim. As seen from Figure 5.12, the film thickness $h(r_{rim}, t)$ at the barrier rim actually decreases faster after the drive stops. In the absence of disjoining pressure or in the presence of an attractive disjoining pressure, this can push some of the aqueous phase back towards the centre of the dimple and causes the 'bounce' in $h(0, t)$ that is seen in Figures 5.8 and 5.12.

A particular feature of our experimental modeling is the success in predicting the time at which the aqueous film collapses when the disjoining pressure is weak or attractive. Experimentally the collapse is observed to occur very quickly, but we are unable to say whether it involves processes that are not axisymmetric and/or multiple local collapses and/or engulfment of the aqueous film phase inside the mercury drop. However, the model does predict the moment of collapse accurately, which strongly suggests that the

physical phenomena causing the collapse are included in the model. Remembering that the model is strictly axisymmetric, this means that the collapse is predicted without any reference to capillary waves or local instabilities of the film. Instead, the implication is that the collapse is determined by a mechanical instability in which the gradient of disjoining pressure overcomes the ability of the drop to resist, through its interfacial tension, a sudden elongation.

Chapter 6

Perturbations on a wetting film: the wimple, pull-off and jump in experiments in SFA

6.1 Introduction

This chapter reports experimental observations and modelling of transient responses of thin equilibrium aqueous films that arise from mechanical and electrical perturbations. We present three different experiments with similar configurations in which thin films with initial thickness less than 100 nm are stabilised by electrical double layer repulsion between a molecularly smooth solid mica surface and a deformable mercury/electrolyte interface in the SFA. The surface potential of the mercury is maintained by an externally applied potential between the mercury and a calomel electrode in the bulk electrolyte. Mechanical perturbations to the film are generated by:

(a) pushing the mica surface towards the mercury/electrolyte interface for a fixed distance over a preset time interval,

(b) pulling the mica surface away from the mercury/electrolyte interface.

Electrical perturbations are applied by:

(c) making a step change in the applied voltage on the mercury which results in a rapid change in the electrical double layer interaction between

the mica and the mercury. This can include switching from a stable film configuration to an unstable one.

By observing the response to mechanical perturbations, we gain insight about the deformation mechanism on the nanometre scale that thin films can undertake in order to make the transition from one equilibrium state to another under the constraints of surface forces, interfacial tension and hydrodynamic interactions. The electrical perturbation studies yield information on the modes of collapse of stable nanometre-thick aqueous films when the stabilizing effects of surface forces are suddenly removed.

We also make quantitative comparisons between the observed time dependent deformations of the mercury/electrolyte interface as the aqueous film accommodates such perturbations using a theoretical model that takes into account surface forces, hydrodynamic flow in the thin film and deformations of the mercury/electrolyte interface. This comparison allows us to elucidate the respective contributions of surface forces and hydrodynamic pressure variations in determining interfacial deformations during the course of the transient response of the film. We can also use the theory to model situations which have not yet been accessed experimentally, to provide insight into the phenomena occurring.

In section 6.2, we present comparisons between the model and experimental results of deformations of the mercury/electrolyte interface starting from an equilibrium thin film as the mica plate is pushed towards the mercury. A detailed analysis of the physical basis of the observed "wimple" is provided. In section 6.3, we present results and analysis for the response of the film when the mica is pulled away from an equilibrium position. This study uncovers a novel mechanism for de-stabilising thin films by a pull-off perturbation. In section 6.4, we analyse the collapse of a stable equilibrium film that follows a step change in the applied potential on the mercury that removes the stabilising repulsive electrical double layer barrier. These novel observations suggest that there are different modes of coalescence depending on the initial shape of film but capillary wave induced instabilities appear not to be the collapse mechanism under the conditions of our experiments. The chapter closes with a discussion.

6.2 Compression of a stable film: the Wimple

The experimental details for compressing an equilibrium film and observing the details of resulting transition to another equilibrium state have been reported earlier [23]. Starting with a stable aqueous film of comparatively small radius (~ 20 μm) stabilized by electrical double layer repulsion between the mica and the flattened mercury/electrolyte interface, the mica is driven towards the mercury drop for a distance of 10 μm in a time of less than 1 s. In response, the mercury/electrolyte interface deforms, develops a characteristic shape dubbed a "wimple" [23] and then subsequently evolves into the more familiar "dimple" shape of trapped fluid which finally drains to form a new equilibrium film of larger radial dimension but with the same thickness as the initial film. The same initial and final equilibrium film thickness is determined by the separation at which the disjoining pressure balances the internal Laplace pressure of the mercury drop. Since deformations of the mercury drop remain small on the scale of the drop, the Laplace pressure is essentially constant.

The measured time sequence of the evolution of the mercury/electrolyte (1 mM KCl) interface described above is shown in three stages in Figure 6.1. The response of the film during the interval when the mica is being pushed is shown in Figure 6.1a. The initial state ($t = 0$) is a 50 nm thick equilibrium aqueous film between the mica plate and the flattened mercury/electrolyte interface. When the mica is driven rapidly 10 μm towards the mercury, the central thickness $h(0, t)$ of the film increases in thickness – that is, the central portion of the mercury/electrolyte interface backs away from the approaching mica surface while the thickness of the outer part of the film, beyond about $r \sim 50$ μm, decreases. Shortly after the mica stops, at a time of 0.8 s, a second minimum in the film thickness develops at a large radial position at $r \sim 100$ μm, in addition to the existing minimum at the axis of symmetry at $r = 0$, see Figure 6.1b. These two minima give the characteristic wimple shape. After the formation of the wimple, the central thickness $h(0, t)$ continues to increase while the thickness at the new film minimum at $r \sim 100$ μm decreases until the interfacial shape changes into a dimple profile with a barrier rim at

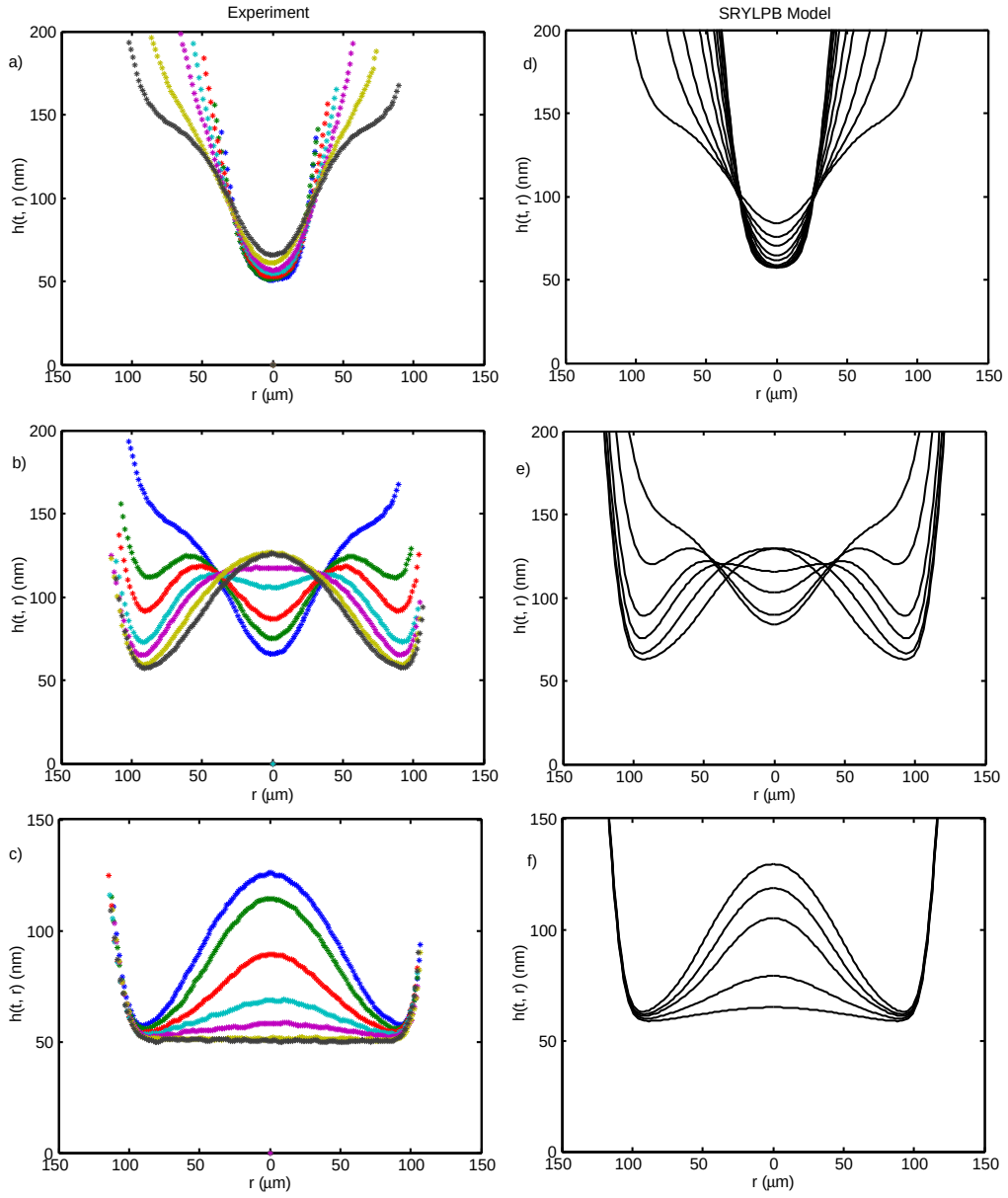

Figure 6.1: The response of an initially stable aqueous film between the mica plate and the flattened mercury/electrolyte interface when the mica is driven towards the mercury drop. Experimental results are taken from ref [23] at times a) 0, 0.04, 0.08, 0.12, 0.2, and 0.28 s. b) 0.28, 0.44, 0.6, 0.92, 1.24, 1.88, and 2.52 s. c) 2.52, 3.8, 6, 8, 10, 14, and 18 s. Theoretical results from the model are plotted at times d) 0, 0.04, 0.08, 0.12, 0.2, 0.28, 0.44, 0.6, and 0.92 s. e) 0.92, 1.24, 1.88, 2.52, 3.8 and 6 s. f) 6, 8, 10, 14, and 18 s.

$r \sim 100$ μm at around 2-3 s. The final stage of the film evolution is given in Figure 6.1c for $t > 2$ s, in which the dimple drains to an equilibrium film of the same thickness as the initial film. However, the final film radius is now several times larger at $r_{final}^{film} \sim 100$ μm compared to an initial film radius of ~ 20 μm . Throughout the entire process, which takes about 18 s in total, the film maintains axial symmetry.

The corresponding stages of deformations of the mercury/electrolyte interface as predicted by the model are shown in Figure 6.1(d-f). The experimental and theoretical parameters used to produce the results in Figure 6.1 are summarised in Table 6.1. Using parameter values within experimental uncertainties, the model gives semi-quantitative agreement with experiment. The degree of agreement is not as precise as that found for earlier related SFA experiments on dimple formation when the mica surface is driven towards the mercury drop from a large separation [52]. One reason for this is associated with the drive time being short ($\sim$0.5 s) and comparable to the start-up and slow-down times of the motor used to drive the mica surface. As a consequence, the exact drive function of the mica, which is an input to the theoretical model, is not well characterised for the wimple experiment. Nonetheless, the main features of the experiment, namely, the initial increase of the central separation $h(0,t)$, the development of the separation minima at a large radial position, the formation of the characteristic wimple, the evolution from a wimple to a dimple and the final drainage to the new equilibrium film with the same thickness of the original film, but with a larger flattened radius, are all predicted by the model.

During the development of the wimple and subsequently the dimple shown in Figures 6.1a and 6.1b, the relative contributions to the total constant force from electrical double layer and hydrodynamic interaction change over time. An examination of this change provides insight into the physical processes that lead to the development of the wimple and subsequently the dimple during film drainage. The theoretical predictions for the disjoining pressure and the hydrodynamic pressure are given in Figure 6.2. For easy reference the curves are labelled (A) to (E) as time progresses.

At early times as the mica approaches the mercury, the film thickness at

Physical parameters	Experimental	Theoretical
Wimple		
Mica surface potential (mV) [59]	-90 ± 10	-90
Drop surface potential (mV)	-500 ± 20	-500
Electrolyte concentration (mM KCl)	1 ± 0.01	1
Drop radius, R_0 (mm)	3.04 ± 0.1	3.04
Maximum mica travel, ΔX_{max} (μm)	10 ± 3	7.2
Drive velocity, V (μm/s)	fast	8
Pull-off		
Mica surface potential (mV)	-100 ± 10	-90
Drop surface potential (mV)	-492 ± 20	-492
Electrolyte concentration (mM KCl)	0.1 ± 0.01	0.11
Drop radius, R_0 (mm)	1.9 ± 0.1	1.9
Drive velocity, V (μm/s)	23 ± 1	24
Jump		
Mica surface potential (mV)	-90 ± 10	-90
Initial drop potential (mV)	-47, -16 ± 20	-51, -17
Final drop potential (mV)	-42, -11 ± 20	-47, -11
Electrolyte concentration (mM KCl)	0.1, 1 ± 0.01	0.11, 1.
Drop radius (mm)	0.67, 0.9 ± 0.1	0.67, 0.74

Table 6.1: Nominal experimental parameters of the mica-mercury system and corresponding theoretical values used in the calculation.

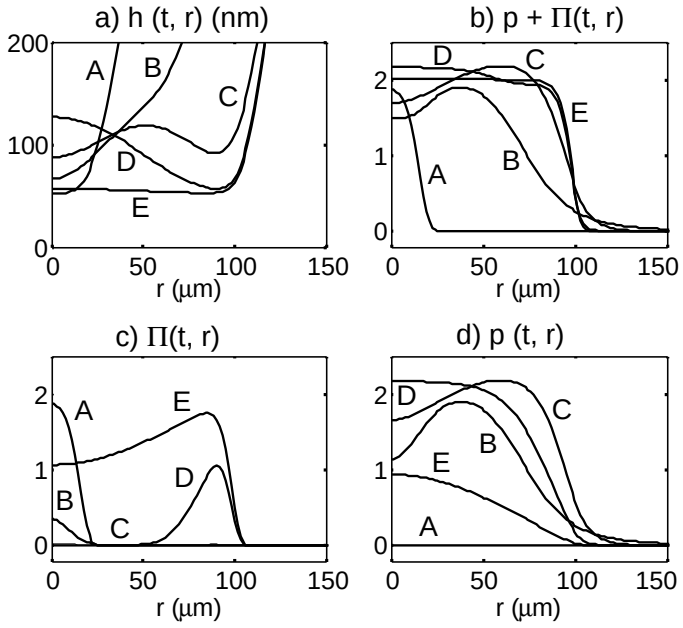

Figure 6.2: Theoretical values of the film thickness $h(r,t)$ in nm and the hydrodynamic $p(r,t)$ and disjoining pressure $\Pi(r,t)$ (in units of σ/R_0) at various times corresponding to the wimple experiment in Figure 6.1. A – 0. s, B – 0.92 s, C – 1.88 s, D – 6 s, E – 18 s.

$r \sim 0$ increases slightly (Figure 6.2a, curves A and B) as the mercury drop backs away from the approaching mica. The increase in central film thickness causes the disjoining pressure to fall (Figure 6.2c, curves A and B) and the hydrodynamic pressure is small in magnitude and is slightly negative around $r \sim 0$ (Figure 6.2d, curve A). However, the thinning of the film around $r \sim 30$ – 50 μm (Figure 6.2a, curve B) causes the hydrodynamic pressure to increase locally (Figure 6.2d, curve B) which drives fluid towards $r = 0$, causing the central portion of the film to continue thickening. At the formation of the wimple (Figure 6.2a, curve C) all parts of the mercury/electrolyte interface are more than 80 nm from the mica and so the disjoining pressure is negligible through out the film (Figure 6.2c, curve C) while the hydrodynamic pressure dominates (Figure 6.2d, curve C). From this time onwards, the rate of thinning of the draining film is controlled by hydrodynamic considerations.

When the film thickness at the barrier rim in the film profile at $r \sim 100$ μm reaches a thickness of ~ 50 nm (Figure 6.2a, curve D), the repulsive disjoining pressure prevents further film thinning beyond this point. Now the inverted curvature of the dimple causes the fluid trapped within the dimple at $r \leq 100$ μm to slowly drain out of the barrier rim to form the final uniform film (Figure 6.2d, curve E). As the film thins everywhere in $r \leq 100$ μm, the disjoining pressure in this region increases (Figure 6.2c, curve E) while the hydrodynamic pressure decreases as the film approaches equilibrium (Figure 6.2d, curve E). From this analysis, the combined roles of disjoining and hydrodynamic pressures in creating the complex wimple-dimple shape are evident. An earlier attempt to account for the wimple shape did not consider hydrodynamic effects [68], and from the above discussion such an explanation would appear to be incomplete.

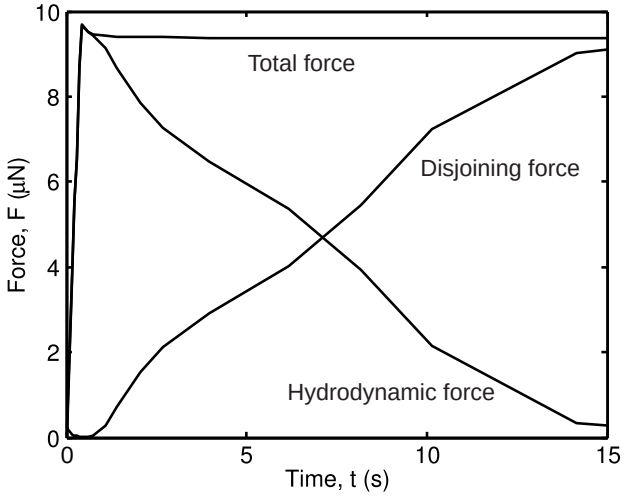

Figure 6.3: Theoretical calculations of the contributions from hydrodynamic interactions and disjoining pressures to the total force during the wimple experiment in Figure 6.1.

The time variation of the force between the mica and the mercury as predicted by the model is given in Figure 6.3. To a first approximation the force is the internal pressure of the drop (which remains essentially constant because the extent of deformation is small compared to the undeformed drop

radius) multiplied by the flattened surface area, so a fivefold increase in contact radius corresponds to a 25-fold increase in the total force. This increase takes place rapidly during the short time interval (<1 s) during which the mica surface is being pushed. The subsequent development of the wimple and then the resolution to the dimple takes place essentially under a constant total force regime, but the relative contributions from the disjoining pressure and from hydrodynamic interactions to this constant force change over time as indicated in the discussion of results of Figure 6.2.

6.3 Pull-off response of a stable film

The pull-off experiment starts from an equilibrium aqueous film with a radius of about 100 μm and 93 nm thick that is trapped between the mica plate and the flattened mercury/electrolyte (0.1 mM KCl) interface. The film is stabilized by electrical double layer repulsion between the mica and the mercury interface. The mica is then retracted from the mercury drop at a speed of 24 μm/s. The subsequent response of the film profile is shown in Figure 6.4 together with predictions from the model. The agreement between theory and experiment is very good. As the mica retracts, the film maintains axial symmetry. Although the mica is being retracted from the mercury surface, an annular region of the aqueous film actually becomes thinner during the transient stage prior to the expected final jump apart of the mica surface from the mercury/electrolyte interface. In the initial stages, a minimum in the film thickness develops near the rim of the initial film at $r \sim 100$ μm while the central area of the film maintains a constant thickness. Over time the radial position of this minimum moves towards the center of the film as the film thickness at this minimum continues to decrease. When the radial position of this minimum approaches $r = 0$, the film has thinned from 93 nm to about 70 nm. After that the mica surface jumps apart rapidly from the mercury/electrolyte interface.

The pressure profiles shown in Figure 6.5 provide the underlying details of the contributions to the total force from hydrodynamics and from disjoining pressures. If we first consider the hydrodynamic pressure we see it

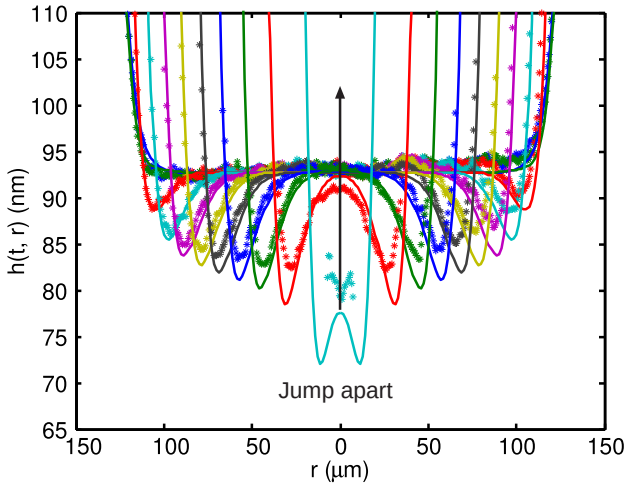

Figure 6.4: Comparison between theory and experiment for a mercury drop being pulled away from a mica surface in SFA. The double layer interaction is strongly repulsive (see Table 1) and film profiles are shown at times t =0., 0.08, 0.16, 0.24, 0.32, 0.4, 0.48, 0.56, 0.64, 0.72 and 0.76 s before the mica jumps apart from the mercury interface.

is negative at all radial positions which reflects the hydrodynamic suction that might be expected when two surfaces are pulled apart. However, the most strongly negative pressure is confined to an annular region near the edge of the quasi-flat part of the drop. Because the mercury drop is easily deformable, the negative pressure pulls part of it closer to the mica. The reduced film thickness in this region creates a higher disjoining pressure which counteracts the effect; nevertheless thinning of the film occurs in an annular region that shrinks with time until it approaches $r \sim 0$.

Variations of the hydrodynamic and disjoining components of the force between the mica and the mercury/electrolyte interface during the pull-off event are shown in Figure 6.6. The contribution from hydrodynamic effects is negative for most of the time as is expected from the knowledge that lubrication forces (or hydrodynamic suction) opposes the separation of two closely spaced surfaces. The deformable drop responds by first thinning at the film periphery, but this generates a local repulsive contribution to the

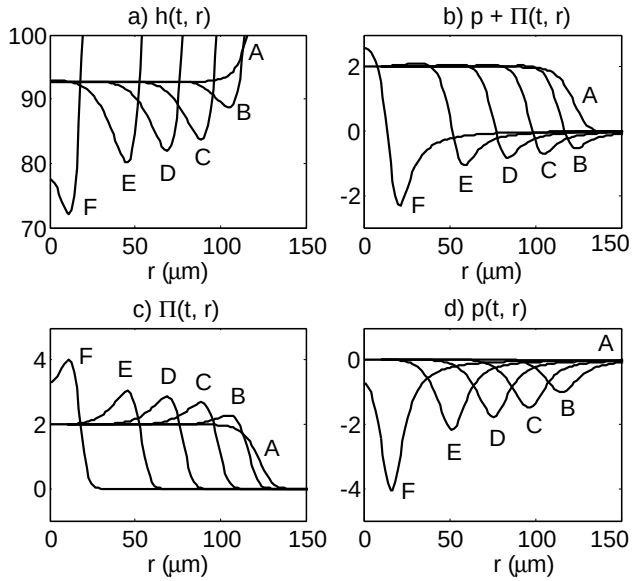

Figure 6.5: Theoretical values of the film thickness $h(r,t)$ in nm and the hydrodynamic $p(r,t)$ and disjoining pressure $\Pi(r,t)$ (in units of σ/R_0) at various times corresponding to the pull-off experiment in Figure 6.4. A – 0. s, B – 0.16 s, C – 0.32 s, D – 0.48 s, E – 0.64 s, F– 0.76 s.

total force from the local increase in disjoining pressure. However, since the lateral extent of the film is decreasing, the total force decreases towards zero as the mica and the mercury separate.

A notable observation of the results in Figure 6.4 is that while the radial extent of the film shrinks as the mica retracts, the edge of the film actually becomes thinner during this transient period. This offers the possibility that the deforming interface may be able to reach an available attractive region of the disjoining pressure curve so that the resultant attraction is sufficient to de-stabilise the film and cause it to collapse. A demonstration of the possibility of such a pull-off induced film collapse is give in Figure 6.7. However, for the mica-mercury system, this can occur only over a small system parameter space.

There is experimental evidence to support the possibility a pull-off induced film collapse. In a study of the coalescence of two oil drops driven

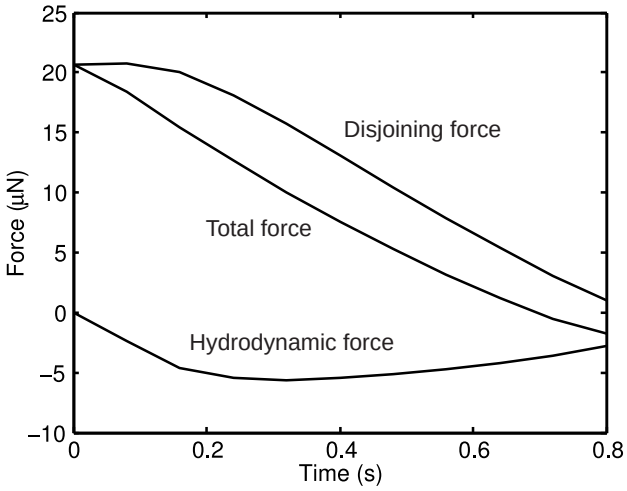

Figure 6.6: Theoretical calculations of the contributions from hydrodynamic interactions and disjoining pressures to the total force during the pull-off experiment in Figure 6.4.

together slightly off centre in a four roll mill configuration, drop coalescence can sometimes be enhanced as they enter the elongation quadrant of the flow field where the drops are beginning to be pulled apart by the imposed flow field [73, 78].

6.4 Changing the bias voltage – film collapse

Another way to perturb an equilibrium film in the mica-mercury system is to apply a step change to the bias voltage between the mercury and the bulk electrolyte which alters the disjoining pressure in the aqueous film between the mica and the mercury due to electrical double layer interactions. This change can be considered as instantaneous since the electrical double layer can re-equilibrate on a millisecond time scale while the response time of the deformable mercury/electrolyte interface is on the order of seconds.

The change in bias voltage was designed to lower the repulsive maximum in the disjoining pressure due to electrical double layer interactions to below that of the Laplace pressure of the drop (see Figure 6.8). With this process,

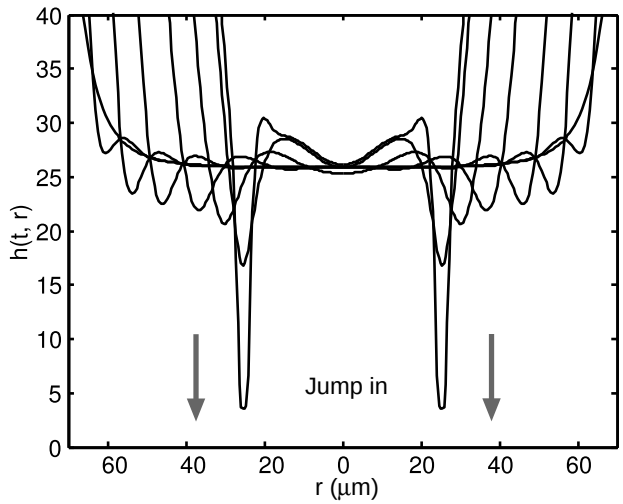

Figure 6.7: A demonstration of the possibility of a pull-off induced collapse of an initially stable film. The system parameters are similar to the ones in Figure 6.4 but with a concentration of 0.5 mM KCl, mica potential of -70 mV and mercury potential of -15 mV. Times are: 0, 0.06, 0.14 ,0.3, 0.7, 1.2, 1.65, and 1.71 s.

we are able to observe directly the collapse mechanism of a destabilized equilibrium film with sub-nanometre resolution. We consider two different initial equilibrium configurations in which the mercury/electrolyte interface has been flattened to different degrees against the mica plate:

(a) a highly flattened film with initial separation about 30 nm and a large film radius of 30 μm in 0.1 mM KCl

(b) a slightly flattened film with a distance of closest approach of about 21 nm and a small film radius of around 15 μm in 1.0 mM KCl

Experimental results and predictions by the model for these two cases are given in Figure 6.9. As the vertical scale only spans a distance of about 10 nm, the scatter in experimental data points appears greater in this figure. The thinning of the highly flattened film, Case (a) with a ratio of film radius to film thickness of about 1000 in the present case, is initiated by the development of a thinning annulus at the edge of the film which gives the collapsing film a "horned" shape (Figure 6.9a) and is reminiscent of the pull-off phenomenon (Figure 6.4). The central portion of the flat film remains

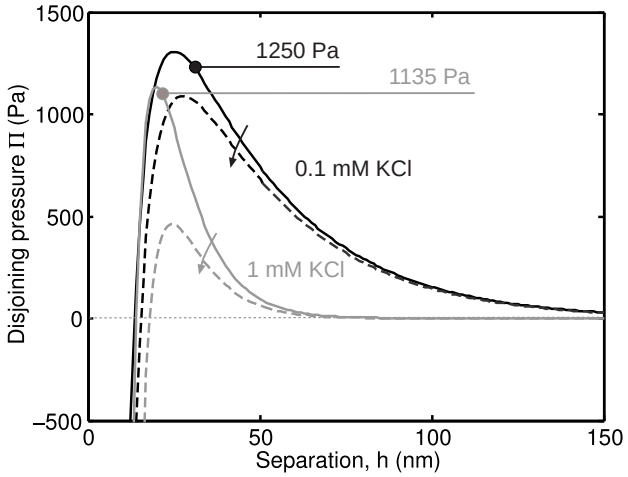

Figure 6.8: The change in disjoining pressure according to the nonlinear Poisson-Boltzmann theory as a result of the change in the bias potential on the mercury. At 0.1 mM KCl, the surface potential of the mercury was changed from –51 mV to –47 mV and the maximum of the initial pressure curve is at 25 nm. At 1.0 mM, the surface potential was changed from –17 mV to –11 mV with the initial pressure maximum at 15 nm. The corresponding Laplace pressures of the mercury drop are indicated by the horizontal lines. The mica surface potential was –90 mV at both electrolyte concentrations.

effectively stationary even until jump-in occurs at the edge of the film because hydrodynamic resistance arising from drainage through the narrowing barrier rim as well as the repulsive disjoining pressure both act to suppress motion of the central portion of the flattened film. For the slightly flattened film with an initial film radius of only 15 μm, Case (b), the thinning film has a more complicated profile during the collapse process that is also predicted in the theoretical model. Unfortunately, our current apparatus is unable to resolve the magnitude of the oscillations in the film thickness near $r = 0$ with higher precision.

In Figure 6.10, we see that during the course of film collapse, the total pressure profile is quite constant in the radial direction and this is maintained by a balance between variations in the disjoining pressure and the hydrodynamic pressure profiles.

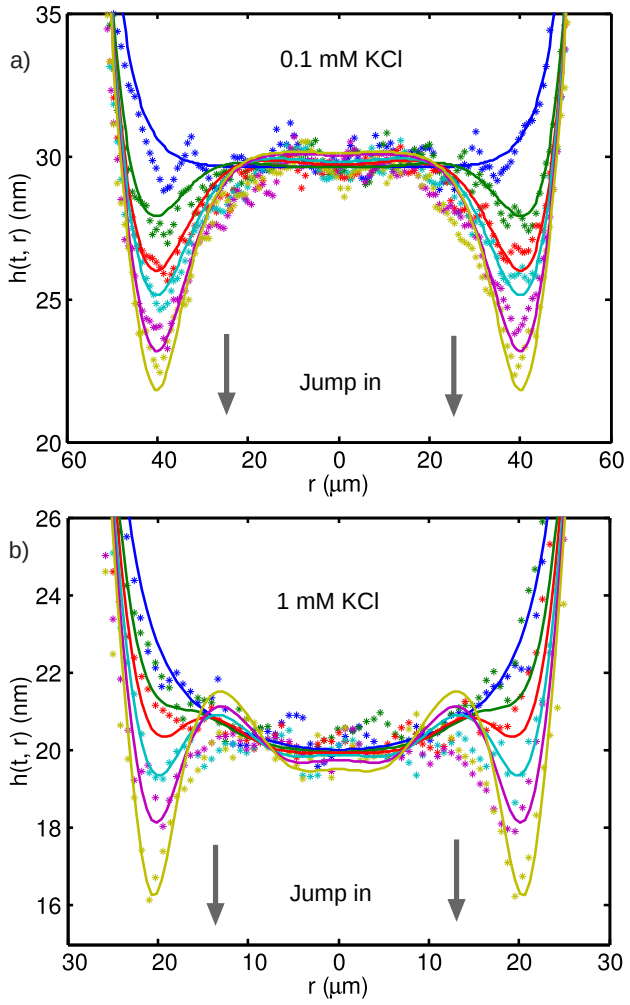

Figure 6.9: The collapsing profiles of initially stable aqueous films between a mica and a mercury surface destabilized by a change in the disjoining pressure that arise from a step change in the bias voltage of the mercury. Experimental results (symbols) and theory (lines) are shown corresponding to the two cases shown in Figure 6.8 for various elapse times after the bias voltage change: a) 0.1 mM KCl for t = 0., 0.8, 1.2, 1.6, 2., 2.4 ,2.8, and 3.2 s; b) 1 mM KCl for t = 0, 0.04, 0.08, 0.12, 0.16, and 0.2 s. Other experimental and theoretical parameters are given in Table 6.1. After the final time step, the mercury/electrolyte interface jumps into contact with the mica.

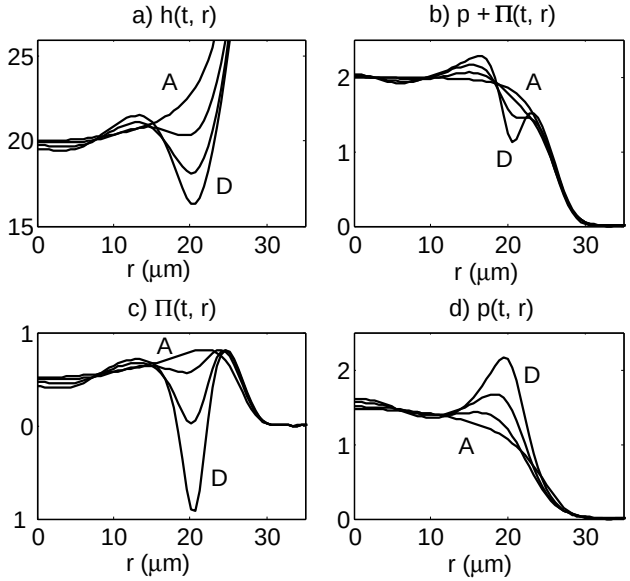

Figure 6.10: Theoretical values of the film thickness $h(r,t)$ in nm and the hydrodynamic $p(r,t)$ and disjoining pressure $\Pi(r,t)$ (in units of σ/R_0) at various times corresponding to the film collapse phenomenon in Figure 6.9b at 1 mM KCl: for $t =$ (A) 0, 0.08, 0.16, and (D) 0.2 s.

In Figure 6.11, we see that both films drain under constant force conditions provided by the Laplace pressure of the drop with the difference being the magnitude of the relative contributions from electrical double layer force and hydrodynamic interactions. The magnitude of the total force in each case depends approximately on the square of the initial flattened film radius.

6.5 Modes of film collapse

Given the good quantitative agreement between experimental profiles and predictions of the model, we can use this model to investigate other possible modes of the film collapse. In Figure 6.12a, we show the collapse of a stable mercury/electrolyte interface with an initial separation of 23 nm and Laplace pressure of 1135 Pa in 1 mM KCl but whose interface is hardly flattened (see Figure 6.8). In this case, because of the high curvature of the initial interface,

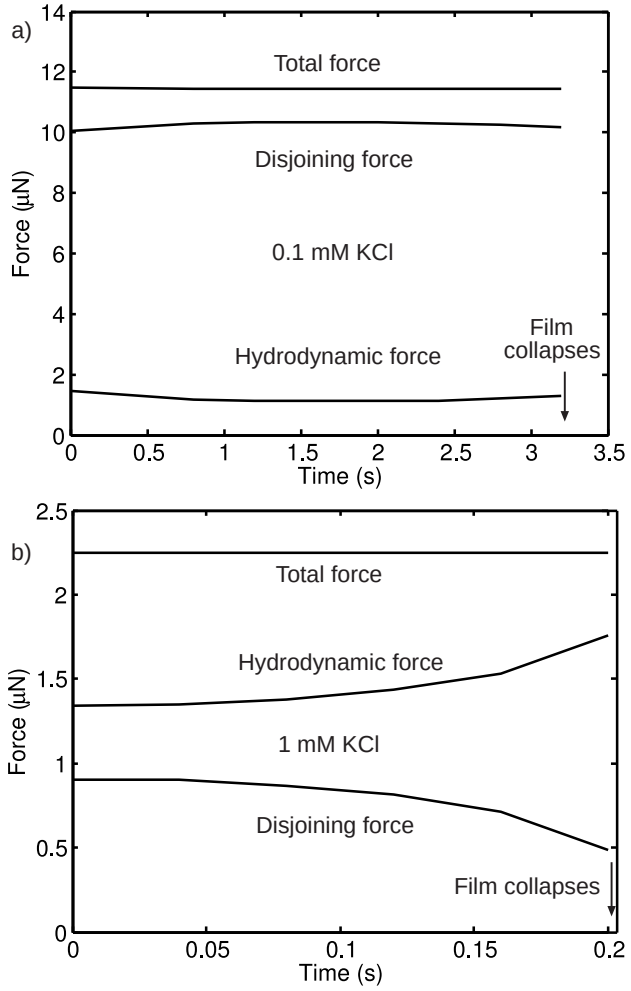

Figure 6.11: Theoretical predictions of the hydrodynamic and disjoining pressure components of the total force corresponding to the film collapse phenomenon in Figure 6.9 for a) 0.1 mM and b) 1 mM.

the induced electrical double layer attraction is able to pull the centre of the film to form a pimple, and film collapse occurs at the central region of the film. The appearance of a small dimple at the very last stage of collapse may not be of practical significance since the film is possibly too thin for a continuum description to be valid and the film actually collapses before the next time step. The corresponding force components from electrical double layer and hydrodynamic interactions are given in Figure 6.12b.

In order to understand how the various modes of film collapse occur via the formation of a wimple, dimple or pimple, we use the model to study how three different equilibrium films collapse under only the combined effects of Laplace pressure and hydrodynamic effects after the disjoining pressure that stabilizes these films is suddenly removed. The three initial equilibrium films of increasing degrees of flattening are formed by advancing the mica surface towards the mercury/electrolyte interface to 0.4 μm, 2.4 μm and 4.4 μm beyond the position at which the mica would have made contact with the mercury had the latter not deformed. The results in Figure 6.13 demonstrate that when the stabilizing disjoining pressure is then removed, the film collapses under the action of the now unbalanced Laplace pressure. Whether the film profile forms a dimple, a wimple or a horned profile is controlled by the ratio of the flattened region of the film to the size of the wings. For a film with negligible flattening (Figure 6.13a), the hydrodynamic wing reaches the centre of the drop and gives the profile a dimple appearance. As the degree of initial film flattening increases (Figure 6.13b, c) the hydrodynamic wings will increasingly be confined to the edge of the thinning film. In all cases, the thickness of the barrier rim at the hydrodynamic wings decreases as time progresses and film coalescence takes place at the barrier rim. The development of hydrodynamic wings at the edge of the film is also consistent with the observed wimple response of the equilibrium film to a mechanical perturbation when the mica plate is pushed further towards the mercury.

The development of hydrodynamic wings at the edge of the film is also consistent with the observed wimple response of the equilibrium film to a mechanical perturbation when the mica plate is pushed further towards the mercury.

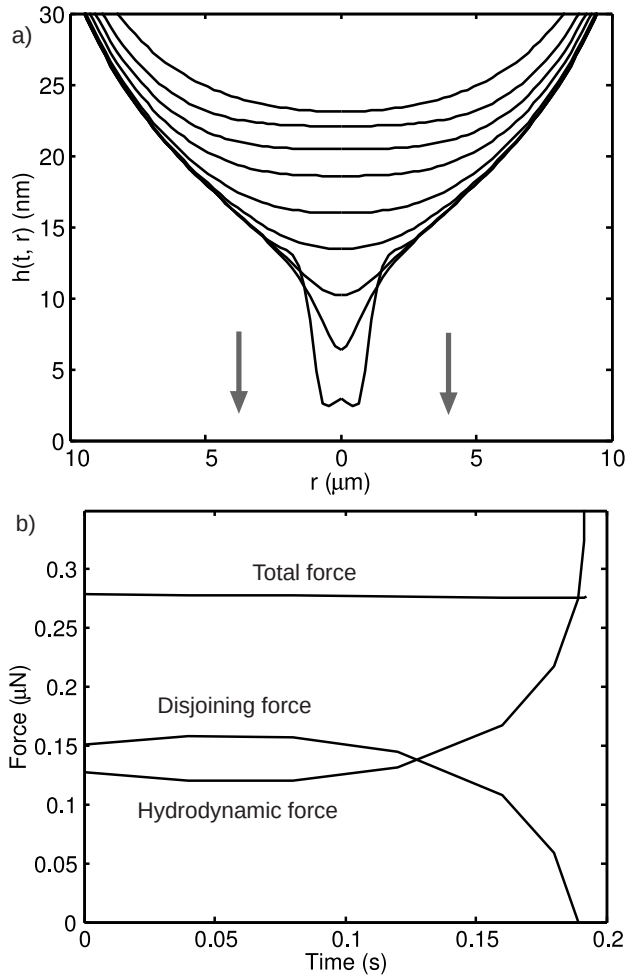

Figure 6.12: Theoretical predictions of the collapse, triggered by a step change in bias potential, of a stable mercury/electrolyte interface that is barely flattened. The initial distance of closest approach is 23 nm in 1.0 mM KCl. The resultant change in disjoining pressure is shown in Figure 6.8. a) The collapsing film profile that proceeds via the development of a 'pimple' at the center of the film; b) Time variations of contributions from hydrodynamic and disjoining pressures to the total force during the collapse.

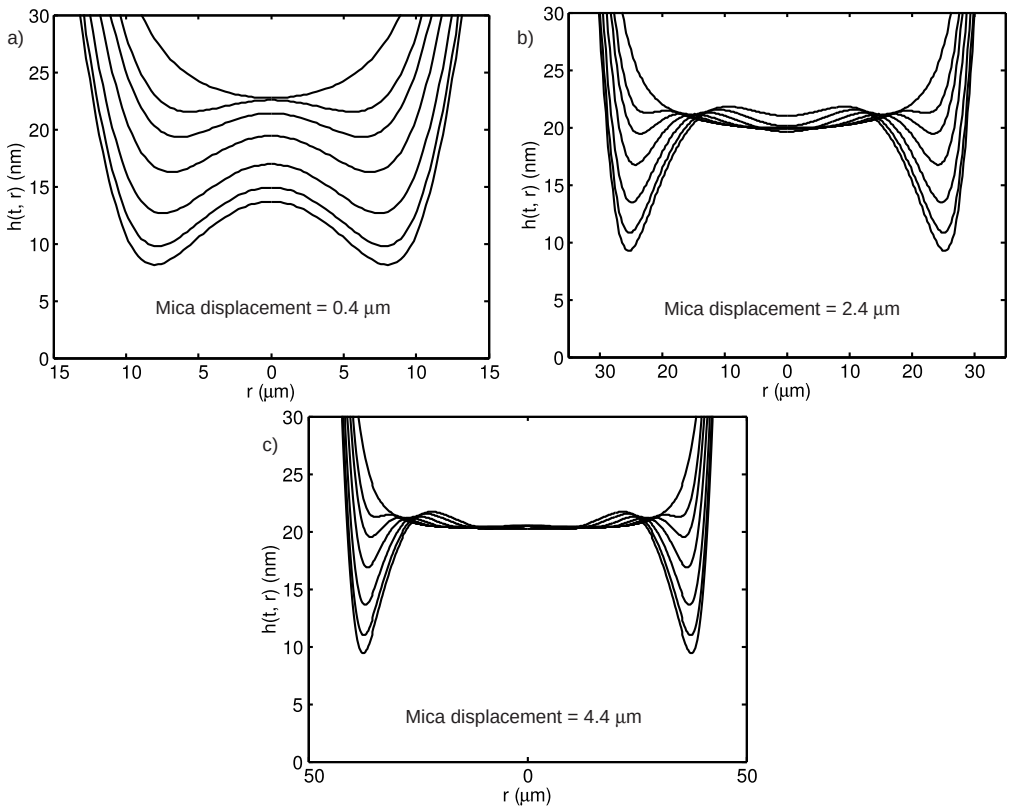

Figure 6.13: Predicted modes of collapse of stable aqueous films of different initial thicknesses between a mica plate and a deformable mercury/electrolyte interface once the stabilizing disjoining pressure is removed and the film thins under the action of capillary pressure and hydrodynamic interactions. The initial stable films are formed by advancing the mica surface to a) 0.4 μm, b) 2.4 μm and c) 4.4 μm beyond the position where it would have made contact with the undeformed mercury drop. Other system parameters corresponds to the 1.0 mM case in Table 6.1. The profiles are at elapse times of t = 0, 0.05, 0.1, 0.2, 0.4, 0.7 and 1.0 s after the removal of the stabilizing electrical double layer disjoining pressure (see Figure 6.8).

Experimental results are in very good quantitative agreement with the developed model in which hydrodynamic interactions are described by Stokes flow in the Reynolds thin film treatment, interfacial deformations are accounted for by the Young-Laplace equation and electrical double layer interactions between the solid mica surface and the deformable mercury/electrolyte interface are described by the non-linear Poisson-Boltzmann theory for dissimilar surfaces; van der Waals interactions are negligible for the range of film thicknesses in question. The parameters used in theoretical calculations are all within measurement tolerances of these quantities.

We found that the no-slip hydrodynamic boundary condition at the mercury/electrolyte interface provided the best agreement between theory and experiment for all experimental situations. This is unexpected since the viscosity of mercury is only about 60% higher than that of water at room temperatures and particular care was take to keep the mercury/electrolyte interface free from contaminants during the course of all experiments. However, a possible explanation can be found for the apparent applicability of the no-slip boundary condition in a recent study of the primary electroviscous effects of mercury drops [58]. It was found that specific viscosity of suspensions of mercury drops that are large compared to the Debye length or are at high surface potentials, assume the same form as that for a suspension of rigid sphere. That is, in the above regime, the mercury behave like rigid particles at which the no-slip hydrodynamic boundary condition can be applied at the surface. The physical picture is that electroneutrality requires counterions to remain fixed with respect to the position of the equipotential mercury surface which has the effect of inhibiting flow of the aqueous phase parallel to the surface. If the drag due to counter-ions is large enough it will create an effective no-slip at the interface. While this observation provides a plausible reason for the use of the no-slip boundary condition to provide agreement between theory and experiment, it is a topic that remains to be explored in more detail in a forthcoming publication. Here we make the remark that even assuming a slip length of a few nanometres at the mercury/electrolyte interface will degrade the agreement between experiment and theory significantly.

In response to mechanical perturbations, the mercury drop has to advance onto or retract from the mica plate at the three phase contact zone that comprises the mercury, the aqueous electrolyte and mica with a wetting film. The observed transient behaviour such as the buckling of the initially flat mercury/electrolyte interface is reminiscent of previous studies of fluid motion in this three phase contact region. For example, it is known [19] that when a three-phase line advances over a wetting film, the film has a slightly thinner zone ahead of the three phase contact line (TPL). However, the precise connection between these earlier studies of straight TPLs and the present investigations involving the advance and retreat of a circular film stabilized by a repulsive disjoining pressure remains to be established.

When the equilibrium film is destabilised by the removal of the repulsive barrier due to electrical double layer interactions, the film collapses in an axisymmetric manner rather than by the often suggested method of collapse by capillary wave fluctuations. Given the observed role of hydrodynamics in controlling film thinning, it would appear that for large flat films, hydrodynamic pressure in the thinning film acts to suppress possible growth of capillary waves and such films collapse by coalescing at the outer rim. Our theoretical modelling, which remain axisymmetric, successfully predicts the collapse conditions. However, we do not rule out the possibility that once the film has become unstable, the coalescence at the outer rim may proceed asymmetrically.

Chapter 7

Limiting forms of small and large forces

7.1 Introduction

Limiting forms of small and large forces for interacting deformable drops have been derived and are submitted to publication in Manica et al. [53]. An important application of the theoretical model is its use to investigate how a deformable drop responds to a general applied force. In many previous AFM experiments involving a deformable drop or bubble, it has been assumed that the drop/bubble deforms as a linear Hookean spring under an applied force [34, 61, 6, 38]. This assumption underpins the key process of deducing the separation between the deformable drop/bubble and an approaching solid particle using data within the so-called constant compliance region. However, there is no general consensus that the Hookean response of a bubble or drop is correct [2, 9, 15]. While a theoretical justification of the Hookean assumption has been advanced, the comparison between theory and experiment adduced to support this is less than compelling [4]. Therefore revisiting the response of a deformable drop to an applied force in more detail will help decide the correct form of the force *vs* displacement behaviour that should be used in processing force measurement data.

7.2 Governing equations

In both the AFM and SFA experiments shown in this thesis, the film thickness, h, the radial dimension of the film, a and the unperturbed radius of curvature of the drops, R_d obey the inequalities $R_d \gg a \gg h$, and characteristic fluid velocities are in the regime where the familiar Stokes-Reynolds thin film drainage model applies. For a film with axial symmetry the governing equation for the film thickness $h(r,t)$ is

$$\frac{\partial h}{\partial t} = \frac{1}{12\mu r}\frac{\partial}{\partial r}\left(rh^3\frac{\partial p}{\partial r}\right) \tag{7.1}$$

where μ is the shear viscosity of the aqueous film and $p(r,t)$ is the hydrodynamic pressure in the film relative to the bulk pressure.

In the configuration of a mercury drop against a rigid surface with local radius of curvature R_s, the axisymmetric deformation of the drop, consistent with the thin film approximation, is governed by the modified Young-Laplace equation in the form [51, 18, 64]

$$\frac{\sigma}{r}\frac{\partial}{\partial r}\left(r\frac{\partial h}{\partial r}\right) = 2\sigma\left(\frac{1}{R}+\frac{1}{R_s}\right) - (p+\Pi) \qquad \text{one drop (SFA)} \tag{7.2a}$$

where $\Pi(h(r,t))$ is the disjoining pressure in the film due to surface forces such as electrical double layer interactions or van der Waals forces, σ is the interfacial tension of the drop and $(2\sigma/R)$ is the Laplace pressure of the drop. The SFA configuration of a rigid mica plate (Figure 2) corresponds to the limit $R_s \to \infty$. For the AFM configuration of two interacting drops (Figure 1) the modified Young-Laplace equation is

$$\frac{\sigma}{2r}\frac{\partial}{\partial r}\left(r\frac{\partial h}{\partial r}\right) = \frac{2\sigma}{R} - (p+\Pi) \qquad \text{two drops (AFM)} \tag{7.2b}$$

where $\sigma^{-1} = (\sigma_c^{-1}+\sigma_p^{-1})/2$ and $R^{-1} = (R_c^{-1}+R_p^{-1})/2$ are defined in terms of the interfacial tensions and Laplace pressures $(2\sigma_c/R_c)$ and $(2\sigma_p/R_p)$ of the two drops which may have dissimilar properties. Implicit in Eq. (7.2) is the assumption that deformations take place under quasi-equilibrium conditions under a dynamic pressure $(p+\Pi)$ [13].

The instantaneous force, $F(t)$ exerted on the drop has contributions from hydrodynamics and disjoining pressures

$$F(t) \equiv 2\pi\sigma G(t) = 2\pi \int_0^\infty [p(r,t) + \Pi(h(r,t))] r \; dr \tag{7.3}$$

This assumes that the drop radius is much larger than the range of hydrodynamic forces so that the interacting interfaces are nearly flat and parallel. The length $G(t)$ defined in Eq. (7.3) arises naturally in later discussions.

It has been shown that when a sessile drop with an equilibrium contact angle θ (see Figure 2) and unperturbed drop height z_0 is subjected to an applied force that is localised around the apex, the perturbed drop height $z^{outer}(r)$ outside the zone in which the force acts has the following small r (on the drop scale) asymptotic form as the drop deforms under constant volume [15, 13, 5]:

$$z^{outer}(r,t) \cong z_0 - \frac{r^2}{2R} + G\left[\log\left(\frac{r}{2R_d}\right) + B(\theta)\right] \tag{7.4}$$

The constant $B(\theta)$ depends whether during deformation, the three phase contact line (TPL) remains *pinned* or is free to *slip* on the substrate to maintain the unperturbed contact angle θ and is given by

$$B(\theta) = \begin{cases} 1 + \dfrac{1}{2}\log\left(\dfrac{1+\cos\theta}{1-\cos\theta}\right), & \textit{pinned} \text{ TPL} \\ 1 + \dfrac{1}{2}\log\left(\dfrac{1+\cos\theta}{1-\cos\theta}\right) - \dfrac{1}{2+\cos\theta}, & \textit{slip} \text{ TPL} \end{cases} \tag{7.5}$$

Eq. (7.4) for the drop profile, which reflects the constant volume constraint on the deforming sessile drop is an expansion correct to first order in (G/R_d). This result together with the geometric condition

$$X(t) = \begin{cases} h(r,t) + z(r,t), & \text{one drop (SFA)} \\ h(r,t) + z_p(r,t) + z_c(r,t), & \text{two drops (AFM)} \end{cases} \tag{7.6}$$

give the required boundary condition at r_{max} by a differentiation with respect to t to eliminate the constants, as shown in Chapter 2

$$\frac{dX}{dt} = \frac{\partial h}{\partial t} + \alpha\frac{dG}{dt} \quad \text{at} \quad r = r_{max} \tag{7.7}$$

where

$$\alpha = \begin{cases} \log\left(\frac{r_{max}}{2R_d}\right) + B(\theta), & \text{one drop (SFA)} \\ 2\log\left(\frac{r_{max}}{2\sqrt{R_c R_p}}\right) + B(\theta_c) + B(\theta_p), & \text{two drops (AFM)} \end{cases} \tag{7.8}$$

Eq. (7.7) is the appropriate constant drop volume boundary condition for AFM and SFA experiments in which the variation of the displacement function $X(t)$ with time t is specified.

For convenience of later discussions, we define

$$\Delta X(t) \equiv \begin{cases} X(t) - z_0, & \text{one drop (SFA)} \\ X(t) - z_{p0} - z_{c0}, & \text{two drops (AFM)} \end{cases} \tag{7.9}$$

where $\Delta X(t) = 0$ corresponds to the position where mica and the mercury drop (SFA) or where the two drops (AFM) would have come into contact had the drops not deformed.

Before we obtain numerical solutions of the governing equations and compare with experimental results we can obtain two limiting solutions that are valid for small and large forces at low velocities.

7.3 Formal results

We first derive some formal results from the governing equations. We shall consider the case of the SFA experiment of one deformable drop interacting with a flat plate and the two drops AFM situation.

Equation (7.1) can be integrated formally to give

$$p(r,t) = -12\mu \int_r^\infty \frac{ds}{sh^3(s,t)} \int_0^s x \frac{\partial h(x,t)}{\partial t} dx \tag{7.10}$$

and Eq. (7.2a) (in the flat plate limit, $R_s \to \infty$) and (7.2b) can also be integrated to give the inner solution

$$\beta h^{inner}(r,t) = \beta h(0,t) + \frac{r^2}{2R} + \frac{1}{\sigma} \int_0^r s \log(s/r)[p + \Pi] ds \tag{7.11}$$

where the constant $\beta = 1$ for the one drop against a flat plate geometry (SFA Eq. (7.2a)) and $\beta = 1/2$ for the two drop geometry (AFM Eq. (7.2b)). Now $p(r,t)$ can be eliminated from Eqs. (7.10) and (7.11) to give the formal but exact result

$$\begin{aligned}\beta h^{inner}(r,t) = \beta h(0,t) + \frac{r^2}{2R} + \frac{1}{\sigma}\int_0^r s\log(s/r)\Pi\ ds \\ - \frac{6\mu}{\sigma}\int_0^r \frac{s\log(s/r)\ ds}{h^3(s,t)}\int_0^s x\frac{\partial h(x,t)}{\partial t}\ dx \\ + \frac{3\mu}{\sigma}\int_0^r \frac{s\ ds}{h^3(s,t)}\int_0^s x\frac{\partial h(x,t)}{\partial t}\ dx \\ + \frac{3\mu}{\sigma}r^2\int_0^r \frac{ds}{sh^3(s,t)}\int_0^s x\frac{\partial h(x,t)}{\partial t}\ dx\end{aligned} \tag{7.12}$$

As $r \to \infty$, this inner solution matches the outer solution that follows from Eq. (7.4), (7.6) and (7.9)

$$h^{outer}(r,t) = \begin{cases}\Delta X(t) + \dfrac{r^2}{2R} - G\left[\log\left(\dfrac{r}{2R_d}\right) + B(\theta)\right] \\ \Delta X(t) + \dfrac{r^2}{R} - G\left[2\log\left(\dfrac{r}{2\sqrt{R_cR_p}}\right) + B(\theta_c) + B(\theta_p)\right]\end{cases} \tag{7.13}$$

where the top solution in Eq. (7.13) corresponds to one drop in SFA and the bottom to two drops in AFM. We can identify the coefficient of $\log(r)$ as

$$G(t) = -\frac{6\mu}{\sigma}\int_0^\infty \frac{s\ ds}{h^3(s,t)}\int_0^s r\frac{\partial h(r,t)}{\partial t}dr + \frac{1}{\sigma}\int_0^\infty r\Pi\ dr \tag{7.14}$$

which form Eq. (7.10), is equivalent to the definition of the force given in Eq. (7.3).

7.3.1 Small force limit

We can develop a solution valid for weak interactions that include hydrodynamic interactions and surface deformations but omitting effects due to disjoining pressure. The result is expected to be accurate for $\Delta X > 0$ before surface forces become important. We first scale variables using the capillary

number $Ca = (\mu V/\sigma)$ [47]

$$\begin{aligned} \{G, \Delta X, h\} &\sim (Ca^{1/2}R) \\ r &\sim (Ca^{1/4}R) \\ \{p, \Pi\} &\sim (\sigma/R) \\ t &\sim (Ca^{-1/2}R\mu/\sigma) \end{aligned} \tag{7.15}$$

and use a trial solution of the (non-dimensional) form

$$h(r,t) = a(t) + \beta r^2 \tag{7.16}$$

on the right hand side of Eq. (7.12) to construct the inner solution. While the trial solution assumes that the film profile has a parabolic shape, the inner solution given by Eq. (7.12) will contain the requisite logarithmic term to match with the outer solution, Eq. (7.13). To determine the unknown function $a(t)$ we substitute Eq. (7.16) into the right hand side of Eq. (7.12), take the $r \to \infty$ limiting form to match the result to the outer solution Eq. (7.13). This matching gives a first ordinary differential equation for $a(t)$

$$\frac{3}{a(t)}\frac{da(t)}{dt}\left[B(\theta) + \log(Ca^{1/4}/2) + \frac{1}{2}\log(2a(t))\right] - a(t) = -\Delta X(t) \tag{7.17a}$$

$$\frac{3}{4a(t)}\frac{da(t)}{dt}\left[B(\theta_c) + B(\theta_p) + 2\log(Ca^{1/4}/2) + \frac{1}{2}\log(a(t))\right] - a(t) = -\Delta X(t) \tag{7.17b}$$

where Eq. (7.17b) correspond to one drop in SFA and Eq. (7.17b) to two drops in AFM.

By setting $f(t) = \log(a(t))$ the numerical solution of Eq. (7.17) is straightforward to determine and the force, Eq. (7.3), can be expressed in terms of this dimensionless function $f(t)$, which is a function of the dimension time according to the scaling in Eq. (7.15)

$$F = -6\pi R\sigma Ca^{1/2}\frac{df}{dt} \tag{7.18}$$

The range of applicability of this approximation will be demonstrated in the results section.

7.3.2 Large force limit

We can derive a simple analytic expression for the force-displacement relationship valid for large forces (in the context of surface force measurements) when the dynamic interaction is repulsive between a solid particle and a drop. For a sessile drop subjected to an applied pressure distribution $(p+\Pi)$ localised axi-symmetrically about the apex, the drop height $z(r,t)$ obeys the modified Young-Laplace equation

$$\frac{\sigma}{r}\frac{\partial}{\partial r}\left[\frac{r(\partial z/\partial r)}{[1+(\partial z/\partial r)^2]^{1/2}}\right] = (p+\Pi) - \frac{2\sigma}{R} \tag{7.19}$$

On a radial scale that is small compared to the drop radius, the denominator may be replaced by unity and the resulting equation can be integrated to obtain the large r (on the scale of the radial extent of the film) limiting form of this inner solution

$$z^{inner}(r,t) \cong z(0,t) - \frac{r^2}{2R} - H + G\log(r) \tag{7.20}$$

where $z(0,t)$ is the perturbed drop height at $r=0$,

$$H(t) = \frac{1}{\sigma}\int_0^\infty (p(r,t)+\Pi(r,t))\, r\log(r)\ dr \tag{7.21}$$

and G is given by Eq. (7.3). The requirement for small r limit of the outer solution, Eq. (7.4), to match with the large r limit of the inner solution, Eq. (7.20), gives an expression for the deformation of the drop apex

$$z_0 - z(0,t) = -H - G\left[\log\left(\frac{1}{2R_d}\right) + B(\theta)\right] \tag{7.22}$$

We can integrate the equation for the film thickness, h given by Eq. (7.2a) to give $(R_f^{-1} \equiv R^{-1} + R_s^{-1})$

$$r\frac{\partial h}{\partial r} = \frac{r^2}{R_f} - \frac{1}{\sigma}\int_0^r (p+\Pi)r'\ dr' \tag{7.23}$$

When $(p+\Pi)$ is repulsive, a dynamic film of thickness h_f forms between the drop and the solid particle. Where the drop is flattened against the solid

particle, $\partial h/\partial r \sim 0$ on the scale of the drop radius and we can define the film radius, a to be the value of r at which $\partial h/\partial r$ starts to increase. From a consideration of the right hand side of Eq. (7.23) the film radius can be approximated by

$$a \approx \left[\frac{R_f}{\sigma}\int_0^\infty (p+\Pi) r\ dr\right]^{1/2} = \sqrt{GR_f} \tag{7.24}$$

so the dynamic pressure distribution within this film can be approximated by

$$(p+\Pi) \approx \begin{cases} (2\sigma/R_f), & 0 < r < a \\ 0, & r > a \end{cases} \tag{7.25}$$

Using this approximation in Eq. (7.22) gives an approximate expression for the drop deformation in terms of the force, F

$$z_0 - z(0,t) \cong -\frac{F}{4\pi\sigma}\left[\log\left(\frac{FR_0}{8\pi\sigma R_d^2}\right) + 2B(\theta) - 1\right] \tag{7.26}$$

where to leading order in (G/R_d) we have made the approximation $R_f^{-1} \equiv R^{-1} + R_s^{-1} \approx R_d^{-1} + R_s^{-1} \equiv R_0^{-1}$.

From the definition of the displacement function $\Delta X(t)$ in Eq. (7.9) we now have the desired results between the two measurable experimental quantities: the displacement, $\Delta X(t)$ and the force, F

$$\Delta X \cong h_f + \frac{F}{4\pi\sigma}\left[\log\left(\frac{FR_0}{8\pi\sigma R_d^2}\right) + 2B(\theta) - 1\right] \tag{7.27a}$$

The constant dynamic film thickness h_f has been added to the right hand side as an approximate attempt to account for the fact that the force will start to be significant when the surfaces are at h_f apart, where $\Delta X = h_f$, rather than at $\Delta X = 0$, when the surfaces would have come into contact without deformation.

The one drop SFA result corresponds to the limit of the particle raduis, $R_s \to \infty$, or $R_0 \to R_d$, the undeformed radius of the drop. With the appropriate expression for $B(\theta)$ from Eq. (7.5), the result in Eq. (7.27a) is valid for both the pinned or free to slip three phase contact line condition and for acute or obtuse contact angles, θ.

A similar derivation gives the corresponding result for the force-displacement relation for two drops in the AFM for which we have to account for the deflection of the cantilever with spring constant K

$$\Delta X \cong h_f + \frac{F}{2\pi\sigma}\left[\log\left(\frac{F}{8\pi\sigma\sqrt{R_c R_p}}\right) + B(\theta_c) + B(\theta_p) - 1 - \frac{2\pi\sigma}{K}\right] \quad (7.27b)$$

In practice the deflection of the cantilever is often taken into account before the data are analysed for force-displacement effects.

An important observation about Eq. (7.27) is the non-linear nature of the force-displacement relationship over the typical range force magnitudes. Also this force-displacement relationship depends on properties of the drop such as the undeformed drop radius, interfacial tension, contact angle, the particle radius as well as whether the three phase contact line sticks or slips through the function, $B(\theta)$. This has implications in any attempt to locate the constant compliance region of AFM results as earlier work on the interpretation of direct force measurements involving drops and bubbles assumed that they deform as Hookean springs [34].

7.4 Results

7.4.1 Approximate formulae – SFA geometry

We compare the extent to which the approximate results for small forces Eq. (7.18) and large forces Eq. (7.27) are able to model the force-displacement curves due to hydrodynamic interactions for the case of a single drop against a moving flat plate in the SFA configuration as given by the model described by Eqs. (7.1) – (7.9). Disjoining pressure effects have not been included in this comparison.

In Figure 7.1a, we compare the large force analytic formula given by Eq. (7.27a) with the numerical solution of Eqs. (7.1) – (7.9) for the approach of a mica plate at constant velocity ($V = 24$ μm/s) towards a mercury drop. The mica plate is driven to 17.5 μm beyond the point at which the mica would

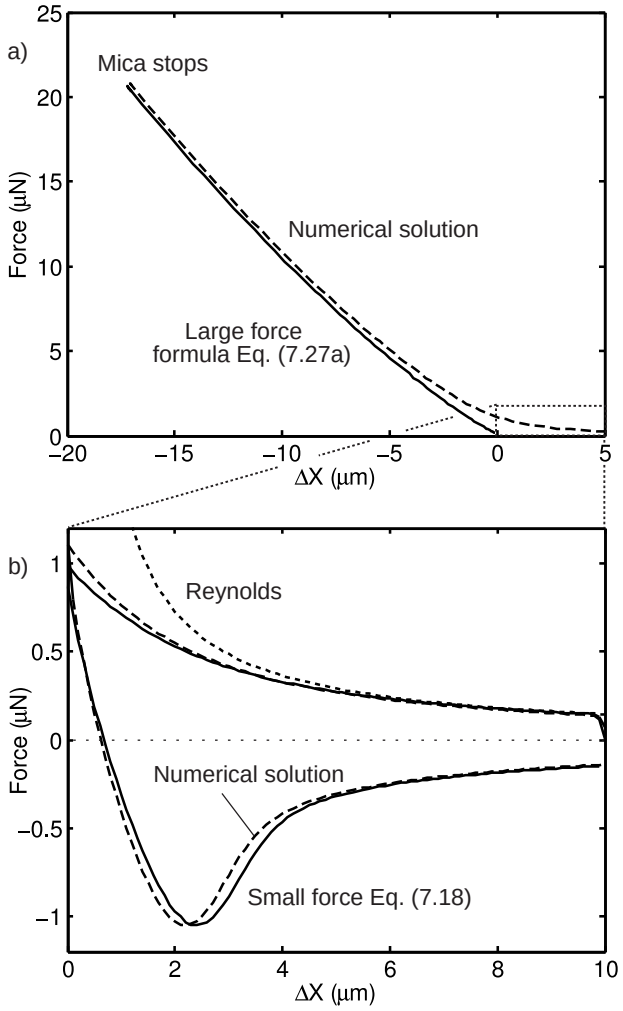

Figure 7.1: Comparison of approximate results (solid lines) for large (Eq. (7.27a)) and small forces (Eq. (7.18)) with full numerical solution (broken lines) for the force against mica displacement between a single mercury drop (surface tension 420 mN/m, undeformed radius of curvature 1.9 mm) interacting with a flat mica plate in the SFA geometry across water driven at a constant velocity of 24 μm/s. (a) The mica plate is driven to a position 17.5 μm beyond the position where the mica and the mercury would have made contact if the mercury did not deform (ie $\Delta X = -17.5$ μm). (b) The mica plate is driven to $\Delta X = 0$ and is then retracted at the same speed. There is no disjoining pressure term between the mica and the mercury interface. The constant velocity Reynolds result (dotted line) is also included for comparison.

have made contact with the mercury drop if the drop did not deform ($\Delta X =$ –17.5 μm). We see that the analytic formula tracks the full numerical results closely for $\Delta X \leqslant -5$ μm.

To assess the accuracy of the small force result given by Eqs. (7.17a) and (7.18), the mica plate is driven towards the mercury drop at 24 μm/s until $\Delta X = 0$ (where the surfaces would have touched if the mercury did not deform), and is then retracted at the same speed. In Figure (7.1b) we can see that all the key features of the force-displacement curve, including the force maximum at $\Delta X = 0$ and the depth and position of the attractive minimum in the retraction branch are reproduced quantitatively by the approximate formula. For comparison, the constant velocity Reynolds formula: $F = 6\pi\mu R^2 V/\Delta X = 6\pi\mu R^2 V/[X(0) - Vt]$, which diverges at $\Delta X = 0$ is also given.

7.4.2 Comparison with SFA experiments

An assessment of the model given in Eqs. (1) – (12) in predicting measured time evolution of the deformations of a mercury/electrolyte interface due to an approaching mica plate at constant velocity was given in Figures 5.2 and 5.6. We saw that the model performs equally well in the presence of a strongly repulsive (SR) disjoining pressure between the mica and the mercury that leads to an equilibrium flat film when the mica stops, or in the presence of a strongly attractive (SA) disjoining pressure that lead to an unstable film that ultimately collapses as the mercury jumps into contact with the mica plate.

From the film profiles, the total force between the mica and the deformable mercury drop can be calculated and separated into contributions from hydrodynamic and disjoining pressure contributions [39]. In Figures 7.2a and 7.2b we can see excellent agreement between the force components predicted from theory and deduced experimentally. This is not surprising since the profiles as seen in Figures 5.2 and 5.6 are in excellent agreement. It is interesting to note that until the mica stops, after which the mercury interface of the strongly attractive case collapses onto the mica, the force as

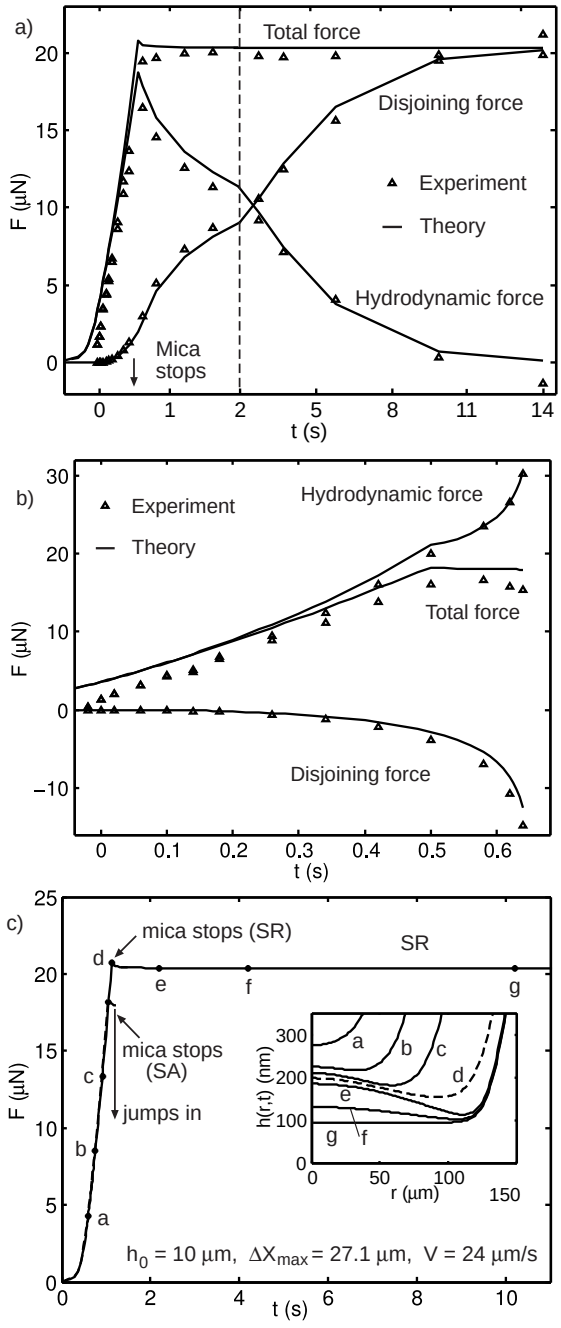

Figure 7.2: Comparisons between numerical solutions of Eqs. (7.1) – (7.9) (lines) and SFA experimental (symbols) determinations of components of the total force as a function of time for the strongly repulsive (SR) (b) strongly attractive (SA) disjoining pressures. (c) an illustration that the force between the SR and SA cases are nearly identical until the mica stops when the SA system jumps into contact while the SR case continues to evolve to the equilibrium film under a constant force condition – from point (d) when the mica stops to point (g).

a function of time is nearly identical between the strongly repulsive and the strongly attractive cases (Figure 7.2c). Indeed this portion of the force curve is also well described by the large force formula Eq. (7.27a).

The results in Figure 7.2c also demonstrate that after the mica stops, the interface in the strongly repulsive case evolves towards the equilibrium film under constant force as pointed out in section 2.1. To leading order, the value of the constant force is approximately equal to the Laplace pressure of the drop multiplied by the film radius which is approximately constant (curves (d) to (g) in the inset of Figure 7.2c) after the mica stops. As the deformation of the drop remains small compared to the drop dimension, the Laplace pressure remains essentially constant.

7.4.3 Comparison with AFM experiments

We now compare predictions of the force calculated from Eqs. (1) – (12) as well as from the approximate formula for small forces (Eqs. (20a) and (21)) and for deformations (Eq. (24b)) with an example of the dynamic force between two oil drops with adsorbed sodium dodecylsulphate (SDS) as measured on the AFM at a relatively low drive velocity of 2 μm/s [28]. Other relevant system and input parameters are: $R_c = 41$ μm, $R_p = 90$ μm, $\theta_c = 100°$, $\theta_c = 50°$, $h_{eq} = 26$ nm, $h_{start} = 1.81$ μm, $\Delta X_{max} = 2$ μm, $\sigma = 10$ mN/m, surface potential $\Psi_0 = -100$ mV, Debye length $\kappa^{-1} = 3.3$ nm, and $Ca = 1.8\text{x}10^{-7}$.

From Figure 7.3 we see that for $\Delta X \geqslant 0$, the small force approximation given by Eqs. (7.17b) and (7.18) is very close to the full numerical solution and to the experimental data. For $F \geqslant 1$ nN, Eq. (7.27b) derived using the assumption of large force becomes applicable. The full numerical solution of the governing equation is in excellent agreement with experimental results at all displacements. As the drive velocity increases, the full solution becomes more necessary in bridging the transition region between the low force limit and the moderate deformation regime. One should also bear in mind that the governing equations given by Eqs. (7.1) – (7.9) have been obtained under a small strain assumption, as defined by $(F/2\pi\sigma R) \ll 1$ (see also Discussions).

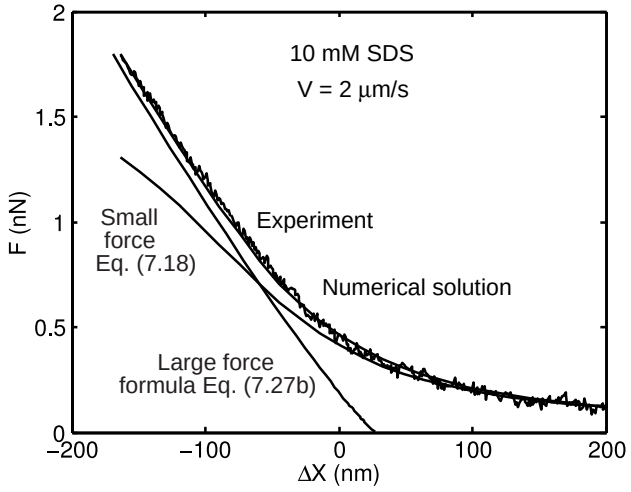

Figure 7.3: Comparisons between the numerical solution of Eqs. (7.1) – (7.9) which lies on top of experimental forces measured on the AFM between two drops on approach, the large force formula given by Eq. (7.27b) and the small forces result given by Eq. (7.17a) and (7.18). The drive velocity is 2 μm/s. The disjoining pressure due to electrical double layer interactions between the drops is repulsive [28].

Fortunately current AFM and SFA measurements fall within this regime.

7.5 Discussion

The AFM and SFA experiments probe the behaviour involving deforming interfaces on very different scales. For example the characteristic drop sizes are of order micrometer in the AFM and millimeter in the SFA experiments. The forces involved also differ by three orders of magnitude: nN for the AFM and μN for the SFA. Also the interfacial tensions: oil/water and mercury/water, differ by two orders of magnitude. However, the two types of experiments are similar when viewed on an appropriate scale.

In both cases, the deformation of the interface on the macroscopic scale is characterised by ΔX and there is a characteristic length associated with the interaction force, F and the interfacial tension σ: $G = F/2\pi\sigma$. Dimensional

analysis expects a functional relationship between the dimensionless ratio (G/R) and the strain $(\Delta X/R)$ that can also depend on the contact angle θ. In Figure 7.4, it is evident where the AFM and SFA reside in this scaled domain.

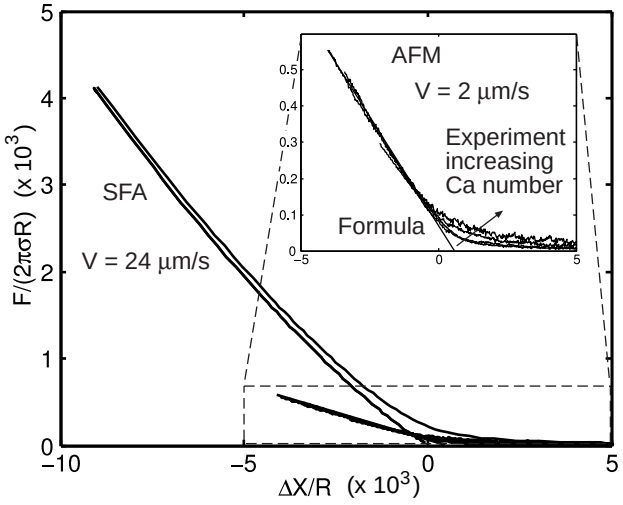

Figure 7.4: Comparisons between AFM and SFA forces on the same scale. The inset provides details due to variations in the capillary number, Ca.

The effects of varying the drive velocity, V in AFM force measurement and the associated variations with the capillary number $Ca = (\mu V/\sigma)$ are demonstrated in Figure 7.5. We observe that the moderate deformations formula (Eq. (25b)) is applicable at low velocities or $Ca \lesssim 10^{-7}$, while the full numerical solution is required to describe results at higher capillary numbers.

Finally we demonstrate the effects of contact angle in SFA (one drop) and AFM configurations (two drops, assuming identical contact angles) in Figure 7.6 in the limit of zero capillary number. With increasing contact angle, the drop(s) become more compliant resulting in a lower scaled force for the same scaled strain or deformation.

In this study we have demonstrated the utility of a model based on the Stokes-Reynolds theory of thin film drainage and the Young Laplace equation of drop deformation that can provide accurate descriptions of force measure-

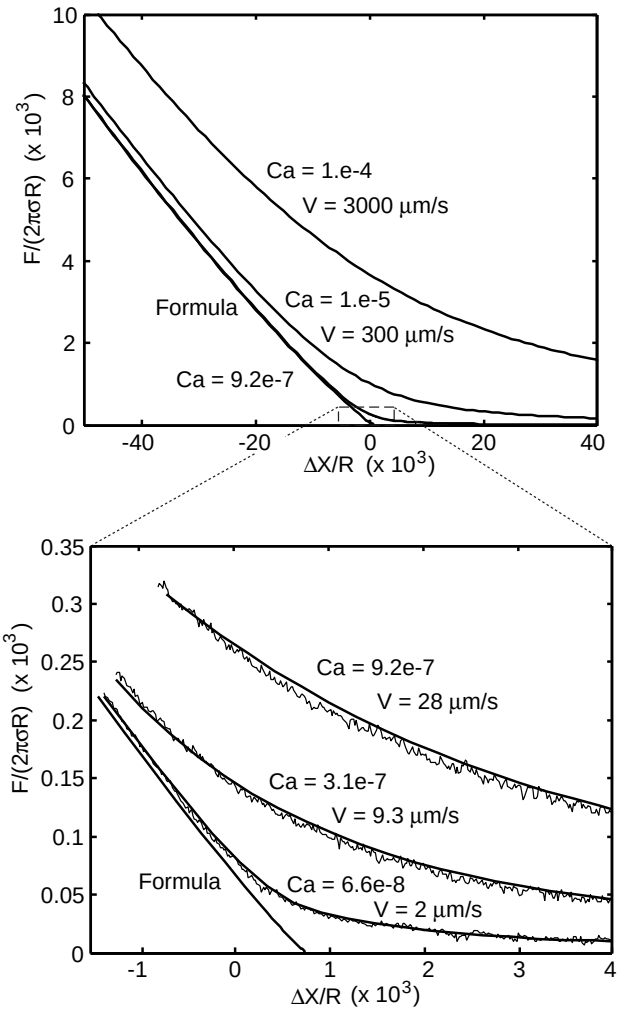

Figure 7.5: AFM results plotted on the dimensionless force-strain scale. (a) For such experiments, unrealistically large drive velocities still correspond to small capillary numbers, Ca. (b) Comparison with AFM experimental results at 1 mM SDS. The large force results (Eq. (7.27b)) is applicable to low velocities or $Ca \lesssim 10^{-7}$. The full numerical solution is required to describe results at higher capillary numbers.

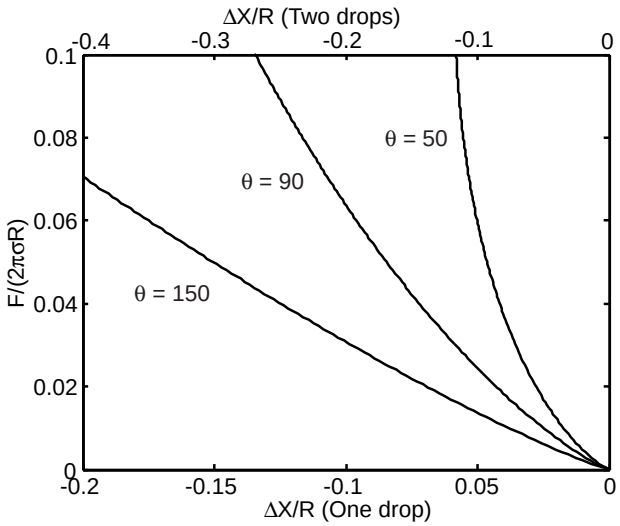

Figure 7.6: Variations of the scaled force with scaled deformation for the AFM (two drops, identical contact angles) and SFA (one drop) configurations at zero capillary number.

ment and deformation studies based on the AFM and the SFA. A key element of the model is that the constant volume constraint of interacting drops gives rise to a new boundary condition for the set of partial differential equations. Two simple analytic limits of this model have been derived. One is applicable at large separations and small forces for which contributions of the disjoining pressure can be neglected and the other is applicable at large force but at low capillary numbers or drive velocities where a stable dynamic film forms between the interacting interfaces. While the model is essentially a small strain model, it has been demonstrated that it covers the practical range of direct force measurement based on this family of apparatus. Fortunately, this regime also covers the domain of interactions of interest in typical droplet and emulsion interactions.

Chapter 8

Conclusions and future work

A considerable amount of experiments involving interacting drops and bubbles in small scales have been performed in the past decade using precise devices such as the Atomic Force Microscope and the Surface Force Apparatus. The goal of this thesis was to improve on the theoretical understanding of how interfaces behave during interaction since the models available in the literature were not able to properly describe the experiments we were analysing. The most important theoretical contribution of this thesis is the development of a new boundary condition at constant volume that properly represents the experiments. With close collaboration with experimentalists we were able to provide a better understanding of such interactions.

The developed model is applicable for most interactions involving deformable drops in the colloidal range in which relative low velocities, and small deformations give rise to a thin film between the interfaces that can be solved using Reynolds theory. The nonlinear system of partial differential equations can be solved numerically in less than one minute in a desktop computer using a standard Matlab package. And this fast running time allowed us to perform extensive parameter sensitivities and understand what are the important contributions to the problem. The numerical technique and solver utilised proved to be adequate and there were no problems regarding solving the theory during this project. The techniques available are accurate and fast enough to properly solve the systems of equations for interactions between deformable interfaces. What needs to be improved is the

understanding of the behaviour of real systems by developing better models for situations that present more complications or new experimental features.

Previous models in the literature considered either constant force or constant velocity interactions. The use of constant volume in this work is the correct way to represent the physical problem since some systems can present both characteristics as observed in some SFA experiments. Comparisons between our model and the constant velocity model from the literature show that the second is not appropriate for a general situation we analysed, but will only be applicable to solve for the whole drop with small contact angle. With impressive agreement between theory and experiment we were confident to use the model to make predictions on what would happen in a situation that cannot be reached experimentally. Also the model can provide more information than the experiment for a given situation, for example, the AFM experiment only provides the force *vs* displacement curve while the model provide separations, pressures, shear rates and other characteristics of the system. For the drop-sphere case, the model recovers the interface of the drop as a function of time since the sphere is not deforming.

For all the experimental data we analyzed we used the no-slip boundary condition at the liquid-liquid interface. In the AFM experiment the no-slip boundary condition is expected since surfactant was added to the system which is known to immobilize the interface. In some of the experiments even with low amounts of surfactant, much below the critical micelle concentration, the behaviour was the same and there was no need for introduction of effects such as surfactant transport or Marangoni. On the other hand, the mercury/electrolyte interface in the SFA experiment was expected to behave like a slip interface since it was attempted to have a clean system and the viscosity of the mercury is just about 1.5 times the viscosity of the electrolyte. A few reasons were proposed for such behaviour including contamination or electroviscous effects that can make the interface behave as immobile.

This work derived a nonlinear formula that relates force and displacement for moderate forces. As a consequence, deformable drops cannot be treated as Hookean springs as early literature have assumed. We also compared small forces at large separations and observed that drops in the studied regimes

behave mostly like solid spheres and differences are only noticeable when deformation becomes important.

Lastly we present some interesting problems for future work in this area that can be analyzed both theoretically and experimentally. Some of the ideas are:

1. From experimental and theoretical observations, the rim of the interfaces of the drops approach when trying to pull them apart (see Figure 6.4) and retract initially when trying to push them together (see Figure 6.1). This important process might have many applications in coalescence and stability of emulsions and a possible project is to quantify both theoretically and experimentally these effects.

2. We modelled and understood systems under well known driving conditions. An interesting problem to model is two drops or drop-particle interactions in a free system like in a real emulsion or suspension. In this case the driving mechanisms can be gravity, thermal motion and these features could be implemented using Newton's law.

3. Coalescence of drops is a problem that is not yet completely understood. In fact some of the ideas proposed in the literature like capillary waves were never seen in the attractive systems we modelled. Further research both experimental and theoretical is necessary to properly understand the coalescence process.

4. Study the effects of slip boundary condition and circulation inside the drops under constant volume to see its effects and differences compared to the no-slip boundary condition. Determine in which practical situations the physical interfaces would behave as slip boundary condition.

5. All experiments studied in this thesis used Newtonian materials, which makes the modelling easier. Since many applications involve non-Newtonian materials, it would be interesting to observe and quantify the different behaviours these systems would present; the models have to take into account such peculiarities.

6. The experimental systems we studied were all axisymmetric which facilitates solving the equations. The development of models for non symmetric systems can be an interesting theoretical project even though it presents complications.

Bibliography

[1] S. Abid and A. K. Chesters. The drainage and rupture of partially-mobile film between colliding drops at constant approach velocity. *International Journal of Multiphase Flow*, 20:613–629, 1994.

[2] D. E. Aston and J. C. Berg. Quantitative analysis of Fluid Interface-Atomic Force Microscopy. *Journal of Colloid and Interface Science*, 235:162–169, 2001.

[3] D. E. Aston and J. C. Berg. Thin-film hydrodynamics in Fluid Interface-Atomic Force Microscopy. *Industrial & Engineering Chemistry Research*, 41:389–396, 2002.

[4] P. Attard and S. J. Miklavcic. Effective spring constant of bubbles and droplets. *Langmuir*, 17:8217–8223, 2001.

[5] D. C. Bardos. Contact angle dependence of solid probe-liquid drop forces in AFM measurements. *Surface Science*, 515:157–176, 2002.

[6] S. Basu and M. M. Sharma. Measurement of critical disjoining pressure for dewetting of solid surfaces. *Journal of Colloid and Interface Science*, 181:443–455, 1996.

[7] G. K. Batchelor. *An Introduction to Fluid Dynamics*. Cambridge University Press, Cambridge, 2000.

[8] I. B. Bazhlekov, A. K. Chesters, and F. N. van de Vosse. The effect of dispersed to continuous-phase viscosity ratio on film drainage between interacting drops. *International Journal of Multiphase Flow*, 26:445–466, 2000.

[9] D. Bhatt, J. Newman, and C. J. Radke. Equilibrium force isotherms of a deformable bubble/drop interacting with a solid particle across a thin liquid film. *Langmuir*, 17:116–130, 2001.

[10] J. Blawzdziewicz, E. Wajnryb, and M. Loewenberg. Hydrodynamic interactions and collision efficiencies of spherical drops covered with an incompressible surfactant film. *Journal of Fluid Mechanics*, 395:29–59, 1999.

[11] E. Bonnacurso, H.-J. Butt, and V. S. J. Craig. Surface roughness and hydrodynamic boundary slip of a Newtonian fluid in a completely wetting system. *Physical Review Letters*, 90:144501–1–4, 2003.

[12] H.-J. Butt. A technique for measuring the force between a colloidal particle in water and a bubble. *Journal of Colloid and Interface Science*, 166:109–117, 1994.

[13] S. L. Carnie, D. Y. C. Chan, C. Lewis, R. Manica, and R. R. Dagastine. Measurement of dynamical forces between deformable drops using the Atomic Force Microscope. I. Theory. *Langmuir*, 21:2912–2922, 2005.

[14] S. L. Carnie, D. Y. C. Chan, and R. Manica. Modelling drop-drop interactions in an atomic force microscope. *ANZIAM Journal*, 46 (E):C805–C819, 2005.

[15] D. Y. C. Chan, R. R. Dagastine, and L. R. White. Force between a rigid probe particle and a liquid interface I. The repulsive case. *Journal of Colloid and Interface Science*, 236:141–154, 2001.

[16] D. Y. C. Chan and R. G. Horn. The drainage of thin liquid films between solid surfaces. *Journal of Chemical Physics*, 83:5311–5324, 1985.

[17] D. Y. C. Chan, R. M. Pashley, and L. R. White. A simple algorithm for the calculation of the electrostatic repulsion between identical charged surfaces in electrolyte. *Journal of Colloid and Interface Science*, 77:283–285, 1980.

[18] J.-D. Chen. Effect of London-van der Waals and electric double layer forces on the thinning of a dimpled film between a small drop or bubble and a horizontal solid plane. *Journal of Colloid and Interface Science*, 98:329–341, 1984.

[19] X. Chen, E. Rame, and S. Garoff. The effects of thin and ultrathin liquid films on dynamic wetting. *Physics of Fluids*, 16:287–297, 2004.

[20] A. K. Chesters. The modelling of coalescence processes in fluid-liquid dispersions: A review of current understanding. *Chemical Engineering Research and Design*, 69:259–270, 1991.

[21] A. K. Chesters and I. B. Bazhlekov. Effect of insoluble surfactants on drainage and rupture of a film between drops interacting under a constant force. *Journal of Colloid and Interface Science*, 230:229–243, 2000.

[22] A. K. Chesters and G. Hofman. Bubble coalescence in pure liquids. *Applied Scientific Research*, 38:353–361, 1982.

[23] L. Y. Clasohm, J. N. Connor, O. I. Vinogradova, and R. G. Horn. The wimple: Rippled deformation of a fluid drop caused by hydrodynamic and surface forces during thin film drainage. *Langmuir*, 21:8243–8249, 2005.

[24] J. N. Connor and R. G. Horn. Measurement of aqueous film thickness between charged mercury and mica surfaces: A direct experimental probe of the Poisson-Boltzmann distribution. *Langmuir*, 17:7194–7197, 2001.

[25] J. N. Connor and R. G. Horn. The influence of surface forces on thin film drainage between a fluid drop and a flat solid. *Faraday Discussions*, 123:193–206, 2003.

[26] V. S. J. Craig, C. Neto, and D. R. M. Williams. Shear-dependent boundary slip in an aqueous Newtonian liquid. *Physical Review Letters*, 87:054504–1–4, 2001.

[27] R. R. Dagastine, T. T. Chau, D. Y. C. Chan, G. W. Stevens, and F. Grieser. Interaction forces between oil-water particle interfaces – non-DLVO forces. *Faraday Discussions*, 129:111–124, 2005.

[28] R. R. Dagastine, R. Manica, S. L. Carnie, D. Y. C. Chan, G. W. Stevens, and F. Grieser. Dynamic forces between two deformable oil droplets in water. *Science*, 313:210–213, 2006.

[29] R. R. Dagastine, G. W. Stevens, D. Y. C. Chan, and F. Greiser. Forces between two oil drops in aqueous solution measured by AFM. *Journal of Colloid and Interface Science*, 273:339–342, 2004.

[30] R. R. Dagastine and L. R. White. Forces between a rigid probe particle and a liquid interface II. The general case. *Journal of Colloid and Interface Science*, 247:310–320, 2002.

[31] R. H. Davis, J. A. Schoenberg, and J. M. Rallison. On the buoyancy-driven motion of a drop towards a rigid surface or a deformable interface. *Physics of Fluids A*, 1:77–81, 1989.

[32] B. V. Derjaguin. Untersuchungen uber die reibung und adhasion. *Kolloid Z*, 69:155–164, 1934.

[33] D. S. Dimitrov and I. B. Ivanov. Hydrodynamics of thin liquid films. On the rate of thinning of microscopic films with deformable interfaces and validity of the Reynolds law. *Journal of Colloid and Interface Science*, 64:97–106, 1978.

[34] W. A. Ducker, Z. Xu, and J. N. Israelachvili. Measurements of hydrophobic and DLVO forces in bubble-surface interactions in aqueous solutions. *Langmuir*, 10:3279–3289, 1994.

[35] S. P. Frankel and K. J. Mysels. On the 'dimpling' during the approach of two surfaces. *Journal of Physical Chemistry*, 66:190–191, 1962.

[36] S. Hartland. The profile of the draining film beneath a liquid drop approaching a plane interface. *Chemical Engineering Progress Symposium Series*, 65:82–89, 1969.

[37] S. Hartland and J. D. Robinson. A model for an axisymmetric dimpled draining film. *Journal of Colloid and Interface Science*, 60:72–81, 1977.

[38] P. G. Hartley, F. Grieser, P. Mulvaney, and G. W. Stevens. Surface forces and deformation at the oil-water interface probed using AFM force measurement. *Langmuir*, 15:7282–7289, 1999.

[39] R. G. Horn, M. Asadullah, and J. N. Connor. Thin film drainage: Hydrodynamic and disjoining pressures determined from experimental measurements of the shape of a fluid drop approaching a solid wall. *Langmuir*, 22:2610–2619, 2006.

[40] R. G. Horn and J. N. Israelachvili. Direct measurement of structural forces betweentwo surfaces in a non-polar liquid. *Journal of Chemical Physics*, 75:1400–1411, 1981.

[41] R. J. Hunter. *Foundations of Colloid Science*. Vol. 1, Clarendon Press, Oxford, 1986.

[42] J. L. Hutter and J. Bechhoefer. Calibration of atomic force microscope tips. *Review of Scientific Instruments*, 64:1868–1878, 1993.

[43] J. N. Israelachvili. Measurements of the viscosity of liquids in very thin films. *Journal of Colloid and Interface Science*, 110:263–271, 1986.

[44] J. N. Israelachvili and G. E. Adams. Measurement of forces between two mica surfaces in aqueous electrolyte solution. *Journal of the Chemical Society Faraday Transactions*, 74:975–1001, 1978.

[45] P. Joseph and P. Tabeling. Direct measurement of apparent slip length. *Physical Review E*, 71:035303–1–4, 2005.

[46] J.-L. Joye, C. A. Miller, and G. J. Hirasaki. Dimple formation and behaviour during axisymmetrical foam film drainage. *Langmuir*, 8:3083–3092, 1992.

[47] E. Klaseboer, J. P. Chevaillier, C. Gourdon, and O. Masbernat. Film drainage between colliding drops at constant approach velocity: experiments and modeling. *Journal of Colloid and Interface Science*, 229:274–285, 2000.

[48] E. Klaseboer, J. P. Chevaillier, A. Mate, O. Masbernat, and C. Gourdon. Model and experiment of a drop impinging on an immersed wall. *Physics of Fluids*, 13:45–57, 2001.

[49] L. G. Leal. *Laminar flow and convective transport processes*. Butterworth Heinemann, Boston, 1992.

[50] C.-Y. Lin and J. C. Slattery. Thinning of a liquid film as a small drop or bubble approaches a fluid-fluid interface. *AIChеJ*, 28:786–792, 1982.

[51] C.-Y. Lin and J. C. Slattery. Thinning of a liquid film as a small drop or bubble approaches a solid plane. *AIChеJ*, 28:147–156, 1982.

[52] R. Manica, J. N. Connor, S. L. Carnie, R. G. Horn, and D. Y. C. Chan. Dynamics of interactions involving deformable drops: Hydrodynamic dimpling under attractive and repulsive electrical double layer interactions. *Langmuir*, 23:626–637, 2007.

[53] R. Manica, J. N. Connor, R. R. Dagastine, S. L. Carnie, R. G. Horn, and D. Y. C. Chan. Equilibrium and dynamic forces involving deformable interfaces on a nanometer length scale. *Submitted to Physics of Fluids*, 2007.

[54] D. McCormack, S. L. Carnie, and D. Y. C. Chan. Calculations of electric double-layer force and interaction free energy between dissimilar surfaces. *Journal of Colloid and Interface Science*, 169:177–196, 1995.

[55] P. Mulvaney, J. M. Perera, S. Biggs, F. Grieser, and G. W. Stevens. The direct measurement of the forces of interaction between a colloid particle and an oil droplet. *Journal of Colloid and Interface Science*, 183:614–616, 1996.

[56] S. A. Nespolo, D. Y. C. Chan, F. Grieser, P. G. Hartley, and G. W. Stevens. Forces between a rigid probe particle and a liquid interface: Comparison between experiment and theory. *Langmuir*, 19:2124–2133, 2003.

[57] C. Neto, D. R. Evans, E. Bonaccurso, H.-J. Butt, and V. S. J. Craig. Boundary slip in Newtonian liquids: a review of experimental studies. *Reports on Progress in Physics*, 68:2859–2897, 2005.

[58] H. Ohshima. Primary electroviscous effect in a dilute suspension of charged mercury drops. *Langmuir*, 22:2863–2869, 2002.

[59] R. M. Pashley. DLVO and hydration forces between mica surfaces in Li+, Na+, K+ and Cs+ electrolyte solutions: A correlation of double-layer and hydration forces with surface cation exchange properties. *Journal of Colloid and Interface Science*, 83:531–546, 1981.

[60] R. Pit, H. Hervet, and L. Leger. Direct experimental evidence of slip in hexadecane: Solid interfaces. *Physical Review Letters*, 85:980–983, 2000.

[61] M. Preuss and H.-J. Butt. Direct measurement of particle-bubble interactions in aqueous electrolyte: dependence os surfactant. *Langmuir*, 14:3164–3174, 1998.

[62] O. Reynolds. On the theory of lubrication and its application. *Philosophical Transactions of The Royal Society London*, A177:157, 1886.

[63] M. A. Rother, A. Z. Zinchenko, and R. H. Davis. Buoyancy-driven coalescence of slightly deformable drops. *Journal of Fluid Mechanics*, 346:117–148, 1997.

[64] A. Saboni, C. Gourdon, and A. K. Chesters. Drainage and rupture of partially mobile films during coalescence in liquid-liquid systems under a constant interaction force. *Journal of Colloid and Interface Science*, 175:27–35, 1995.

[65] B. A. Snyder, D. E. Aston, and J. C. Berg. Particle-drop interaction examined with an Atomic Force Microscope. *Langmuir*, 13:590–593, 1997.

[66] H. Spikes and S. Granick. Equation for slip of simple liquids at smooth solid surfaces. *Lamgmuir*, 19:5065–5071, 2003.

[67] T. T. Traykov and I. B. Ivanov. Hydrodynamics of thin liquid films. Effect of surfactants on the velocity of thinning of emulsion films. *International Journal Multiphase Flow*, 3:471–483, 1977.

[68] R. Tsekov and O. I. Vinogradova. A qualitative theory of wimples in wetting films. *Langmuir*, 21:12090–12092, 2005.

[69] E. J. W. Verwey and J. T. G. Overbeek. *Theory of the Stability of Lyophobic Colloids*. Elsevier, Amsterdam, 1948.

[70] O. I. Vinogradova. Drainage of a thin liquid film confined between hydrophobic surfaces. *Langmuir*, 11:2213–2220, 1995.

[71] O. I. Vinogradova and F. Feuillebois. Elastohydrodynamic collision of two spheres allowing slip on their surfaces. *Journal of Colloid and Interface Science*, 221:1–12, 2000.

[72] G. Webber, R. Manica, S. Edwards, G. Stevens, S. Carnie, R. Dagastine, F. Grieser, and D. Chan. Hydrodynamic interactions between a silica particle and a deformable droplet I: Effects of particle/droplet size ratio. *In preparation*, 2007.

[73] S.-M. Yang, L. G. Leal, and Y.-S. Kim. Hydrodynamic interaction between spheres coated with deformable thin liquid films. *Journal of Colloid and Interface Science*, 250:457–465, 2002.

[74] L. Y. Yeo, O. K. Matar, E. S. P. de Ortiz, and G. F. Hewitt. The dynamics of Marangoni-driven local film drainage between two drops. *Journal of Colloid and Interface Science*, 241:233–247, 2001.

[75] L. Y. Yeo, O. K. Matar, E. S. P. de Ortiz, and G. F. Hewitt. Film drainage between two surfactant-coated drops colliding at constant approach velocity. *Journal of Colloid and Interface Science*, 257:93–107, 2003.

[76] S. G. Yiantsios and R. H. Davis. On the buoyancy-driven motion of a drop towards a rigid surface or a deformable interface. *Journal of Fluid Mechanics*, 217:547–573, 1990.

[77] S. G. Yiantsios and R. H. Davis. Close approach and deformation of two viscous drops due to gravity and van der Waals forces. *Journal of Colloid and Interface Science*, 144:412–433, 1991.

[78] Y. Yoon, M. Borrell, C. C. Park, and L. G. Leal. Viscosity ratio effects on the coalescence of two equal-sized drops in a two-dimensional linear flow. *Journal of Fluid Mechanics*, 225:355–379, 2005.

[79] Y. Zhu and S. Granick. Apparent slip of Newtonian fluids past adsorbed polymer layers. *Macromolecules*, 35:4658–4663, 2002.

[80] Y. Zhu and S. Granick. Limits of the hydrodynamic no-slip boundary condition. *Physical Review Letters*, 88:106102–1–4, 2002.